COMPUTER SIMULATION OF GRAIN BOUNDARY GROOVING AND CATHODE VOIDING IN BAMBOO INTERCONNECTS BY SURFACE DIFFUSION UNDER CAPILLARY AND ELECTROMIGRATION FORCES

ÖNCÜ AKYILDIZ

SEPTEMBER 2004

COMPUTER SIMULATION OF GRAIN BOUNDARY GROOVING AND CATHODE VOIDING N BAMBOO INTERCONNECTS BY SURFACE DIFFUSION UNDER CAPILLARY AND ELECTROMIGRATION FORCES

A THESIS SUBMITTED TO
THE GRADUATE SCHOOL OF NATURAL AND APPLIED SCIENCES
OF
MIDDLE EAST TECHNICAL UNIVERSITY

BY

ÖNCÜ AKYILDIZ

IN PARTIAL FULFILLMENT OF THE REQUIREMENTS
FOR
THE DEGREE OF MASTER OF SCIENCE
IN
METALLURGICAL AND MATERIALS ENGINEERING

SEPTEMBER 2004

Approval of the Graduate School of Natural and Applied Sciences

Prof. Dr. Canan ÖZGEN
Director

I certify that this thesis satisfies all the requirements as a thesis for the degree of Master of Science.

Prof. Dr. Bilgehan ÖGEL
Head of Department

This is to certify that we have read this thesis and that in our opinion it is fully adequate, in scope and quality, as a thesis for the degree of Master of Science.

Prof. Dr. Tarık Ö. OĞURTANI
Supervisor

Examining Committee Members

Prof. Dr. Erman TEKKAYA	(METU, ME)
Prof. Dr. Tarık Ö. OĞURTANI	(METU, METE)
Prof. Dr. Bilgehan ÖGEL	(METU, METE)
Prof. Dr. Abdullah ÖZTÜRK	(METU, METE)
Prof. Dr. Yavuz TOPKAYA	(METU, METE)

I hereby declare that all information in this document has been obtained and presented in accordance with academic rules and ethical conduct. I also declare that, as required by these rules and conduct, I have fully cited and referenced all material and results that are not original to this work.

Name, Last name : Öncü AKYILDIZ

Signature :

ABSTRACT

COMPUTER SIMULATION OF GRAIN BOUNDARY GROOVING AND CATHODE VOIDING IN BAMBOO INTERCONNECTS BY SURFACE DIFFUSION UNDER CAPILLARY AND ELECTROMIGRATION FORCES

AKYILDIZ, Öncü
M.S., Department of Metallurgical and Materials Engineering
Supervisor: Prof. Dr. Tarık Ö. OĞURTANI

September 2004, 128 pages

The processes of grain boundary grooving and cathode voiding which are important in determining the life times of thin films connecting the transistors in an integrated circuit are investigated by introducing a new mathematical model, which flows from the fundamental postulates of irreversible thermodynamics, accounting for the effects of applied electric field and thermal stresses. The extensive computer studies on the triple junction displacement dynamics shows that it obeys the first order reaction kinetics at the transient stage, which is followed by the familiar time law as $t^{1/4}$, in the normalized time and space domain, at the steady state regime in the absence of the electric field (EF). The application of EF doesn't modify this time law very; but puts only an abrupt upper limit for the groove depth and fixes the total elapse time for that event, which is found to be inversely proportional with the electron wind intensity parameter. The drift in the cathode edge due to the surface diffusion along the side walls is simulated under the constant current regime. An analytical formula is obtained in terms of system parameters, which shows well defined threshold level for the onset of electromigration induced cathode drift, showing an excellent agreement with the reported experimental values in the literature.

Key words : Electromigration, thermal grooving, cathode failure, surface diffusion.

ÖZ

MİKRO ELETRONİK DEVRELERDEKİ BAMBU BENZERİ ARABAĞLANTI ELEMANLARINDA GERÇEKLEŞEN KAPİLERİ VE ELEKTROGÖÇ KUVVETLERİNİN ETKİSİNDE TANE SINIRI OLUKLANMASI VE KATOT BÖLGESİNDE BOŞLUK OLUŞUMU OLAYLARININ BİLGİSAYAR MODELLEMESİ

AKYILDIZ, Öncü
Y. Lisans, Metalurji ve Malzeme Mühendisliği Bölümü
Tez Yöneticisi: Prof. Dr. Tarık Ö. OĞURTANI

Eylül 2004, 128 sayfa

Bu çalışma ile mikro elektronik devrelerde transistörleri birbirlerine bağlayan iletkenlerin yaşam sürelerini belirlemekte büyük öneme sahip olan tane sınırı oluklanması ve katot bölgesi boşluk oluşumu olayları, dönüşümsüz termodinamiğin temel postülatlarını baz alan yeni bir matematik modelleme yöntemi ile incelenip, çok zengin bilgisayar simülasyon sonuçları elde edilmiştir. Simülasyon sonuçları elektrik alanın yokluğunda, üçlü kavşak hareketinin geçiş süresi boyunca birinci derece reaksiyon kinetiğine uyup, kararlı halde ise alışıla geldik zaman kanununa ($t^{1/4}$) uyduğunu göstermiştir. Elektrik alanın devreye girmesi ile zaman kanununun çok fazla değiştirmeyip, oluk derinliği için bir üst sınırın ortaya çıktığı ve bunun gerçekleşmesi için geçen zamanın elektron rüzgar kuvveti ile ters orantılı olduğu gözlemlenmiştir. Yan duvarlarda meydana gelen yüzey difüzyonunun yol açtığı katot ucundaki sürüklenme, sabit akım altında simüle edilip bu olayı betimleyen analitik bir formül ortaya koyulmuştur. Bu formül ile birlikte, katot sürüklenmesi için literatürde yer alan deneysel çalışmalar ile mükemmel bir şekilde uyum gösteren, ortam parametrelerine bağımlı bir eşik değeri bulunmuştur.

Anahtar Sözcükler : Elektrogöç, termal oluklanma, katot bozulması, yüzey difüzyonu.

To My Mother...

ACKNOWLEDGEMENTS

I am grateful to Prof. Dr. Tarık Ö. Oğurtanı for his valuable guidance and endless motivation during the study of this thesis.

I would like to thank Dr. Ersin E. Ören for sharing his knowledge about the subject and for encouraging me to start such a complicated study.

Finally I would like to express my gratitude to my mother Gönül Akyıldız, for her complimentary love and unshakable faith in me during my life.

TABLE OF CONTENTS

CHAPTER

LIST OF FIGURES

CHAPTER 1

INTRODUCTION

Thermal grooving at grain boundaries is a process of capillary-driven evolution of surface topography in the region where a grain boundary emerges to intersect a free surface of a polycrystal.

Thermal grooving, or speaking more generally, grain-boundary grooving affects many properties of polycrystalline materials especially in the presence of applied or internal fields. Common examples are growth of grain boundary grooves and cavities, stress relaxation and diffusional creep, stress voiding, electromigration behavior, liquid metal penetration along grain boundaries, and stress induced groove modification.

Mullins (1957) made the very first analytical study that was related to the grooving of a grain boundary without having the grain boundary diffusion by considering the triple junction to have the equilibrium capillarity configuration satisfying the Young (1805) relationship. With this study problem has been put into a theoretical basis and since then an extensive research effort has been put forth by scientists.

Some applications of the theory foreseen at the time it appeared first were the calculation of the surface diffusion coefficient (D_s) and absolute free energies (γ). Also it was foreseen that the theory could explain some features of the grain boundary motion. And finally Mullins (1957) stated that there was a possibility that thermal grooves were responsible for the inhibition of grain growth in a sample which has a large proportion of grain boundaries terminating on a surface, e.g. a thin sheet.

Experiments carried out up to day verified that the theory is successful in estimating surface diffusion coefficients and surface free energies. In any experiment, the groove width and depth are measured as functions of time and the diffusion coefficient is obtained from comparison with theory. Some examples are the studies on Cu (Mullins and Shewmon, 1959), Ag (Sharma and Spitz, 1981), Mo, Mo-Re, and Cr (Srinivasan, 1981).

However, the real success of the model is its ability to describe the surface profile at a given time and its evolution under certain circumstances. Actually not only the grain boundary grooving process but many fields of physics, chemistry, and metallurgy encounter the need for an understanding of surface structures of crystals which are subjected to various applied or internal fields. Examples of such areas of interest include thermionic emission, sintering, many problems in adsorption and catalysis.

Especially today's microelectronics industry demands a good understanding of morphological changes occurring in circuit elements called 'interconnects'.

In integrated circuits, electricity is conducted via thin film structures that are in direct contact with an effective heat sink (e.g., a silicon wafer). Through more than 30 years of experience, today thin films of Al - Cu alloys (interconnects) with a ranging width of about 50 μm to less than 1 μm are manufactured commercially for microelectronics industry. A near bamboo structure is produced as the width of these interconnects is reduced to microscopic dimensions. This near bamboo structure contains both interconnected networks of grain boundaries as well as grains, which span along the width of the line. Thus large proportions of grain boundaries in these thin films terminating at a free surface, and several grain boundary grooves are form.

Moreover these thermal grooves are subjected to large current densities ($\sim 10^6$ A/cm^2 (Ohring, 1971)) which presents a problematic mechanism called Electromigration.

Electromigration is the mass transport of a metal due to momentum transfer between the conducting electrons and the diffusing metal atoms when an electrical current passes through a metal thin film.

Electromigration induced failure of metallic interconnects is a complicated process, which involves flux divergence, vacancy and/or atom accumulation with or without compositional variations, void and hillock nucleation, growth and shape changes (Artz and Nix, 1991; Nix and Artz, 1992).

Grain-boundary grooves, is nothing however but surface voids nucleated at the sites of grain boundary intersections with free surfaces, so that the examination of the combined action of thermal grooving and electromigration inevitably becomes a major interest for microelectronics industry.

Computer simulation studies to consider multiple mechanisms involved in morphological changes take place in interconnect lines by the combined action of thermal grain boundary grooving and electromigration induced surface and grain boundary diffusion to observe the macroscopic effects of the microscopic variables lead successful developments to overcome the reliability problems.

The aim of this study is to examine the grooving dynamics under the effect of capillary and electromigration forces, evaluate the circumstances under which cathode failure takes place, and provide some suggestions on how to increase the mean time to failure. To this end a new mathematical model, which flows from the fundamental postulates of irreversible thermodynamics, was developed and computer simulation experiments were utilized.

In Chapter 2, a detailed literature review for grain-boundary grooving and cathode voiding phenomenons with and without electromigration are given.

In Chapter 3, a summary of rigorous irreversible thermodynamic treatment of morphological evaluation of curved surface layers, and their intersections with the grain boundaries, at the presence of electromigration-induced forces is presented.

In Chapter 4, the mathematical model and the numerical methods and procedures used in the solution of the completely normalized and scaled partial differential equation obtained in Chapter 3, are described briefly.

Results of the simulation experiments with their brief discussions are given in Chapter 5.

The computer code developed in C++ programming language to carry out the experiments is also given in Appendix.

CHAPTER 2

LITERATURE SURVEY

2.1. Overview

Groove formation on the tip of the triple junction formed by grain boundary (GB) and the two surfaces can occur via several mass transport mechanisms, such as surface diffusion, bulk diffusion, and evaporation and condensation, to reduce the combined free energy of the surface and the GB. Among these, surface diffusion dominates for temperatures far below the melting temperature and for grooves less than 10 μm in size (Xin and Wong, 2003). The familiar condition for the vanishing of the two surface tensions and the one GB tension along the line of intersection may be expressed as (Bailey and Watkins, 1950),

$$2\gamma_s \sin(\theta) = \gamma_b \tag{2.1.1}$$

where γ_s and γ_b are, respectively, the surface and boundary free energies per unit area, and θ is the equilibrium angle. This can be visualized by Fig. 2.1.1.

The rapid establishment of the equilibrium angle by atomic migration in the infinitesimal region of intersection produces sharp ridges that border each side of the boundary. These ridges tend to flatten by preferential mass transport mechanism. This flattening perpetually upsets the equilibrium angle and forces the groove to deepen (Mullins, 1957).

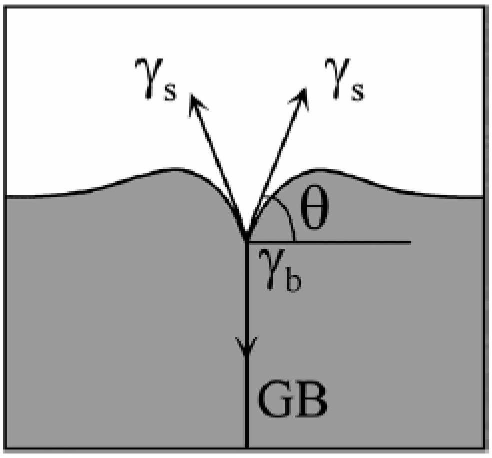

Figure 2.1.1: Classical Mullins-type GB groove, where γ_b and γ_s are GB and surface energies and θ is the dihedral angle (L. Klinger and E. Rabkin, 2001).

In the case of thermal grooving the effective mass transport mechanism is the surface diffusion, referring to the movement of atoms/molecules over the solid surface. This movement at the surface ends up with diversity in chemical potential of atoms then drive fluxes whose divergence leads to shape changes of the body. These changes are called capillary induced shape changes of a body.

When an electrical current passes, it is generally agreed that the force acting on diffusing atoms (i.e., ion cores) whether in bulk or thin films originates from the sum of two contributions, the direct electrostatic field force tending to drive ions toward the cathode, and the “friction” force caused by the momentum exchange between ions and scattered electrons, for electron conductors (electromigration), which tends to cause ionic motion in the opposite direction. The latter effect generally dominates so that atomic drift is toward the anode (Ohring, 1971). Thus the combined action of electromigation and capillary forces form a net driving force, and determine the characteristics of profile changes of a groove, which forms a basis to overcome reliability problems in interconnect lines.

2.2. Triple Junction Problem

Importance of capillarity-driven shape and micro structural evolution in solids can be connected with the fundamental role of surfaces and heterophase boundaries in physical and chemical processes, in stability and of structure and properties of materials.

The most obvious problem in this field is that of what shape a small crystal must take if its surface free energy is to be minimum for a given volume. In other words, when can the free energy of a plane surface be lowered by rearranging the atoms into hills and valleys?

The very fist study in this field came from Herring (1951), Neumann (1952) and Mullins (1957) which strictly relies on the equilibrium thermodynamics and the Gibbs description of interfaces and surfaces (Gibbs, 1948; Defay *et al.*, 1966). Later the problem studied by considering two coupled processes, namely the surface diffusion taking place on the interface separating the bulk phase from the void phase, and the GB diffusion driven by the gradient of the normal stress acting on the boundary. Triple junction, a geometric singularity, appears to be the place where these two processes are coupled.

The boundary conditions at the triple junction are assumed to be the continuity of the chemical potential, the conservation of mass, and the equilibrium capillarity configuration for geometry. These boundary conditions relying on the validity of Herring's relationship between chemical potential and the curvature are mutually incompatible for the triple junction.

At the triple junction there is no way of defining single curvature because of the large discontinuity due to the finite dihedral angle. Therefore Herring's relationship, which is valid for only smoothly varying surfaces, cannot be used at the triple junction. Continuity of the chemical potential implicitly assumes that there is no local equilibrium, which violates the possibility of internal entropy production. However the triple junction motion is completely natural (irreversible) process.

The driving force not only depends on the curvature gradient but also depends on the gradient of the Gibbs free energy difference between bulk and surface layers. In reality this additional term becomes responsible for the growth of the void surface layer during the shape evolution.

Takahashi *et al.* (1991) made similar studies on the void shrinkage process utilizing two different numerical but rather ad hoc models. One of them always restricts dihedral angle θ to the value of the equilibrium balance. In the other model, the local equilibrium at the triple junction is ignored (free dihedral angle). The second model resulted in a bonding pressure exponent that is in agreement with the experimental observations, namely; the dihedral angle is not always constant and changes as increasing net stress is applied to the bond-interface.

Triple junction steady state kinetics is also investigated recently by Gottstein and Shvindlerman (2002) in their studies related to the grain growth in 2D polycrystals by utilizing a modified version of the Von Neumann-Mullins relationship (Mullins, 2001) as a basis for the theoretical work. As a driving force for the triple junction mobility they assume an ad hoc connection, which may be valid only for the symmetrically disposed dihedral angles having an equilibrium value exactly equal to 60°. Very similar problem, namely the grain boundary crack growth in interconnects with electric field is considered by Liu *et al.* (2001). They also proposed that one has steady state shape evolution having an equilibrium angle at the crack apex by further arguing that the crack apex does not constitute a point source of entropy production, which is actually the key point in our theory of irreversible processes associated with the evolution dynamics of closed curved interfaces having triple junction singularities.

Recently, non-boundary tracking methods have been increasingly applied to simulate complex microstructural evolutions, including the Monte Carlo methods, the cellular automata, and the phase field method (Mahadevan and Bradley, 1999). In the phase field approach the field variables governed by semi-phenomenological equations of motion, e.g. the Cahn-Hilliard (Chan and Hilliard, 1958) non-linear diffusion equation for the density field and the time-dependent Ginzburg-Landau (Landau and Lifshitz, 1980) equation for the long-range order parameter field. Kazaryan *et al.* (1999) generalized phase field approach by incorporating the rigid–body rotation for the computer simulation of sintering by further assuming that the triple junction velocity can be determined from the steady state requirement at the grain boundary. Triple junction motion is also investigated by Cahn *et al.* (1996) for an Allen-Cahn / Cahn-Hilliard (Novick-Cohen, 2000) system utilizing long time asymptotic, which is still incorporated by the requirement of the uniform displacement. They also assumed that one has local physico-chemical equilibrium and continuity of chemical potentials at the triple junction. However, the more serious restriction associated with the method of phase field is the utilization of symmetric free energy form “double well potential” which results not only equal interfacial energies but also hinders the particle growth process as admitted by the authors themselves. Nathan *et al.* (2000) and Khenner *et al.* (2001) applied the level set approach to study grain boundary grooving and cathode edge displacement, while assuming a fixed surface slope and zero atomic flux at the groove root. The most recent computer simulation experiments in bare bamboo-type of lines under diffusion and electromigration (EM) fields are performed by Averbuch *et al.* (2003). These authors utilized highly sophisticated numerical procedures in their studies, but still they assumed that there is an equilibrium configuration at the triple junction, and the triple junction displacement velocity can be extrapolated from the projection of the normal velocities of the neighboring nodes in the direction of the intergranular grain boundary.

Ogurtani (2000) developed a model for the void configurational evolution during the intergranular motion, considering the generalized forces, the conjugate fluxes, and the energy dissipation at a triple junction in multi-component systems. Ogurtani also states that the first two of the normally used three boundary conditions at the triple point – the continuity of the chemical potential, the equilibrium capillarity configuration for geometry, and the conservation of mass – are mutually incompatible. Considering the internal entropy production associated with the virtual displacements of the junction, and applying the laws of linear thermodynamics only, they deduced (longitudinal and transverse) the displacement velocities of the triple junction.

2.3. Mullins' Theory of Thermal Grooving

Mullins derived a general partial differential equation for the rate of change of the profile of a surface for profile changes occurring by surface diffusion mechanism. In the derivation and solution of the differential equations describing the development of a groove profile, the following assumptions were made,

1) The system is closed and contains a metal poly-crystal in quasi-equilibrium with its vapor.
2) The properties of an interface are independent of its orientation with respect to the adjacent crystals.
3) All matter transport occurs by surface diffusion.
4) Macroscopic concepts such as surface free energy and surface curvature are valid.
5) There is negligibly flow of matter out of the boundary proper; instead, the role of the boundary is to maintain the correct equilibrium angle in the infinitesimal region of intersection.
6) The absolute value of the profile slope is everywhere small compared to unity,

$$1 << \frac{\gamma_b}{2\gamma_s} = \sin\theta \approx \tan\theta = \frac{dy(0,t)}{dx}$$

The surface profile is described a function $y(x,t)$ where y is the departure from of the actual profile from the initial flat surface, x is the distance from the GB, and t is the elapsed time since the groove started to grove. The arc length measured along the curve from the boundary intersection is denoted by s, and the curvature by $K(s)$.

The increase in the chemical potential per atom that is transferred from a point of zero curvature to a to a point of curvature K on the surface is given by,

$$\mu(K) = K\gamma\Omega \tag{2.3.1}$$

where γ is the surface free energy per unit area, and Ω is the molecular volume. Gradients of chemical potential along the surface will therefore be associated by gradients of curvature. Such gradients will produce a drift of surface atoms with an average velocity given by the Nernst-Einstein relation,

$$V = -\frac{D_s}{kT}\frac{\partial\mu}{\partial s} = -\frac{D_s\gamma\Omega}{kT}\frac{\partial K}{\partial s} \tag{2.3.2}$$

where D_s is the coefficient of surface diffusion, k is the Boltzmann's constant, and T is the absolute temperature. The surface current J is the product of average velocity of surface atoms, V, by the number of atoms per unit area, ν,

$$J = -\frac{D_s\gamma\Omega\nu}{kT}\frac{\partial K}{\partial s} \tag{2.3.3}$$

If the surface divergence of negative value of surface current, $-J$, is taken, one obtains the increase in the number of atoms per unit area per unit time. This may be converted to the speed of movement r_n of the surface element along its normal by multiplying by Ω. Then,

$$r_n = \frac{D_s\gamma\Omega^2\nu}{kT}\frac{\partial^2 K}{\partial s^2} \tag{2.3.4}$$

In expressing above equation in terms of $y(x,t)$, the following relationships were used,

$$\frac{\partial}{\partial s}=\left(\frac{\partial x}{\partial s}\right)\left(\frac{\partial}{\partial x}\right) \tag{2.3.5}$$

$$r_n=\left(1+y'^2\right)^{-1/2}\left(\frac{\partial y}{\partial t}\right) \tag{2.3.6}$$

$$K=\frac{-y'}{\left(1+y'^2\right)^{3/2}} \tag{2.3.7}$$

$$\frac{\partial x}{\partial s}=\left(1+y'^2\right)^{-1/2} \tag{2.3.8}$$

Substituting these to Eq. (2.3.4) yields the general partial differential equation for the rate of change of the surface profile,

$$\frac{\partial y}{\partial t}=-B\frac{\partial}{\partial x}\left(\left(1+y'^2\right)^{-1/2}\frac{\partial}{\partial x}\left(\frac{-y''}{\left(1+y'^2\right)^{3/2}}\right)\right) \tag{2.3.9}$$

where,

$$B=\frac{D_s\gamma\Omega^2\nu}{kT} \tag{2.3.10}$$

This equation solved for the function $y(x,t)$ subjecting to the following boundary conditions,

$$y\left(x,0\right)=0 \tag{2.3.11}$$

$$\frac{dy\left(0,t\right)}{dx}=\tan\left(\beta\right)=m \tag{2.3.12}$$

$$\frac{d^3y(0,t)}{dx^3} = \frac{3m\frac{d^2y(0,t)}{dx^2}}{\left(1+m^2\right)} = 0 \tag{2.3.13}$$

The last condition is the small slope approximation (assumption 6) of the main equation when we require a vanishing current of atoms out of the boundary, i.e. flux out of the boundary equals to zero.

Through a series of operations, utilizing Laplace transforms, Mullins obtained solution of the PDE, subject to initial and boundary conditions as,

$$y(x,t) = m(Bt)^{1/4} Z\left[\frac{x}{(Bt)^{1/4}}\right] \tag{2.3.14}$$

defining $u = \frac{x}{(Bt)^{1/4}}$, an analytic solution of the function $Z(u)$ is developed as a power series form,

$$Z(u) = \sum_{n=0}^{n} a_n u^n \tag{2.3.15}$$

As a final step for the complete solution, the values of coefficients a_n were tabulated.

Mullins (1957) also stated that the form of the dependence of y (Eq. (2.3.14)) upon its variables implies a profile shape depending on m, but independent of the time and of the physical parameters comprising B. The linear dimensions of this shape are evidently proportional to $t^{1/4}$. The analysis continued by selecting $(Bt)^{1/4} = 1$ and plotting the normalized profile $y/m = Z(x)$.

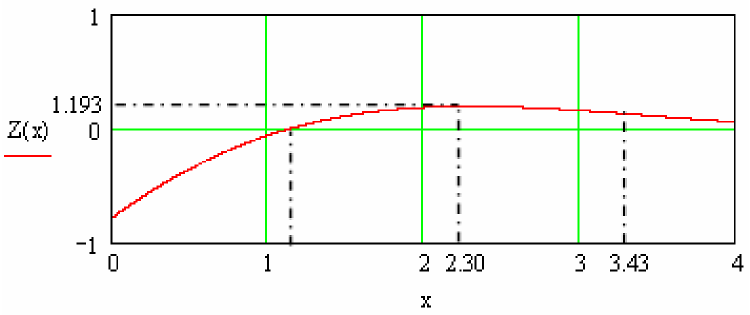

Figure 2.3.1: Normalized profile shape due to surface diffusion.

The zero, the maximum, and the point of inflection are indicated in Fig. 2.3.1. Using Eq. (2.3.14) and the data of Fig. 2.3.1 that the depth of the groove measured in the y direction from the maximum of the surface to the grain boundary is given by,

$$d = 0.973m(Bt)^{1/4} \tag{2.3.16}$$

whereas the seperation of the two maxima is given by,

$$s = 4.6(Bt)^{1/4}. \tag{2.3.17}$$

2.4. Grain Boundary Grooving in Conjunction with Electromigration

Electromigration is the process of current induced self diffusion in metal lines. It is generally considered to be the result of momentum transfer from the electrons, which move in the applied electric field, to the ions which make up the lattice of the interconnect material (Arzt, and Nix, 1991).

When electrons are conducted through a metal, they interact with imperfections in the lattice and scatter. Scattering occurs whenever an atom is out of place for any reason. Thermal energy produces scattering by causing atoms to vibrate. This is the source of resistance of metals. The higher the temperature, the more out of place the atom is, the greater the scattering and the greater the resistivity.

It is generally agreed that the force acting on diffusing atoms whether in bulk or thin films originates from the sum of two contributions, the direct electrostatic force tending to drive ions toward the cathode, and the 'friction force' caused by the momentum exchange between ions and scattered electrons, for electron conductors (electromigration), which tends to cause ionic motion in the opposite direction. The latter (electromigration) effect usually dominates so that atomic drift is towards the anode. The term "electron wind force" generally refers net force on the diffusing ions is given by,

$$F_{total} = F_{direct} + F_{friction} \tag{2.4.1}$$

Whereas an electrostatic analogue for the driving force of electromigration may be expressed as,

$$F_{total} = Z^{*} qE \tag{2.4.2}$$

where q is the electronic charge, E is the electric field, Z^{*} is the effective valance whose magnitude is determined by the competition between the field and electron friction effects. Theoretical estimates and experimentally measured values of Z^{*} have appeared in the literature (Huntington, 1961).

The electromigration ionic drift and atomic diffusion are connected via the Nernst-Einstein relation,

$$v_{drift} = \frac{D_s}{kT} = \frac{D_s Z^{*} qE}{kT} = \frac{D_s Z^{*} q\rho j}{kT} \tag{2.4.3}$$

where, v_{drift} is the drift velocity, D_S is the surface diffusion coefficient, ρ and j are resistivity and current density, respectively, and kT has the usual meaning.

The drift velocity, v_{drift}, will be a function of the diffusion pathway and the temperature dependence of v_{drift} will be characterized by the activation energy of the predominant diffusion mechanism, Q, as shown in the following equation (D_o is the temperature independent pre-exponential);

$$D = D_0 \exp\left(-\frac{Q}{kT}\right) \tag{2.4.4}$$

After a series of operations with appropriate assumptions, just as the derivation of Mullins', the electromigration induced GB grooving found that governed by the following equation (Ohring, 1971),

$$\frac{\partial y_i}{\partial t} + A_i \frac{\partial^3 y_i}{\partial x^3} = 0 \qquad i = 1, 2... \tag{2.4.5}$$

where,

$$A_i = \frac{B_i Z^* e\rho j}{kT} = \frac{D_s \gamma \Omega^2 v Z^* e\rho j}{(kT)^2} \tag{2.4.6}$$

with the similar boundary conditions given for thermal GB grooving problem.

2.5. Further Improvements of Mullins' Theory

After Mullins' published his work in 1957, an extensive effort was performed on the characteristics of the derived partial differential equation, in order to evaluate several cases to understand the groove profile changes under several circumstances.

2.5.1. Finite Slope Consideration

Lots of numerical approaches were developed to get a more general solution and one of them was the finite slope consideration of the equation. In Mullins work, for simplifying the solution small slope approximation was done, by doing this the equation for normal displacement of the surface is linearized. Later, the problem has been extended to finite slopes in several independent studies. Robertson (1971) evaluates the cases of finite slopes ranging from 0 to 4. The main conclusion of this solution is that the groove profile is self similar; the width and height of the groove grow with time t as $t^{1/4}$.

Zhang and Schneibel (1995), Wong *et al.* (1997), and Sun and Suo (1997) obtain similar results.

2.5.2. Grain Boundary Diffusion; The Presence of Grain Boundary Fluxes

If the grain boundaries, which intersect the free surface, do not transport matter, the corresponding profile evolves via surface diffusion under well-known conditions of scale and temperature, as completely discussed above. In this approach the only role of the triple junction present in the system is to maintain the equilibrium angle. However, the presence of GB fluxes I change the surface morphology drastically.

GB grooving with a GB flux in real thin film interconnects is a complex problem. An adequate numerical modeling technique should be capable of managing such issues as GB grooving with an arbitrary flux, and various ratios of GB to surface diffusivities (Khenner *et al*., 2001).

Huang and Yang (1987) studied the surface profiles generated by the electromigration induced surface and GB diffusion in a bicrystal film having a varying surface diffusivity. The grooving solution for a periodic array of GB grooves, each with an external flux, has been studied by Thouless (1993), only for steady state and the small slope case. Klinger *et al.* (1995) examine the case, under isotropic conditions for the intersection of a periodic array of grain boundaries with an external surface for arbitrary GB fluxes. Authors stated that, two modes of surface evolution can occur:

1) For moderate magnitudes of I the entire surface advances or recedes as material is supplied or removed by the intersecting grain boundaries;
2) For sufficiently large magnitudes of I, the GB roots break away from the remaining surface to form rapidly growing ridges $(I > 0)$ or slits $(I < 0)$. The transition from the first to the second mode occurs at limiting values of I which depend on geometry and material parameters Finally they obtain upper and lower limiting values for I (α_+ and α_- respectively), after which a global steady-state profile no longer exists, and conclude with the following remarks:

i. Equilibrium profiles $(I = 0)$: Circular arcs (constant curvature), thus assuring that surface flux vanishes and that the surface remains stationary.

ii. Global steady state profiles $(\alpha_- < I < 0)$ or $(0 > I > \alpha_+)$: More complex curvature determined by the condition that the divergence of the surface flux is uniform over the periodic distance $2L$, thus assuring that the surface flux is displaced at a constant velocity.

iii. Ridge $(I > \alpha_+)$ and slit $(I < \alpha_-)$ profiles: The surface cannot accept or supply sufficient GB flux, thus the groove root breaks away from the remaining surface and assumes the form of a slit or ridge, translating at a constant velocity. Increasing grain size (2L) favors slit-like grooving.

And also creep cavity growth in a GB, a similar problem to GB grooving, was studied by Chuang and Rice (1973), Pharr and Nix (1979), Huang *et al.* (2000) under this consideration.

2.5.3. Effect of Diffusivity Variation

The surface diffusivity D is known to vary with the crystalline orientation. Further quantitative clarification of D in this regard calls for an extremely careful determination of the surface transport (Huang, Yang, 1987). Gungor and Maroudas (2001) adopted a useful functional form for varying surface diffusivity, relying on older studies of Liu (1995), Gungor and Maroudas (1999) and Liu *et al.* (1991).

2.5.4. Effect of Aspect Ratio & Equilibrium Angle

Huang *et al.* (2001) examine GB grooving on a polycrystalline surface by finite element method. They simulate the shape evolution dynamics as a function of equilibrium angle θ, and the initial aspect ratio β of the interconnect line. They found that there is a critical thermal grooving or equilibrium angle $\theta_{\min}$ for given β value. If h < $\theta_{\min}$, the plate cannot split, otherwise, the plate will split along the internal boundary of the plate-like grain. An approximate formulation of $\theta_{\min}$ as a function of β is given based on a number of finite element analyses. The effect of initial termination shape of the plate on $\theta_{\min}$ is also examined, and a weak effect was found. When β > 10, its effect can be neglected. They also stated that when there is no longer a GB exists in the system i.e. the case where the the interconnect break apart into grains, grains will evolve into cylinders directly.

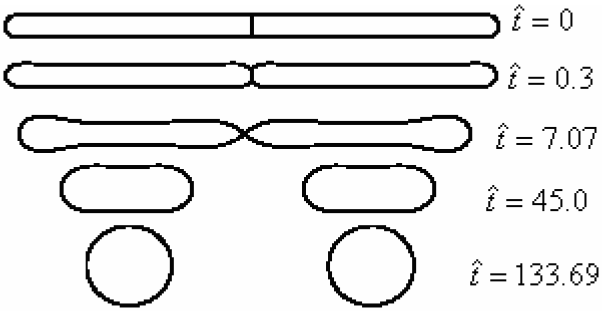

(a) $\beta = 20, \theta = 45^0$

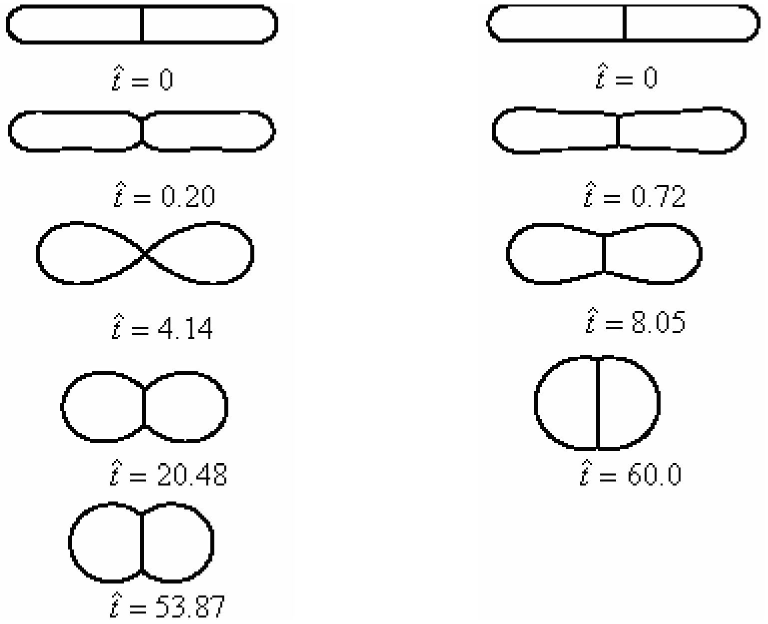

(b) $\beta = 6, \theta = 45^0$ (c) $\beta = 6, \theta = 14.57^0$

Figure 2.4.1: The shape and evolution process of plate-like grains with different initial aspect ratio β and thermal angle θ for a given mobility and surface free energy (Huang *et al.*, 2001).

2.5.5. Effect of Anisotropic Surface Free Energies

Maybe the most serious simplification made in the Mullins model is the assumption of the full isotropy of the surface energy, γ_s. Obviously, this assumption justifies the use of the continuum approach, with the macroscopic curvature as the only driving force for surface diffusion. However, the importance of the surface free energy anisotropy in determining the dihedral angle of the groove and the groove shape was recognized soon after Mullins' original work (Rabkin *et al.*, 2000).

In the case of a coherent twin boundary, it is stated that the surface anisotropy may even cause the formation of a ridge instead of a groove (Mykura, 1961). The evolution of a pre-perturbed surface topography of the vicinal surface, which is essentially anisotropic, was also considered. It was found that the in the small slope approximation, the flux of the surface atoms is again proportional to the gradient of the surface curvature defined in the proper frame of reference, but γ_s should be substituted by a complex expression which depends on the energy of an isolated step, the energy of interaction between steps and the direction of perturbation (Bonzel and Mullins, 1996).

Zhang *et al.* (2002) derive models describing groove growth while the dihedral angle changes. Inevitably the change in the dihedral angle is assumed to be caused by the change in the surface energy. They express γ_s as a function of time, and after a serious of simulations they conclude that changes in the dihedral angle affect the growth exponent for the groove depth much more than the groove width. Growth exponents for depth values as high as 0.4 are possible in this model, whereas Mullins' model predicts an exponent of 0.25 for both the width and depth of the groove.

Xin and Wong (2003) study grooving by capillarity driven surface diffusion with strong surface energy anisotropy and find that faceted grooves still grow with time t with an exponent of 0.25. They stated that, an isotropic groove can be smooth if the groove surface does not cross a facet orientation, moreover the groove has the same shape as the corresponding isotropic groove, but the growth rate is reduced by a factor that depends on the degree of anisotropy.

Recently, Zhang *et al.* (2004) study the effect of anisotropic surface free energy on thermal GB grooving using modeling, simulation and experiments on tungsten. Based on Herring's model they show that, for tungsten, when the anisotropy is mild, the groove profiles are self-similar in the evolution but are often not are in proportion to those developed under isotropic material properties. The grooving kinetics obey power laws with the exponent 0.25. When the anisotropy is critical surface faceting occurs. And, when it is severe the facets coarsen in the evolution. They exhibit the groove profiles in evolution under different degrees of anisotropy.

2.5.6. Migrating Grain Boundary Consideration

When we rewrite the boundary conditions of the evaluated by Mullins, by calling the grain at right hand side as *Grain I*, and the other *Grain II*, matching boundary conditions connect the two solutions at the origin becomes,

$$y_I(0,t) = y_{II}(0,t) \tag{2.5.6.1}$$

$$\left[\frac{\delta y_I(0,t)}{\delta x}\right] - \left[\frac{\delta y_{II}(0,t)}{\delta x}\right] = \frac{\gamma_b}{\gamma_s} \tag{2.5.6.2}$$

$$\frac{\delta^2 y_I(0,t)}{\delta x^2} = \frac{\delta^2 y_{II}(0,t)}{\delta x^2} \tag{2.5.6.3}$$

Again, the first and third of these conditions expresses the continuity of the profile depth and mass flux across the boundary root respectively. The second condition maintains a constant angle between the profile surfaces under the approximation of small slopes. This condition, however; implies that the GB will rotate in the xy plane and may thus migrate. (Allen D.J., 1982). It is not common to observe GB migration in interconnect lines that are operating at relatively low temperatures.

2.5.7. The Temperature Effect

When the temperature gradients are small we end up with Mullins' classical grooving equation. Cases of high temperature gradients were also studied in connection with electromigration problems, Ohring (1971) states that, where the current flows in the direction of increasing temperatures a mass accumulation occurs while conversely mass depletion and thinning occurs where the current flows in the direction of decreasing temperatures.

2.5.8. The Effect of Stress

A theory of the effect of stress on the GB grooving was also developed by Genin *et al*. (1993). The analysis predicts an acceleration of grooving by a tensile stress and offers the possibility of an absolute measurement of the GB diffusion data for mass transport.

2.6. Electromigration Induced Cathode Voiding and Drift

When DC current is applied to a metal interconnect line, electromigration takes place resulting in the depletion or accumulation of metal atoms at the locations where the imbalance of atom fluxes occurs. Over time this net flux of atoms will cause voiding and extrusion in the line which in turn can cause failure of the interconnect.

The standard approach to electromigration testing involves measuring resistance as a function of time for a large number of samples to determine a failure distribution curve based on a predetermined failure criterion. This is typically done at high temperature and high current density and the data are then used to extrapolate what the expected lifetime would be under use conditions. Failure analysis of tested structures can reveal information concerning the failure mechanism, provided the applied current is shut off soon after the sample has failed. Continued testing of samples after failure can cause significant localized damage (e.g., melting) which makes failure analysis much more difficult.

Void growth rate can be estimated by measuring the final void size and dividing by the total testing time. To obtain additional data points, one can either test a large number of samples and stop the test at different times, or one can periodically interrupt the electromigration testing of samples to monitor void growth, however this becomes cumbersome, as it involves repeated heating and cooling of the test structures.

In situ electromigration testing studies enables one to observe void growth as it takes place and therefore make a direct correlation between changes in resistance and physical changes taking place in the test line. Koetter *et al.* (2000) looked at the correlation between void and hillock growth and microstructure in unpassivated physical vapor deposited Cu lines. Lee *et al.* (1995) carried out Blech-type (Blech I. E., 1976) *in situ* drift experiments on 10-µm-wide Ta/Cu/Ta and Ta/Cu(Sn)/Ta sandwich line structures and showed that the addition of Sn reduced drift velocity significantly and also increased the measured electromigration activation energy from 0.73 eV for pure evaporated Cu, to 1.25 eV for a Cu (2 at. % Sn) alloy. Proost *et al.* (2000) have carried out drift experiments on passivated Blech-type test structures looking at the effect of various barrier layers on drift velocity in both polycrystalline and bamboo plated Cu structures. They concluded that drift proceeds at the Cu/barrier layer interface, with the highest drift velocity measured in the case of Ta followed next by TaN and then TiN. Kageyama *et al.* (1998) showed that the texture of Al and Cu lines could be controlled by the texture of the underlying Ti and TiN and that highly $\langle 111 \rangle$ textured Al and Cu showed improved electromigration resistance.

Hu *et al.* (1999) measured void size in unpassivated Cu lines to determine drift velocity as a function of linewidth and sample temperature by occasionally interrupting the testing in order to make void size measurements. For fine lines $(\text{width } < 1\mu m)$ with a bamboo grain structure, an increase in drift velocity was observed with decreasing linewidth suggesting surface diffusion dominated mass transport along the three free surfaces of the lines. For wide lines $(\text{width} > 1\mu m)$ with a polycrystalline grain structure there was a slight increase, then a decrease, and then a leveling off in drift velocity with increasing linewidth due to the secondary contribution of grain boundary diffusion. The tested samples were fabricated using a lift-off technique which differs considerably from today's typical commercial single or dual damascene Cu processing.

Liniger E. *et al.* (2002) studied *in situ* SEM electromigration in dual-damascene electroplated Cu lines to examine the effect of sample temperature and linewidth on the rate of void growth. They observed void growth takes place by consuming grains in a stepwise fashion, either by grain thinning or by an edge displacement mechanism. Surface diffusion was found to be the primary diffusion path for void growth. In addition they stated that, grain boundaries provided a secondary path for copper diffusion in polycrystalline structures and nucleation sites for void growth in bamboo structures. A direct correlation between the test line resistance change and void growth behavior was also presented in their study. Void growth rate was measured as a function of sample temperature and linewidth using a scanning electron microscope. Electromigration activation energy of $0.9 \pm 0.1\,\mathrm{eV}$ was determined for the copper voiding process. The effect of linewidth on void growth rate was also investigated and found to be negligible, consistent with a surface-diffusion dominated model for void growth.

CHAPTER 3

IRREVERSIBLE THERMOKINETIC THEORY OF SURFACES & INTERFACES

3.1. Introduction

Defining the smallest molecular region in which microscopic fluctuations are negligible and whose intensive properties are homogeneous as a *micro-discrete element,* and relying only on the fundamental postulates of linear irreversible thermodynamics of bulk phases as advocated by Prigogine (1961), Ogurtani (2000) develop a novel analytical theory of a network of interfaces that are interconnected by triple junctions which successfully describes the evolution dynamics of ordinary points along an interface (e.g. a free surface) and the displacement kinetics of triple junctions.

Discretization is applied to an open composite system composed three distinct phases, namely the free surface, grain boundary, interconnect where the grain boundary separates interconnect into two different sub domains. Then by applying legitimate limiting and normalization procedures convenient differential equations describing the phenomenon are obtained. The interfacial regions are considered as autonomous, i.e. their thermodynamic properties do not require any special definition, as for bulk phases.

3.2. Internal Entropy Production for Discrete Micro-Elements

Variations taking place in micro-extent (discrete micro-element) are denoted by of Δ space-scaling operator. Following this notation, *the total reversible work* done on a flat surface phase is given by:

$$\delta\Delta w = -\overline{P}d\Delta V_\sigma + \gamma d\Delta A_\sigma \tag{3.2.1}$$

where $\overline{P}$ is the mean isotropic pressure in the layer, and γ is called the surface tension whose value may be given roughly by:

$$\gamma = \int_0^{h_\sigma} Q dz \tag{3.2.2}$$

where Q is the deviatoric part of the stress tensor and h_σ is the thickness of the surface layer and also the integration is performed along the surface normal.

The local anisotropic properties of the medium are now automatically embedded in the intensive variables, which are characterized by second order tensors or dyadics. Hence the Helmholtz free energy for an open surface phase of a micro-extent and embedded in an isotropic media may be written as,

$$d\Delta F_\sigma = -\Delta S_\sigma dT_\sigma - P_\sigma d\Delta V_\sigma + \gamma d\Delta A_\sigma + \sum_i \mu_\sigma^i d\Delta n_\sigma^i - \sum_j \Delta A_\sigma^j d\xi_\sigma^j \tag{3.2.3}$$

where, ΔS_σ denotes the entropy, μ_σ^i denotes the chemical potential, Δn_σ^i is the number of i^{th} chemical species in the micro-element, $d\xi_\sigma^j$ is the extent of the homogeneous j^{th} chemical reaction taking place in the phase under consideration, and ΔA_σ^j is the affinity of the homogeneous j^{th} chemical reaction and is related to the chemical potentials and the stoichiometric numbers as defined by Th. De Donder and Rysselberghe (1936).

For a bulk phase one may rewrite very similar expression for a micro-system namely,

$$d\Delta F_b = -\Delta S_b dT_b - P_b d\Delta V_b + \sum_i \mu_b^i d\Delta n_b^i - \sum_j \Delta A_b^j d\xi_b^j \tag{3.2.4}$$

In the case of a composite system as defined previously, the total Helmholtz free energy differential can be easily written down from Eqs. (3.2.3) and (3.2.4) by using the fact that the extensive thermodynamic quantities are additive.

The entropy of any system whether it is close or open can change in two distinct ways, namely by the flow of entropy due to the external interactions, $d\Delta S_{ex}$, and by the internal entropy production (IEP) due to the changes inside the system, $d\Delta S_{in}$. Symbolically, one may write this as:

$$d\Delta S = d\Delta S_{in} + d\Delta S_{ex} \tag{3.2.5}$$

The entropy increase $d\Delta S_{in}$ due to changes taking place inside the system is positive for all natural or irreversible changes, is zero for all reversible changes and is never negative.

For an open system, in which not only the energy but also the matter exchange takes place between the system and its surroundings, the conservation of energy becomes,

$$\delta\Delta\Phi = d\Delta U - \delta\Delta w = d\left(\Delta F + T\Delta S\right) - \delta\Delta w \tag{3.2.6}$$

where $\delta\Delta\Phi$ is the energy received by the system, in terms of heat and matter transfer processes from the surroundings, $d\Delta U$ is internal energy change, and $\delta\Delta w$ is the reversible work done on the system by external agents, and this work is equal to $-Pd\Delta V$ or $-\left(Pd\Delta V - \gamma d\Delta A\right)$ depending upon whether one deals with the bulk phase or the surface phase, respectively.

For a global composite system having discontinuous phases, the total IEP due to the irreversible processes should include the entropy contributions due to transport of heat and chemical species among various phases of the system. Hence from Eqs. (3.2.3) or (3.2.4) and (3.2.6), one can obtain the following relationship for multi-phase systems with interfaces by first using the additive property of the entropy changes, and then performing a similar splitting procedure as also applied by Prigogine (1961) to the system consists of two open phases but is closed as a whole:

$$\frac{d\Delta S_{in}}{\delta t} = -\sum_{i,k} \frac{\mu_k^i}{T_k} \frac{d\Delta n_k^i}{\delta t} + \sum_k \frac{1}{T_k} \frac{\delta\Delta\Omega_k}{\delta t} + \sum_{j,k} \frac{\Delta A_k^j}{T_k} \frac{d\xi_k^j}{\delta t} \qquad (3.2.7)$$

The expression given by Eq. (3.2.7) is generalized in order to take into account of the existence of the various homogeneous chemical reactions occurring in different phases of a global system. Double summations with respect to *k* and *i* or *j* indicate summation over various phases (bulk or surface), and over different chemical species or reactions taking place simultaneously in the same phase, respectively. $\delta\Delta\Omega_k$ is the amount of energy transported to the individual phase from the other phases present in the global system due to heat or mass transfer, which also employed by Prigogine (1961) in the treatment of lump and close composite systems. The first term in Eq. (3.2.7) represents an additional contribution to the IEP in the composite system due to internal entropy flow associated with the transfer of chemical species from one sub-domain to another sub-domain. One should be noticed that the second term in the entropy production for a composite system immediately drops out for those sub-domains having identical temperatures.

The IEP is not an additive property of a thermodynamic system composed of interacting open sub-systems unless the whole system is in the state of complete physico-chemical equilibrium. Therefore, the rate of entropy flow (REF) should be also formulated in order to calculate global IEP for the whole system, which is composed of a set of discrete but interconnected micro-elements and the embedding matrix, by utilizing summation or integration operation as demonstrated by Ogurtani and Oren (2001).

Similarly, the REF from the surrounding to an open composite system may be written as,

$$\frac{d\Delta S_{ex}}{\delta t} = -\sum_{i,k} \frac{\mu_k^i}{T_k} \frac{d\Delta n_{k\leftrightarrow s}^i}{\delta t} + \sum_k \frac{1}{T_k} \frac{\delta\Delta\Omega_{k\leftrightarrow s}}{\delta t} \text{ (Open composite micro-system) (3.2.8)}$$

where the subscript $_{k\leftrightarrow s}$ indicates that the matter and energy exchange takes place between the phases of the system, k, and the surrounding, s. Here, $\delta\Delta\Omega_{k\leftrightarrow s} / \delta t$ and $d\Delta n_{k\leftrightarrow s}^i / \delta t = J_{k,s}^i$ are, the rate flow of energy and the flux of chemical species *i* to the domain *k* of the composite open micro-system from its surrounding denoted by *s* through the heat and matter exchange processes respectively.

3.3. Internal Entropy Productions Associated With the Virtual Displacements of the Triple Junction and the Ordinary Points

As far as the kinetic behavior of a triple junction is concerned, it is assumed that the whole system is in thermal equilibrium and no insitu chemical reaction is taking place other than the phase transformation occurring between the free surface and the grain boundary region. This last point, which is closely connected with the entropy point source term, up to now, is completely omitted in the literature (Rice and Chuang, 1981) in the formulation of conservation of species (mass balance) in terms of flux balance at the triple junction. In the present theory the sampling domain is a very small composite and discrete open micro-system, which is eventually localized into a point of singularity, and situated just in the immediate neighborhood of the junction as illustrated in Fig. 3.3.1. This selected composite micro-system is also connected to the neighboring micro-discrete elements by nodes where the exchange or the flow of matter only contributes to the REF but nothing to do with the IEP.

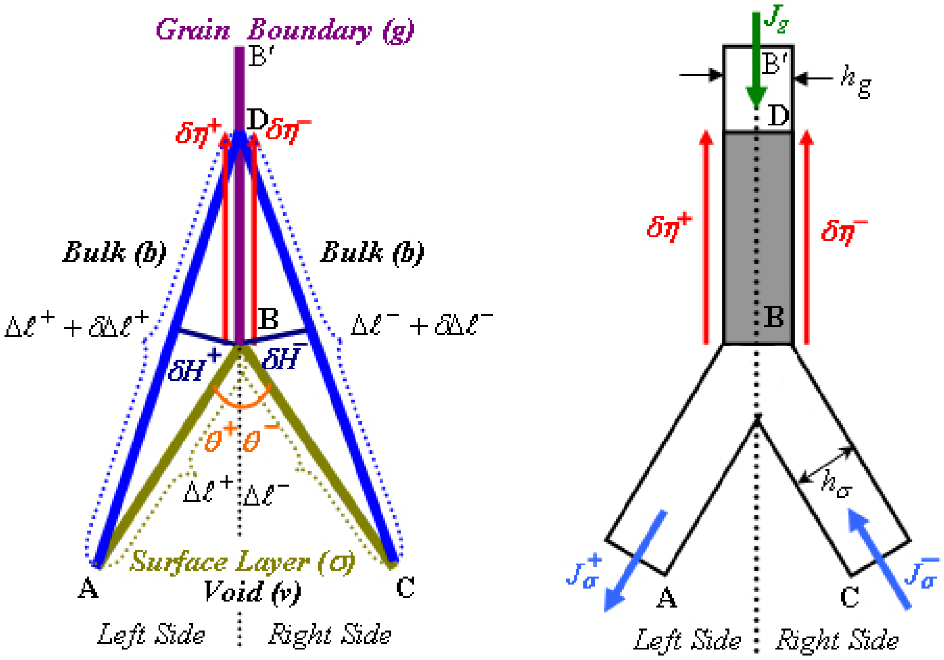

a) b)

Figure 3.3.1: Triple junction longitudinal displacement along the grain boundary. (a) Triple junction macrostructure. (b) Triple junction microstructure. BB′ is the grain boundary, ABC and ADC are the initial and the displaced position of the free surface, respectively, and $\delta\eta$ is the longitudinal virtual displacement of the triple junction along the grain boundary. (Ogurtani and Oren, 2003)

Now, let us calculate the internal entropy variation for the left hand side sub-system when the triple junction moves along the grain boundary with a distance $\delta\eta^+$. From Fig. 3.3.1, one immediately finds the following variational relationships among various quantities by using simple geometric arguments and assuming that: $\Delta\ell^+ >> \delta\eta^+$ and $\Delta\ell^- >> \delta\eta^-$;

$$\delta\Delta\ell^+ = \cos\theta^+\delta\eta^+, \qquad \delta H^+ = \sin\theta^+\delta\eta^+ \tag{3.3.1}$$

$$\delta\Delta n_b^+ = -\frac{1}{2\Omega_b}\Delta\ell^+\sin\theta^+\delta\eta^+, \qquad \delta\Delta n_v^+ = \frac{1}{2\Omega_v}\Delta\ell^+\sin\theta^+\delta\eta^+ \tag{3.3.2}$$

$$\delta\Delta n_\sigma^+ = \frac{h_\sigma}{\Omega_\sigma}\cos\theta^+\delta\eta^+, \qquad \delta\Delta n_g^+ = -\frac{h_g}{2\Omega_g}\delta\eta^+ \tag{3.3.3}$$

where Ω_σ, Ω_g, Ω_b and Ω_v are the mean atomic specific volumes, respectively, associated with free surface, grain boundary, bulk and gaseous phases. $\Delta\ell^+$ and $\Delta\ell^-$ denote segment lengths of the free surface just next to the triple junction right and left hand sides, respectively. h_σ and h_g are the thickness of the surface layer and the grain boundary region and assumed to be invariant. $\delta\Delta n_v^+$ and $\delta\Delta n_b^+$ are the number of atoms gained in the reaction zones associated with the void / interfacial layer, and the bulk / interfacial layer, respectively, while the transformation processes are taking place there during the virtual displacement of the interfacial layer. $\delta\Delta n_g^+$ is the total number of atoms misplaced by the half of the grain boundary during triple junction motion. Similarly, $\delta\Delta n_\sigma^+$ is identically equal to the net atomic gain by the interfacial layer denoted by σ due to enlargement (extension without stretching) of that layer during the displacement operation. δ and Δ are variational and micro-discretization operators, respectively. Eventually, by using a set of novel limiting procedures of calculus, they will be replaced by exact differential, and zero that corresponds to the infinitesimal volume or better to say to the singularity associated with the triple junction.

One can obtain exactly similar expressions for the other side of the triple junction, which will be identified by a negative sign as superscript in the formulas. The following identities are employed in our future formulas; $\Gamma_\sigma = h_\sigma / \Omega_\sigma$ and $\Gamma_g = h_g / \Omega_g$. They correspond to the specific mean atomic densities associated with the free surface and grain boundary, respectively.

By applying the first term of Eq. (3.2.7) that is the only term that does not vanish to the left and right side sub-composite systems, the IEP generation can be calculated for any arbitrary virtual displacement of the triple junction along the grain boundary. Also, one should recall that in the case of multi-component system, the variations in the number of atomic species could be easily obtained by simply multiplying the total atomic number variations by the respective atomic fractions denoted by x_j^i. As an example, the number of chemical species involved in the left hand side bulk phase due to the virtual displacement may be given by

$$\delta\Delta n_b^{i+} = x_b^i \delta\Delta n_b^+ = \frac{x_b^i}{2\Omega_b}\Delta\ell^+ \sin\theta^+ \delta\eta^+ \qquad (3.3.4)$$

One can than rigorously write down the rate of entropy production due to triple junction virtual displacement for the left as well as for the right hand side domains using Eqs. (3.2.7, 3.3.1-3.3.4). In the case of left hand side it is denoted by the following formula:

$$\frac{\delta\Delta S_{in}^+}{\delta t} = \frac{1}{T}\left\{ \begin{array}{l} \sum\limits_i \left(\frac{x_b^{i+}}{\Omega_b}\mu_b^{i+} - \frac{x_v^{i+}}{\Omega_v}\mu_v^{i+}\right)\frac{1}{2}\Delta\ell^+ \sin\theta^+ \\ +\frac{\Gamma_g}{2}\sum\limits_i x_g^i \mu_g^i - \Gamma_\sigma \cos\theta^+ \sum\limits_i x_\sigma^{i+}\mu_\sigma^{i+} \end{array} \right\} \frac{\delta\eta^+}{\delta t} \qquad (3.3.5)$$

In above relationship, we have employed special subscript, $^+$, above the atomic fractions as well as the chemical potentials related to the surface phase in order to indicate explicitly that those quantities may depend upon the orientation of the local surface normal. One should also recall that for the multi-component surface phases, $\sum \Gamma_\sigma^i \mu_\sigma^i$, and $\sum \Gamma_g^i \mu_g^i$ are exactly equal to the specific Gibbs free energy densities associated with the free surface, and the grain boundary, respectively. They will be denoted by g_σ and g_g. Here, $\Gamma_\sigma^i = \Gamma_\sigma x_\sigma^i$, and $\Gamma_g^i = \Gamma_g x_g^i$ are by definition known as the specific surface concentration of chemical species in surface layer, and the grain boundary, respectively.

The terms appearing in the first group on the right side of Eq. (3.3.5) such as, $\sum x_b^i \mu_b^i / \Omega_b$ and $\sum x_v^i \mu_v^i / \Omega_v$ are the volumetric Gibbs free energy densities. These quantities are denoted by $\breve{g}_b$ and $\breve{g}_v$, and associated with the bulk phase and gaseous region having their own instantaneous compositions just next to the hypothetical geometric boundaries of the interfacial layer (reaction fronts or zones). Furthermore, these quantities are related to the specific Gibbs free energy densities by the relationship: $g_\sigma = h_\sigma \breve{g}_\sigma$.

By dividing both sides by δt, and then taking consecutive limiting procedures first with respect to $\delta t \to 0$, and then $\Delta\ell \to 0$, one immediately obtains the following differential equations representing IEP associated with the virtual displacement of the left and right sides of the triple junction singularity,

$$\lim_{\substack{\delta t\to 0\\ \Delta\ell\to 0}} \frac{\delta\Delta S_{in}^{+}}{\delta t} = \frac{d\Delta\hat{S}_{in}^{+}}{dt} = \frac{1}{T}\left(\frac{1}{2}g_g - g_\sigma^{+}\cos\theta^{+}\right)\frac{d\eta^{+}}{dt} \quad (\text{erg}/{}^{\circ}\text{K/cm/sec}) \qquad (3.3.6)$$

and

$$\lim_{\substack{\delta t\to 0\\ \Delta\ell\to 0}} \frac{\delta\Delta S_{in}^{-}}{\delta t} = \frac{d\Delta\hat{S}_{in}^{-}}{dt} = \frac{1}{T}\left(\frac{1}{2}g_g - g_\sigma^{-}\cos\theta^{-}\right)\frac{d\eta^{-}}{dt} \quad (\text{erg}/{}^{\circ}\text{K/cm/sec}) \qquad (3.3.7)$$

On the left sides of above expressions, the symbol, ^, has been tacitly employed to emphasize that these entropy production terms are line source in three dimensional space. Superscripts over the specific Gibbs free energies indicate that those quantities may depend upon the orientation of the local surface normal vector.

The entropy production for the combined system can be easily calculated using above arguments for the virtual displacement of the triple junction along the grain boundary. The result is as follows:

$$\frac{\delta\Delta S_{in}^{g\sigma}}{\delta t} = \frac{\delta\Delta S_{in}^{+}}{\delta t} + \frac{\delta\Delta S_{in}^{-}}{\delta t} = \frac{1}{T}\left\{\begin{matrix} -\frac{1}{2}\left(\breve{g}_{vb}^{+}\Delta\ell^{+}\sin\theta^{+} + \breve{g}_{vb}^{-}\Delta\ell^{-}\sin\theta^{-}\right) \\ +\left[g_g - \left(g_\sigma^{+}\cos\theta^{+} + g_\sigma^{-}\cos\theta^{-}\right)\right] \end{matrix}\right\}\frac{\delta\eta_g}{\delta t} \ge 0 \qquad (3.3.8)$$

which yields IEP due to longitudinal displacement of the triple junction along the grain boundary, after applying the consecutive limiting procedures as described previously,

$$\frac{d\hat{S}_{in}^{g\sigma}}{dt} = \frac{1}{T}\left[g_g - \left(g_\sigma^+ \cos\theta^+ + g_\sigma^- \cos\theta^-\right)\right]\frac{d\eta_g}{dt} \geq 0 \tag{3.3.9}$$

where $\breve{g}_{vb} = (\breve{g}_v - \breve{g}_b)$, and it corresponds by definition to the volumetric density of Gibbs Free Energy of Transformation (GFET) (negative of the affinity of an interfacial reaction such as condensation or adsorption, $g_{vb} > 0$) associated with the transformation of the bulk phase into the gaseous phase which contains chemical species even though they are present in a trace amount. In the case of thermostatic equilibrium between a gaseous phase and an adjacent bulk phase, GFET becomes identically equal to zero, if the reaction front would be a flat interface. There is a very simple connection between this quantity GFET and the Specific Gibbs Free Energy of transformation g_{vb} (evaporation or desorption, g_{vb}<0) between the parent phase and gaseous phase that may be given by $g_{vb} = \breve{g}_{vb} h_\sigma$.

One should also mentioned here that IEP density associated with the virtual displacement of an ordinary point along the normal direction of free surface can be also deduced from Eq. (3.3.8) by the application of proper and rigorous mathematical manipulations. Namely, first taking out the contribution due to the grain boundary interaction, and furthermore recognizing that the displacement motion of the curved interface takes place along the local surface normal vector. Since the right and the left hand segments around the selected ordinary point can be chosen arbitrarily, we may take them equal in length that automatically results identical take off angles between the surface normal and the right and the left segments. Now if one applies the limiting procedure such as; $\Delta\ell \to 0$ and $\delta t \to 0$, then the following rigorous continuum relationship may be obtained, by recalling that the definition of the local radius of curvature $\rho = \kappa^{-1}$,

$$\kappa = \lim_{\Delta\ell \to 0} \frac{\cos\theta}{\Delta\ell / 2} \tag{3.3.10}$$

Similarly $\lim\limits_{\Delta\ell \to 0}$ results $\theta = \pi / 2$. Hence, using above described limiting quantities in Eq. (3.3.13), one may deduce the following expression for the internal entropy production density (the entropy source term) associated with ordinary points:

$$\frac{d\hat{S}_{\text{int}}}{dt} = -\frac{1}{T}\left(\breve{g}_{vb} + g_{\sigma}\kappa\right)\frac{d\eta}{dt} \ge 0 \quad (\text{erg}/{}^{o}\text{K/cm}^{2}\text{/sec}) \tag{3.3.11}$$

There is a certain freedom exists in the choice of fluxes and forces, because the entropy production can be split in several ways into fluxes and forces as clearly demonstrated by De Groot (1951). The interpretation of the first set of forces and fluxes is rather abstract and they may be also called as the affinities in the field of irreversible thermodynamics. On the other hand, the second set can be easily understood in terms of *ordinary drag force* versus *velocity* concept, and their physical interpretation is rather straight forward, but its validity is rather restricted to the systems that are in complete thermal equilibrium and the processes are isothermal. Since it has been assumed on the on set that there is a thermal equilibrium in the system, we may rather use a direct and more plausible approach for the triple junction singularity, namely the concept of power dissipation in the close sense of classical mechanics, and sometimes it is called Helmholtz dissipation function (Haase, 1969). This concept is also advocated and extensively used by Ogurtani and Seeger (1983) in the general formulation of internal friction and dislocation damping phenomenon associated with atomic hopping motions in discrete body centered cubic lattice, that is exposed to the interaction fields which are inhomogeneous in space and fluctuating in time. The power dissipation function is simply given by the internal entropy production multiply by the temperature for an isothermal system, and for the present case obviously it is identically equal to driving force velocity product, namely:

$$T\frac{d\hat{S}_{in}^{\pm}}{dt} = \widehat{F}^{\pm}\frac{d\eta^{\pm}}{dt} \ge 0 \quad (\text{erg/cm/sec}) \tag{3.3.12}$$

Hence comparing this expression with Eq. (3.3.6) one can immediately deduce the generalized force for the left side as;

$$\widehat{F}^{+}=\left(\frac{g_g}{2}-g_{\sigma}^{+}\cos\theta^{+}\right)\quad \text{(dyne/cm)} \tag{3.3.13}$$

and similarly by comparing the Eq. (3.3.12) with Eq. (3.3.7) one can write down an equivalent expression, for the right side;

$$\widehat{F}^{-}=\left(\frac{g_g}{2}-g_{\sigma}^{-}\cos\theta^{-}\right)\quad \text{(dyne/cm)} \tag{3.3.14}$$

These generalized forces are associated with the net material flow during the triple junction longitudinal displacement along the grain boundary without making any distinction between intrinsic fluxes related to the individual chemical species. They are also given in terms of per unit length, because in our formulation of the IEP, a sample of unit length in thickness is chosen. In the phenomenological relationship between velocity and force, one may prefer to use the force acting on a single atomic particle. Therefore above expressions for generalized forces should be multiplied by an atomic length, d_a, which may be taken as equal to the interatomic distance along the sample thickness. Hence, the connection between the triple junction velocity and the atomic generalized force can be now written by introducing the phenomenological mobility coefficient $\Re^{long}/kT$,

$$\frac{d\eta^{+}}{dt}=\frac{\Re^{long}d_a}{kT}\left(\frac{g_g}{2}-g_{\sigma}^{+}\cos\theta^{+}\right) \tag{3.3.15}$$

and

$$\frac{d\eta^{-}}{dt}=\frac{\Re^{long}d_a}{kT}\left(\frac{g_g}{2}-g_{\sigma}^{-}\cos\theta^{-}\right) \tag{3.3.16}$$

where, the same mobilities for both sides are employed. One can now immediately formulate the atomic fluxes coming from the triple junction towards the both sides of the free surface. These are simply given by the number of atoms present in a volume swept by the triple junction motion along the grain boundary per unit time, and plus the incoming grain boundary atomic flux $\hat{J}_g$ (#/cm.sec) associated with the long-range drift-diffusion. Since, the velocity of the triple junction is proportional with the net flux accumulated or depleted at the junction, one can write the following expressions;

$$\frac{d\eta_g^+}{dt} = \frac{2}{\Gamma_g}\left(\hat{J}_\sigma^+ - \hat{J}_g/2\right) \qquad \text{and} \qquad \frac{d\eta_g^-}{dt} = -\frac{2}{\Gamma_g}\left(\hat{J}_\sigma^- + \hat{J}_g/2\right) \tag{3.3.17}$$

Using these expressions in Eqs. (3.3.15) and (3.3.16) for the triple junction velocities, one gets immediately the following generalized conjugate fluxes:

$$\widehat{J}_\sigma^+ = \Gamma_g \frac{\Re^{long} d_a}{2kT} g_\sigma^+ \left(\lambda^+ - \cos\theta^+\right) + \hat{J}_g/2 \tag{3.3.18}$$

and

$$\widehat{J}_\sigma^- = -\Gamma_g \frac{\Re^{long} d_a}{2kT} g_\sigma^- \left(\lambda^- - \cos\theta^-\right) - \hat{J}_g/2 \tag{3.3.19}$$

where one takes the sample thickness as one unit length, and also considers the right and left sub-domains separately by splitting the grain boundary diffusion flux equally. At this stage one can immediately write down the expression for the velocity of the triple junction either directly from Eq. (3.3.9), or applying the law of conservation of species to the displacement motion of triple junction, and utilizing Eqs. (3.3.18) and (3.3.19) for the out-going fluxes from the transformation front:

$$v_g^{long} = \frac{d\eta_g}{dt} = \left(\widehat{J}^+ - \widehat{J}^- - \widehat{J}_g\right)\frac{1}{\Gamma_g} = \frac{\Re^{long} d_a}{2kT}\left[g_g - \left(g_\sigma^+ \cos\theta^+ + g_\sigma^- \cos\theta^-\right)\right] \tag{3.3.20}$$

In above flux relations, λ^- and λ^+ are very important parameters which may be assumed to be constant and equal especially in the case of isotropic behavior of surface phases. They may be called as the wetting parameters and are given by the following expressions: $\lambda^- = \frac{g_g}{2g_\sigma^-}$ and $\lambda^+ = \frac{g_g}{2g_\sigma^+}$. The specific Gibbs free energy of the free surface may depend on the orientation of the local surface normal due to the anisotropic behavior of the surface tension γ and/or the specific Helmholtz free energy itself in crystalline solids (Defay et al., 1966).

In above expressions, a phenomenological mobility coefficient has been introduced and denoted by $\Re^{long}$, which may be called as the reaction rate constant associated with the phase transformation denoted symbolically by $\sigma \Leftrightarrow gb$. For the present case, it refers a transformation, which takes place continuously and reciprocally between two surface phases, namely, between the free surface and the grain boundary region just at the triple junction. This phenomenological mobility does not make any distinction between individual chemical species and their rate of transfer over the activation energy barrier. It is strongly dependent on the temperature, and that may be formulated according to the activated complex rate theory of chemical reactions (Yeremin, 1979) as follows:

$$\Re^{long} = \left(\frac{kT}{h}\right)\exp\left(-\frac{\Delta G^*_{\sigma,g}}{kT}\right) \tag{3.3.21}$$

In above expression $\Delta G^*_{\sigma,g}$ is the Gibbs free energy of activation for the transformation of surface phase into the grain boundary phase or vice versa. Eq. (3.3.20) clearly shows that in the case of thermostatic equilibrium at the triple junction, the displacement velocity becomes identically equal to zero regardless the magnitude of the grain boundary flux. Thermostatic equilibrium establishes when the dihedral angles have reached those values, which make generalized forces given in Eqs. (3.3.13) and (3.3.14) identically equal to zero, under the assumed constrain on the triple junction, namely no lateral motion is possible. Similarly in above equation, the fluxes associated with the surface diffusion, they may go through certain modifications in the case of anisotropic behavior of the free surface as demonstrated by Ogurtani and Oren (2001) and Oren and Ogurtani (2002). In the case of isotropic specific Gibbs free energies, namely $g_\sigma^+ = g_\sigma^- = g_\sigma$, Eq. (3.3.20) may be written in the following form by utilizing the dimensionless parameter λ, which is given by $\lambda = g_g/(2g_\sigma)$.

$$v_g^{long} = \frac{\Re^{long} d_a g_\sigma}{2kT}\left[2\lambda - \left(\cos\theta^+ + \cos\theta^-\right)\right] \quad \text{(cm/sec)} \tag{3.3.22}$$

One can easily show, using the technique developed in this section that the internal entropy production associated with the transverse virtual displacement of the triple junction, namely the motion perpendicular to the grain boundary, may be given by the following rigorous relationship;

$$\frac{\delta\Delta S_{in}^{trans}}{\delta t} = -\frac{1}{T}\left\{\begin{matrix}\frac{1}{2}\left(\breve{g}_{vb}^{+}\Delta\ell^+ \cos\theta^+ - \breve{g}_{vb}^{-}\Delta\ell^- \cos\theta^-\right) \\ +g_\sigma^+ \sin\theta^+ - g_\sigma^- \sin\theta^-\end{matrix}\right\}\frac{\delta\eta^{trans}}{\delta t} \geq 0 \tag{3.3.23}$$

from which one can deduce the following expression for the triple junction singularity by imposing the limiting procedures such as; $\Delta t \to 0$ and $\Delta\ell^\pm \to 0$. Hence, the internal entropy production for the transverse motion of the triple junction along the designated positive direction becomes;

$$\frac{d\hat{S}_{in}^{trans}}{dt} = -\frac{1}{T}\left(g_\sigma^+ \sin\theta^+ - g_\sigma^- \sin\theta^-\right)\frac{d\eta^{trans}}{dt} \geq 0 \tag{3.3.24}$$

Since, it is assumed that the composite system is under the thermal equilibrium condition, according to Eq. (3.3.24) the projection of the dissipative force acting along the direction perpendicular to the grain boundary may be given by

$$F^{trans} = g_\sigma^- \sin\theta^- - g_\sigma^+ \sin\theta^+ \quad \text{(dyne/cm)} \tag{3.3.25}$$

This relationship together with Eq. (3.3.20) clearly shows that triple junction without having any constrain (completely free junction) can be in complete physico-chemical equilibrium configuration if and only if the specific interfacial Gibbs free energies associated with the grain boundary and the both sides of the free surface satisfy a *Nil Vectorial Summation Rule,* which may represented by the following equation; $\vec{g}_g + \vec{g}_\sigma^+ + \vec{g}_\sigma^- = 0$. We should mentioned here that the similar vectorial connection exist among the surface tensions γ associated with the intersecting interfaces in order to have a mechanical equilibrium at the triple junction, which is also known as Young formula in the literature (Young, 1805).

Above findings related to the transverse virtual motion of the triple junction is very important if one considers a more general problem where the grain boundary migration occurs as a result of some thermally activated processes. In that situation, the transverse component of the triple junction velocity according to Eq. (3.3.25) may be given by the following expression;

$$v_g^{trans} = \frac{\Re_g^{trans}}{kT} d_a \left(g_\sigma^- \sin\theta^- - g_\sigma^+ \sin\theta^+ \right) \quad \text{(cm/sec)} \qquad (3.3.26)$$

where d_a is the atomic distance and $\Re_g^{trans} / kT$ is the triple junction transverse migration mobility, and it is a phenomenological coefficient depending upon the temperature of the system through an activation energy barrier.

In the case of lateral constraint on the grain boundary motion, the generalized lateral force now generates a particle flow at and through the triple junction along the free surface to establish thermostatic equilibrium configuration there by adjusting orientations of the neighboring left and right micro-elements. The conjugate particle flux (transverse flow) associated with this force can be immediately written as;

$$\hat{J}_\sigma^{trans} = -Sign(\psi)\Gamma_g \frac{\Re_g^{trans}}{kT} d_a \left(g_\sigma^- \sin\theta^- - g_\sigma^+ \sin\theta^+ \right) \quad \text{(\#/cm.sec)} \qquad (3.3.27)$$

In above expression the angle ψ denotes the amount of rotation of the microelements adjoint to the triple junction in the anti-clockwise direction, and Sign is the usual sign function. A close inspection of above flux expression reveals that the direction of which as such that it tries to eliminate any deviation from the thermostatic equilibrium at the triple junction through the dihedral angles readjustment by transferring mass from one side to another. Where, the direction of mass flow is always towards the establishment of the thermostatic equilibrium configuration, as one expects a priory from very meaning of the postulate of positive internal entropy production in the irreversible thermodynamics.

3.4. Global Internal Entropy Production Associated With the Virtual Displacement of an Interface Interacting With Grain Boundaries

During the derivation of the formula for the global IEP (GIEP) associated with the arbitrary virtual displacement, $d\eta / dt$, of the interfacial loop of a finite thickness, which separates gaseous phase denoted by v from the bulk matrix having multi-components, one has to integrate the rate of local entropy density change along the curved interphase in order to obtain desired connection between generalized forces and conjugate fluxes. The rate of local entropy density change is the only quantity, which has the additive property that allows to be integrated. Therefore, not only the local internal entropy production (source term) given by Eq. (3.3.11), but also the external entropy flow term should be evaluated for the virtual displacement of an interface. The linear combination of these two terms, which may be called the rate of local entropy density change, is given by the following expression in the case of isothermal processes; where the last term represents REF, which can be immediately obtained from Eq. (3.2.8):

$$\frac{\partial \hat{S}}{\partial t} = -\frac{1}{T}\left\{\left(\breve{g}_{vb} + g_{\sigma}\kappa\right)\frac{d\eta}{dt} + \Omega_{\sigma}\left[\frac{\partial}{\partial \ell}\left(\breve{g}_{\sigma} J_{\sigma}\right) + \breve{g}_{\sigma}(\hat{J}_b + \hat{J}_v)\right]\right\} \tag{3.4.1}$$

where, $\hat{J}_v$ and $\hat{J}_b$ are the total atomic fluxes in such directions that they are perpendicular and oriented towards the interfacial layer, just at the reaction fronts between the gaseous phase and free surface and the bulk and the interfacial layer, respectively. Since the evaporation region can be assumed to be a homogeneous system having zero gradient of intensive variables, it can only generate a finite flux at the dividing interface next to the interfacial layer during the virtual displacement, due to the condensation or evaporation processes.

The first group of terms in the above expression represents the IEP density (the entropy source for a ordinary point virtual displacement). The second group of terms similarly represents, respectively, the divergence of the surface entropy flow (DEF) and the possible contribution due to lateral flow of entropy due to exchange of chemical species between bulk phase and interface and/or gaseous phase and the interface (evaporation and condensation), assuming that the interfacial layer is a completely open system, and the displacement process is isothermal. In order to calculate the global rate of entropy change of the whole curved interfacial layer, which is between the gaseous and the bulk phases, let us first take the line integral of Eq. (3.4.1) all along the closed curved interface, excluding any possible singularity such as a triple junction that may be situated at a point denoted by the open interval $(-\varepsilon,\varepsilon)$ when $\varepsilon \to 0$:

$$\begin{aligned}\int_{+\varepsilon}^{-\varepsilon} d\ell \frac{\partial \hat{S}}{\partial t} &= \lim_{\varepsilon\to 0} \oint_{\varepsilon} d\ell \frac{\partial \hat{S}}{\partial t} \\ &= -\frac{1}{T} \lim_{\varepsilon\to 0} \left\{ \oint_{\varepsilon} d\ell \left[\left(\breve{g}_{vb} + g_{\sigma}\kappa \right) \frac{d\vec{\eta}}{dt} + \Omega_{\sigma} \left(\frac{\partial}{\partial \ell} \left(\breve{g}_{\sigma} J_{\sigma} \right) + \breve{g}_{\sigma} \hat{J}_{vb} \right) \right] \right\}\end{aligned} \tag{3.4.2}$$

The entropy source terms associated with the normal components of the atomic flows are considered as coming from the bulk phase, and the open void region (region formed by grooving) due to condensation or evaporation processes which may be summarized by $\hat{J}_{vb} = \hat{J}_v + \hat{J}_b$. Hence, one may have the following rigorous expression (even both phases may be in condensed states such as the precipitation of second phase particles in supersaturated alloy matrixes) for the conservation of atomic species during the virtual displacement of curved interphases having no stretching and thickness variations:

$$\left[(c_b - c_v) - h_\sigma \bar{\kappa} c_\sigma\right]\frac{d\eta}{dt} = \sum_i \frac{\partial J^i_\sigma}{\partial \ell} - \sum_i (\hat{J}^i_b + \hat{J}^i_v) = \frac{\partial J_\sigma}{\partial \ell} - \hat{J}_{bv} \tag{3.4.3}$$

where c_b, c_v and c_σ are the atomic volumetric concentrations associated with the bulk, gaseous and surface phases, respectively. Gaseous phase may be treated as polyatomic dilute gas, such as: $c_v = 0$, and $\bar{\kappa} h_\sigma = 0$. One would get the following result using the fact that $\Omega_b = c_b^{-1}$, which is mostly adapted in the literature (Ogurtani and Oren, 2001; Guggenheim, 1959;Wang and Suo, 1996):

$$\frac{d\eta}{dt} = \hat{n}\cdot\frac{\partial \vec{r}}{\partial t} = \Omega_b\left(\frac{\partial J_\sigma}{\partial \ell} - \hat{J}_{vb}\right) \tag{3.4.4}$$

where, $\vec{n}$ and $\vec{r}$ are the surface normal and the position vectors, respectively.

Then, one can write down the following relationship by substituting Eq. (3.4.4) into the integrated entropy expression Eq. (3.4.2), to obtain the following expression:

$$\int_{+\varepsilon}^{-\varepsilon} d\ell \frac{\partial \hat{S}}{\partial t} = -\frac{\Omega_\sigma}{T} \lim_{\varepsilon \to 0} \left\{ \begin{array}{l} \displaystyle\int_{+\varepsilon}^{-\varepsilon} d\ell \left[(\breve{g}_{vb} + g_\sigma \kappa) \frac{\partial J_\sigma}{\partial \ell} \right] - \int_{+\varepsilon}^{-\varepsilon} d\ell \left[(\breve{g}_{vb} + g_\sigma \kappa) \hat{J}_{vb} \right] \\ \displaystyle + \int_{+\varepsilon}^{-\varepsilon} d\ell \frac{\partial}{\partial \ell} (\breve{g}_\sigma J_\sigma) + \int_{+\varepsilon}^{-\varepsilon} d\ell \left(\breve{g}_\sigma \hat{J}_{vb} \right) \end{array} \right\} \tag{3.4.5}$$

The first and the third group of terms on the right side of above relationship can be integrated by parts, which result;

$$\frac{d}{dt}\int_{+\varepsilon}^{-\varepsilon} d\ell\hat{S} = \frac{\Omega_\sigma}{T}\lim_{\varepsilon\to 0}\left\{\begin{array}{l} \displaystyle\int_{+\varepsilon}^{-\varepsilon} d\ell\left[J_\sigma\frac{\partial}{\partial\ell}\left(\breve{g}_{vb}+g_\sigma\kappa\right)\right]-\left[\left(\breve{g}_{vb}+g_\sigma\kappa\right)J_\sigma\right]_{+\varepsilon}^{-\varepsilon} \\ \displaystyle+\int_{+\varepsilon}^{-\varepsilon} d\ell\left[\left(\breve{g}_{vb}+g_\sigma\kappa\right)\hat{J}_{vb}\right]-\left[\breve{g}_\sigma J_\sigma\right]_{+\varepsilon}^{-\varepsilon}-\int_{+\varepsilon}^{-\varepsilon} d\ell\left(\breve{g}_\sigma\hat{J}_{vb}\right) \end{array}\right\} \tag{3.4.6}$$

Now, we can split the rate of global entropy change into two parts, namely the global IEP term and the REF term by carefully inspecting the individual contributions in Eq. (3.4.6). Hence, one can write for the global IEP term is as follows:

$$\frac{d}{dt}S_{IEP} = \frac{\Omega_\sigma}{T}\underset{\varepsilon\to 0}{\ell im}\left\{\begin{array}{l} \displaystyle\int_{+\varepsilon}^{-\varepsilon} d\ell\left[J_\sigma\frac{\partial}{\partial\ell}\left(\breve{g}_{vb}+g_\sigma\kappa\right)\right]+\int_{+\varepsilon}^{-\varepsilon} d\ell\left[\left(\breve{g}_{vb}+g_\sigma\kappa\right)\hat{J}_{vb}\right] \\ -\left[\left(\breve{g}_{vb}+g_\sigma\kappa\right)J_\sigma\right]_{-\varepsilon}+\left[\left(\breve{g}_{vb}+g_\sigma\kappa\right)J_\sigma\right]_{+\varepsilon} \end{array}\right\} \tag{3.4.7}$$

Similarly, we can collect those terms in Eq. (3.4.6), which are clearly related to the rate of entropy flow or in another word the external entropy contribution associated with the free surface phase excluding the triple junction as a singularity. Hence, one may write:

$$\frac{d}{dt}S_{REF} = \frac{\Omega_\sigma}{T}\underset{\varepsilon\to 0}{\ell im}\left\{-\int_{+\varepsilon}^{-\varepsilon} d\ell\left(\breve{g}_\sigma\hat{J}_{vb}\right)-\left[\breve{g}_\sigma J_\sigma\right]_{-\varepsilon}+\left[\breve{g}_\sigma J_\sigma\right]_{+\varepsilon}\right\} \tag{3.4.8}$$

In these expressions $\smile$ indicates volumetric densities and ^ denotes the bulk flux intensities (#/cm^2.sec). Here, $J_\sigma = \sum_i J_\sigma^i$ denotes the sum-over surface atomic fluxes (#/cm.sec) in the interfacial layer. Similarly, $\hat{J}_b = \sum_i \hat{J}_b^i$ and $\hat{J}_v = \sum_i \hat{J}_v^i$ are the total atomic flux densities normal to the interface, and they are coming from the adjoint bulk and gaseous phase, respectively. As far as the definition of fluxes is concerned, the lattice structure is assumed to be the reference system in our treatment, therefore existence of vacancies and their flow $\hat{J}_V$ is automatically considered in this representation. In those phases (i.e., bulk and interface regions) with well-defined crystal structures, the lattice vacancies (especially athermal vacancies) should be regarded as independent chemical species in the summation operation dealing with respective Gibbs free energies even though their chemical potentials become identically equal to zero when thermodynamic equilibrium established in the system. One should remember that we are using the postulate of conservation of lattice sites rather than the real chemical species in the crystalline materials as long as there is no sink and source for annihilation and generation of intrinsic point defects such as mono-vacancies in the domain of interest as first mentioned by Bardeen and Herring (1951). However, in the total atomic flux calculations relevant summation operations do not include vacancies, but rather one would have following rigorous identities; $\hat{J}_b^V = -\hat{J}_b$ and $J_\sigma^V = -J_\sigma$, where superscript, ^{V}, denotes vacancy flux density in the relevant phase assuming that it has a crystalline structure, otherwise no such connection can have any meaning.

In the absence of any possible singularity, the last two terms of Eq. (3.4.7) and (3.4.8) become identically zero and drops out completely. Then the integrated internal entropy production, given by Eq. (3.4.7), immediately results in the following expressions for the generalized forces utilizing the fundamental connection between conjugated forces and fluxes by considering the additional contribution due to the external forces $\vec{F}_{Ext}$ as formulated in the Appendix-B of Ogurtani and Oren (2001) namely,

$$F_\sigma = \Omega_\sigma \left\{ \frac{\partial}{\partial \ell} \left[\frac{1}{T} \left(\breve{g}_{vb} + g_\sigma \kappa \right) \right] + \vec{t} \cdot \vec{F}_{Ext} \right\}, \tag{3.4.9}$$

and

$$F_{vb} = \Omega_\sigma \left\{ \left[\frac{1}{T} \left(\breve{g}_{vb} + g_\sigma \kappa \right) \right] + \vec{n} \cdot \vec{F}_{Ext} \right\}, \qquad \text{(valid for ordinary points)} \tag{3.4.10}$$

where F_σ and F_{vb} denote longitudinal and transverse generalized forces that are acting on the interfacial layer respectively. $\vec{t}$ and $\vec{n}$ denote unit tangent and normal vectors at the free surface, respectively. The last contribution in Eq. (3.4.10) becomes identically zero since the normal component of the electric field intensity and the traction are all vanish at the free surface. Then, it can immediately be written down the conjugate fluxes associated with the above forces using the conventional approach in the irreversible thermodynamics of linear (isothermal) processes exposed to conservative external force fields as;

$$J_\sigma = \frac{\mathrm{M}_\sigma}{kT}\Omega_\sigma \frac{\partial}{\partial \ell}\left[\left(\breve{g}_{vb} + g_\sigma \kappa\right) - \left\langle eZ^* \right\rangle \frac{\vartheta}{\Omega_\sigma} + \left\langle \bar{\bar{\lambda}} \right\rangle \otimes \bar{\bar{\sigma}}\right] \qquad \text{(surface flux)} \qquad (3.4.11)$$

and

$$\widehat{J}_{vb} = \frac{\mathrm{M}_{vb}}{kT}\Omega_\sigma \left(\breve{g}_{vb} + g_\sigma \kappa\right) \qquad \text{(incoming net lateral flux density)} \qquad (3.4.12)$$

where, the cross-coupling terms between generalized forces and fluxes have also been neglected. M_σ / k and M_{vb} / k are generalized phenomenological mobilities associated with the respective conjugated forces and fluxes, and k is Boltzmann's constant. $\left\langle \bar{\bar{\lambda}} \right\rangle$ and $\left\langle eZ^* \right\rangle$ are the mean values of the elastic dipole tensor and the effective electromigration charge associated with the interacting species, respectively. Double bars in the expressions indicate tensor quantities, and $\otimes$ operator denotes enlarged double inner product of tensors or dyadics ($\bar{\bar{a}} \otimes \bar{\bar{b}} = a_{ij} b_{ij}$). For multi-component systems, where we are interested only in the net atomic (mass) transport regardless to the contributions of individual chemical species, the first generalized-mobility given above may not be easily connected to any combination of the intrinsic surface diffusivities of individual chemical species in the interfacial layer or in the bulk phase. However, for one component system having minor amount of doping elements or impurities, the situation is rather simple where one can easily identify the existence of the following relationship between generalized mobility and the surface self-diffusivity of host matter denoted by $\tilde{D}_\sigma$,

$$\hat{\mathrm{M}}_\sigma = \frac{\mathrm{M}_\sigma}{kT} = \frac{\tilde{D}_\sigma}{kT}\frac{h_\sigma}{\Omega_\sigma} = \frac{\tilde{D}_\sigma}{kT}\Gamma_\sigma, \tag{3.4.13}$$

Hence, for the future discussions, the following compact form will be used, which is more suitable to take other driving forces such as the electromigration and the stress assisted drift motion of surface atoms into considerations:

$$J_\sigma = \hat{\mathrm{M}}_\sigma \frac{\partial}{\partial \ell}\left[\Omega_\sigma\left(\breve{g}_{vb} + g_\sigma \kappa\right) - \langle eZ\rangle \vartheta + \Omega_\sigma \left\langle \bar{\bar{\lambda}} \right\rangle \otimes \bar{\bar{\sigma}}\right] \tag{3.4.14}$$

where $\hat{\mathrm{M}}_\sigma$ may be called surface atomic mobility, and it has the dimension given by [1/erg.sec]. The generalized mobility M_{vb} [cm^2/sec] associated with the incoming bulk diffusion flux is related to the transformation rate of chemical species from bulk phase to the interfacial layer or vice versa over the activation energy barrier denoted by ΔG^*_{vb}. Hence, it can be defined according to the transition rate theory of chemical kinetics advocated by Eyring (Yeremin, 1979), as: $\mathrm{M}_{vb} = \left(\frac{kT}{h}\right)\exp\left(-\frac{\Delta G^*_{vb}}{kT}\right)$, where h is Planck's constant. In our future formula we will use rather renormalized mobility, which may be defined by $\hat{\mathrm{M}}_{vb} = \mathrm{M}_{vb}/kT$, which has the following dimension [cm^2/erg.sec].

CHAPTER 4

MATHEMATICAL MODEL & NUMERICAL PROCEDURES

4.1. Introduction

As entirely discussed in the literature survey, up to the novel studies carried out by Ogurtani (2000), Ogurtani and Oren (2001, 2003), all the theoretical studies related to the interfaces and surfaces, which are reported and cited, are strictly relying on the classical thermodynamics as a general tool for the macroscopic description of physico-chemical processes with some obscure modifications in the concept and usage of chemical potentials, and the free energies especially in the presence of externally imposed force fields without considering their original strictly mathematical definitions by Gibbs (1948). The more serious limitation of these approaches lies in the fact that the methods are based on reversible processes and true equilibrium states.

However, the groove formation at the sites of grain boundary intersections with a free surface starts at a point we can call the ‘groove root’, which is nothing but a triple junction itself. Triple junction motion is a completely natural (irreversible) process, and although Mullins’ theory of thermal grooving is successful in describing profile changes, we believe that this special point should be treated as it is, not with the formulations based on reversible processes. The theory given in Chapter 3 enables this special treatment, and showed to be successful by former studies of Ogurtani and Oren (2001, 2002, 2003).

4.2. Mathematical Modeling

In the present model, a constant electric field E_o is imposed far away from the groove surface, which generates an electrical field denoted by E, having zero normal components at the free surfaces. Fig. 4.2.1 shows the schematic representation of the model, which is under discussion.

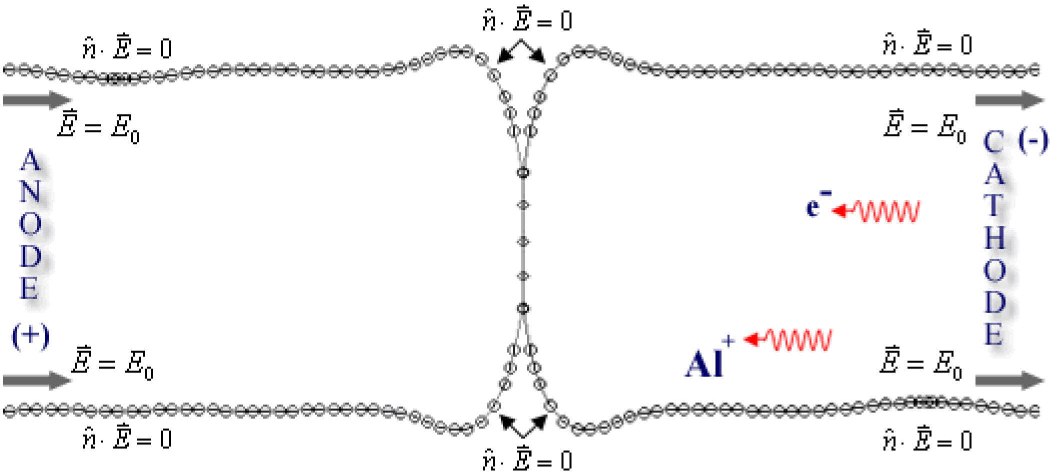

Figure 4.2.1: The schematic representation of the problem.

Following a series of normalization and scaling procedures, final form of the boundary value problem whose theoretical considerations are fully discussed in Chapter 3 is given in sections 4.2.2 and 4.2.3.

4.2.1. Normalization & Scaling

In Chapter 3 equations describing the phenomenon are obtained without the use of simplifications or normalization procedures. However we perform the actual calculations using normalized units to make the algorithms more efficient, to eliminate any necessity for the knowledge of the specific material properties, and to avoid numerical overflow and underflow. In the following formulas the bars over the symbols indicates the normalized and scaled quantities.

The curvilinear coordinate along the curved surface formed by grooving (arc length), ℓ, the interconnect with w, the local curvature, κ, that represents the capillary effect, and the system time, t, are normalized with respect to selected scales (ℓ_o, τ_o) as shown below:

$$\bar{\ell} = \ell / \ell_o, \qquad \bar{w}_o = w_o / \ell_o, \qquad \bar{\kappa} = \kappa\, \ell_o \qquad \text{and} \qquad \bar{t} = t / \tau_o, \tag{4.2.1.1}$$

The volumetric Gibbs free energy difference between the gaseous phase and the bulk phase can be normalized by using the specific Gibbs free energy of the interfacial layer, denoted by g_σ,

$$\bar{g}_{vb} = \frac{\breve{g}_{vb}\ell_o}{g_\sigma} \tag{4.2.1.2}$$

The electrostatic potential generated at the void surface may be normalized with respect to the remote applied electric field denoted by E_0 and it is given by

$$\bar{\vartheta} = \frac{\vartheta}{E_o \ell_o} \tag{4.2.1.3}$$

The relative importance of electromigration with respect to capillary forces can be easily represented by a single variable χ that may be called as the *electron wind intensity*.

$$\chi = \frac{e\left|\hat{Z}\right| E_o \ell_o^2}{\Omega_\sigma g_\sigma} \tag{4.2.1.4}$$

where $e\hat{Z}$ is the effective charge in multi-component systems.

And similarly the generalized mobility $\hat{\mathrm{M}}_{vb}$ associated with the interfacial displacement reaction taking place during the surface growth process, $\hat{\mathrm{M}}^{long}$ and

$\hat{\mathrm{M}}^{trans}$, which correspond to the longitudinal and transverse triple junction mobilities, are normalized with respect to the mobility of the surface diffusion denoted by $\hat{\mathrm{M}}_{\sigma}$,

$$\bar{\mathrm{M}}_{vb} = \frac{\hat{\mathrm{M}}_{vb} w_o^2}{\hat{\mathrm{M}}_{\sigma}}, \qquad \bar{\mathrm{M}}^{long} = \frac{\hat{\mathrm{M}}^{long}}{\hat{\mathrm{M}}_{\sigma}} \quad \text{and} \quad \bar{\mathrm{M}}^{trans} = \frac{\hat{\mathrm{M}}^{trans}}{\hat{\mathrm{M}}_{\sigma}} \qquad (4.2.1.5)$$

where,

$$\hat{\mathrm{M}}^{long} = \frac{\Re^{long}}{kT} \frac{h_g}{\Omega_g}, \qquad \hat{\mathrm{M}}^{trans} = \frac{\Re^{trans}}{kT} \frac{h_\sigma}{\Omega_\sigma} \quad \text{and} \quad \hat{\mathrm{M}}_{\sigma} = \frac{D_\sigma^o}{kT} \frac{h_\sigma}{\Omega_\sigma} \qquad (4.2.1.6)$$

In above description we have tried to scale the time and space variables $\{t, \ell\}$ in a following fashion; first of all, $\hat{\mathrm{M}}_{\sigma}$, an atomic mobility associated with mass flow at the surface layer, is defined by the relationship given in the previous section, and then a new time scale is introduced by $\tau_o = \ell_o^4 / \left(\Omega_\sigma^2 \hat{\mathrm{M}}_\sigma g_\sigma\right)$, where ℓ_o is the arbitrary length scale, which is for the present simulation studies chosen as $\ell_o = w_o / 3$, where w_o is the halve width of the interconnect specimen. The size of the scaling length is only important for the stress calculations using BEM technique to obtain proper convergency, which utilizes the Kelvin's solution for the elastostatic problems. Ω_σ is the atomic volume in the surface layer, $\tilde{D}_\sigma \delta_\sigma$ is the thickness of the surface layer times its diffusivity, k is the Boltzmann's constant, T is the absolute temperature and ϑ is the electrostatic potential generated at the surface due to the remote applied electric field denoted by E_o. The surface specific Gibbs free energy, g_σ, plays very important role in above definitions. $\bar{g}_{vb}$ ($\bar{g}_{vb}$<0 evaporation) is the volumetric Gibbs free energy difference (the Gibbs free energy of transformation) between the realistic void and the bulk phase, and it is normalized with respect to the specific surface Gibbs free energy.

Using these, the evolution kinematics of the surfaces or the interfacial layers (simply connected domains) may be described by the following well-posed moving boundary value problem in 2D space, for the ordinary points and TJ singularities, in terms of normalized and scaled parameters and variables, assuming that the surface drift-diffusion and the specific Gibbs free energy of the interfacial layer are anisotropic and isotropic (for the time being), respectively.

4.2.2. Normal Displacement Velocity of the Ordinary Points

After these normalizations, the normal displacement velocity of an ordinary point at the surface layer, may be given by the following fourth order partial differential (nonlinear) equation in curvilinear coordinate system,

$$\bar{v}_{ord} = \frac{\partial}{\partial \bar{\ell}} \left[D''(\theta,\phi) \frac{\partial}{\partial \bar{\ell}} \left(\Delta \bar{g}_{vb} + \chi \bar{\vartheta} + \bar{\kappa} + \psi \bar{\Phi} \right) \right] - \bar{\mathrm{M}}_{vb} \left(\Delta \bar{g}_{vb} + \bar{\kappa} \right) \tag{4.2.2.1}$$

where, the angular dependent post factor $D''(\vartheta,\theta)$ denotes the anisotropic surface diffusivity.

Assumption of isotropic specific surface Gibbs free energy g_{σ} and the Gibbs free energy of transformation is homogeneous in space ($\nabla_2 \left(\Delta \bar{g}_{vb} \right) = 0$) brings further simplification to Eq. (4.2.2.1) which takes into account that one may have condensation ($\Delta \bar{g}_{vb} > 0$) or/and evaporation ($\Delta \bar{g}_{vb} < 0$):

$$\bar{v}_{ord} = \frac{\partial}{\partial \bar{\ell}} \left[D''(\theta,\phi) \frac{\partial}{\partial \bar{\ell}} \left(\chi \bar{\vartheta} + \bar{\kappa} + \psi \bar{\Phi} \right) \right] - \bar{\mathrm{M}}_{vb} \left(\Delta \bar{g}_{vb} + \bar{\kappa} \right) \tag{4.2.2.2}$$

4.2.3. Triple Junction Motion

Similarly, the triple junction drift velocity in the direction along the grain boundary can be represented by,

$$\bar{v}_g^{long} = \bar{\mathrm{M}}^{long} \frac{\bar{\Omega}_g \bar{d}_a}{2\bar{\Omega}_\sigma^2 \bar{h}_g} \left[2\lambda - \left(\cos\theta^+ + \cos\theta^- \right) \right] \qquad (4.2.3.1)$$

In our formulation of the problem, we have adapted the convention such as that the positive direction of the motion is always towards the bulk material whether one deals with inner voids or outer surfaces or interfaces. The following boundary conditions at the triple junction in terms of right and left side fluxes may be written;

$$\bar{J}_o^{\mp} = \mp \bar{\mathrm{M}}^{long} \frac{\bar{d}_a}{2\bar{\Omega}_\sigma^2} \left(\lambda - \cos\theta^{\mp} \right) \mp \bar{J}_g / 2 + \bar{J}_\vartheta + \bar{\mathrm{M}}^{trans} \frac{\bar{d}_a}{\bar{\Omega}_\sigma^2} \left(\sin\theta^+ - \sin\theta^- \right) \qquad (4.2.3.2)$$

where $\bar{\mathrm{M}}_{gb}$ is the grain boundary drift diffusion mobility $\hat{n}_g$ is the normal vector along the grain boundary direction.

$\bar{J}_g$ denote the normalized atomic fluxes associated with grain boundary mass flow due to some driving force such as thermal stress field inhomogeneities, and/or the drift-diffusion due to electromigration, which is given by the expression

$$\bar{J}_g = -\frac{\bar{\mathrm{M}}_{gb}}{\bar{\Omega}_g} \chi (\hat{n}_g \cdot grad\,\bar{\vartheta}) \qquad (4.2.3.3)$$

$\bar{J}_\vartheta$ is the usual contribution due to electromigration forces acting on the both branches of the void at the triple junction. The electrostatic potential exhibits well known discontinuity at the triple junction (at edges and corners, etc.). On the contrary to this behavior, the tangential component of the electric field intensity vector along the interfacial layers or surfaces is continuous everywhere including the triple junction singularity. In the present problem, the positive direction of the flux is chosen as the clock-wise direction around the interconnect body starting from the upper left edge (anode side).

A careful examination of Eq. (4.2.3.1) and Eq. (4.2.3.2) shows immediately that there is no conservation of fluxes at the triple junction in ordinary sense. This is due to fact during the displacement of the triple junction there is a phase transformation taking place (positive entropy production), which is precisely accounted by Eq. (4.2.3.1). If one combines incoming $\bar{J}_\sigma^-$ and outgoing $\bar{J}_\sigma^+$ conjugated fluxes at the triple junction using Eq. (4.2.3.2), and recalling that the clockwise direction is chosen as to represent the positive direction of the fluxes in our work, then one arives the following universal connection in the presence of Eq. (4.2.3.1), namely the conservation of chemical species including the phase transformation at the triple junction:

$$\bar{J}_\sigma^- - \bar{J}_\sigma^+ + \bar{J}_g \equiv \frac{\bar{v}_g^{long}\,\bar{h}_g}{\bar{\Omega}_g} \qquad (4.2.3.4)$$

Where the term on right side represents the rate of material rejection or gain by the grain boundary during the displacement of the triple junction along the grain boundary. Similarly, the third term on the left side $\bar{J}_g$ is the incoming material flux from the grain boundary to triple junction.

However, in the present investigation, it is assumed that even in the case of tilt boundary, there is no grain boundary diffusion taking place, $\bar{M}_{gb} = 0$, though there is a non-vanishing electric field intensity projection along the GB, when $\chi \neq 0$. So that the groove tip fluxes can be given by the following simplified form of Eq. (4.2.3.2):

$$\bar{J}_o^{\mp} = \mp \bar{\mathrm{M}}^{long}\,\frac{\bar{d}_a}{2\bar{\Omega}_\sigma^2}\left(\lambda - \cos\theta^{\mp}\right) + \bar{\mathrm{M}}^{trans}\,\frac{\bar{d}_a}{\bar{\Omega}_\sigma^2}\left(\sin\theta^+ - \sin\theta^-\right). \qquad (4.2.3.5)$$

4.2.4. Boundary Conditions

For a disconnected interfacial layer (finite or infinite) such as one or two-grain sector of interconnect, the additional boundary conditions should be set at the end points of the metallic line, where the direct contact with electrodes through an interface does exist or not. In our computer simulation studies, we have considered three types of boundary conditions (excluding the periodic BC) for a finite system, depending upon the experimental conditions in the laboratory testing and the interaction of the test piece with its immediate surroundings.

4.2.4.1.The Reflecting Boundary Condition (R-BC):

This boundary condition is also known as insulating BC, which does not allow any material flow or leakage due to drift-diffusion caused by chemical, capillary and electromigration forces at the anode and/or cathode edges. The net flux at the edge may written as in the normalized and scaled time and space domain (NSTS) :

$$\bar{J}_{\sigma}^{edge} = D''(\theta,\phi)\frac{\partial}{\partial\bar{\ell}}\left(\Delta\bar{g}_{vb} + \chi\bar{\vartheta} + \bar{\kappa}\right) \equiv 0 \qquad (4.2.4.1)$$

In the computation of the electrostatic potential at the interface between substrate and the interconnect, and also at the free surface layer, which is exposed to air or just detached from the cathode electrode, we will set the electromigration boundary conditions such as that the normal component of the electric field intensity vector is identically equal to zero. At the cathode and anode pads, we will assume that an adaptive external potential difference is applied in order to maintain a constant current flow during the evolution period, regardless the variation of the electrode contact areas there.

4.2.4.2.The Interactive-Barrier Boundary Condition (IB-BC):

This boundary condition is taken into account where the capillary reaction (wetting) is taking place at the contact layer between electrode and the interconnect material. This boundary condition is very similar to the grain boundary surface interaction problem (one-sided GB) with one modification, namely the interfacial layer between electrode pad and the edge of the interconnect line stays rigid and impermeable to drift-diffusion flux. However, the contact area will diminish or increase due time, as it will be demonstrated later in the following chapter by computer simulations. This boundary condition is especially very suitable for the anode side of the interconnect structures, which results a hillock formation at that edge with proper topology, rather then the ordinary up-hill mass accumulation resulted from the application of the reflection BC. It can be also used for the cathode edge, up to the point where the detachment of the interconnect from the electrode pad occurs, which normally indicates catastrophic cathode failure. As a special application of Ogurtani's theory, one can show that the displacement velocity of the one-sided triple junction at the electrode end may be written in NSTS domain as:

$$\bar{v}_e = \bar{\mathrm{M}}^e \frac{\bar{\Omega}_e \bar{d}_a}{2\bar{\Omega}_\sigma^2 \bar{h}_e}\left[2\lambda^e - \left(\cos\theta^e + \frac{g_e}{g_\sigma}\right)\right] \tag{4.2.4.2}$$

One can also write down the following expression for the incoming flux to the interconnect surface from the interface junction at the electrode pad,

$$\bar{J}_o^s = \bar{\mathrm{M}}^e \frac{\bar{d}_a}{2\bar{\Omega}_\sigma^2}\left(\lambda_{eb} - \cos\theta^e\right) + \bar{J}_{eb} + \bar{J}_\vartheta^e \tag{4.2.4.3}$$

where $\lambda_{eb} = g_{eb}/2g_\sigma$ is the electrode wetting parameter, and g_e, g_σ are the specific surface Gibbs free energies associated with electrode and the interconnect material, respectively. Similarly, g_{eb} is the interfacial Gibbs free energy between interconnect material and the electrode. $\bar{M}_e$ is the normalized mobility of the one-sided triple junction along the electrode surface. θ_e is dihedral angle at the electrode edge of the interconnect. $\bar{J}_{eb}$ is the flux coming from the electrode-interconnect interface to the junction due to the residual stress inhomogeneities. $\bar{J}_g^e$ is the flux due to drift-diffusion driven by EM at the junction on the interconnect side. Similarly the flux coming from the triple junction towards the exposed area of the electrode to air may be written as:

$$\bar{J}_o^e = -\bar{\mathrm{M}}^e \frac{\bar{d}_a}{2\bar{\Omega}_\sigma^2}\left(\lambda_{eb} - \frac{g_e}{g_\sigma}\right) \tag{4.2.4.4}$$

One can easily see that the combination of Eq. (4.2.4.2), Eq. (4.2.4.3) and Eq. (4.2.4.4) results a relationship similar to Eq. (4.2.4.1), which satisfies the conservation of particles at the electrode junction. As far as the electrostatic boundary conditions are concerned, the situation is exactly equivalent to the case described in type (R-BC).

4.2.4.3.The Free-Moving Boundary Condition (FM-BC):

This BC assumes that there is no direct contact with electrode pads at the cathode and/or anode edges. The whole interconnect test piece like Blech type experimental set-up rests on a substrate (TiN or Mo, W), which has very high specific resistivity compared to the interconnect material (i.e., the aluminum and copper stripes carry most of the current since their sheet resistance (a measure of resistance of very thin doped regions; expressed in ohm/square; commonly used to evaluate outcome of semiconductor doping operations, for Al and Cu $\approx 0.07\Omega/\square$) are much lower than of the TiN ($\approx 10\Omega/\square$)). Since the distribution of the specific conductivity, σ_e in the physical system under consideration is discontinuous: the conductivity inside the conductor material differs by a finite value from that of the surrounding (substrate), one has to use the following relationships for the small aspect ratio according to Averbuch *et. al.*(2001):

$$\nabla_2(\sigma_e . \nabla_2 \vartheta) = 0 \tag{4.2.4.5}$$

The finite difference solution of this electrostatic problem in the prescribed physical system under given boundary conditions is the 'bottleneck' of the numerical simulation. The indirect boundary element method utilizing the constant element approach may be used rather effectively to handle the distribution of the electrostatic potential in the interconnect material even at the triple junction singularity, where the substrate plays the role of a shunt on the the test peace during the cathode evolution. In practice two types of boundary conditions may be considered at the cathode and anode edges. As follows:

i) During the evolution process (cathode drift) of the interconnect test specimen a constant potential difference applied to the electrodes, which are fixed in space at their original positions on the substrate.

ii) By utilizing a constant current source a steady state current flow (the strength of the external electric field is invariant and homogeneous in space) is maintained through the system regardless its overall resistivity and the surface topology and the shape of interconnect specimen. This is the most common experimental situation encountered in practice while applying the accelerated test measurements in the determination of the mean cathode failure time.

The boundary element method (BEM) solution of the first type of boundary value problem (BVP) still requires the complete knowledge of the instantaneous values of the electrostatic potential distribution at the moving cathode and anode ends of the interconnect material. This moving boundary data can be obtained only by solving the complete BVP in the specified composite domain (interconnect plus the substrate). Therefore, one has to supplement some workable analytical solution for the electrostatic potential distribution at the moving cathode end using the symmetry considerations. The exact solution of the electrostatic potential at the moving cathode tip is possible because of the reflection symmetry of the problem with respect to the longitudinal axis of the test specimen facilitates the conversion of two dimensional problem described by Eq. (4.2.4.5) into one dimension.

4.3. Numerical Procedures

We consider an interconnect system composed of two grains and naturally having two triple junctions associated with a grain boundary as illustrated in Fig. 4.3.1.

The interconnect system is considered to be groove free at the beginning and appeared as a collection of nodes as a result of discretization, forming predetermined segment lengths. Present model employs symmetry in the preparation of upper and lower strips of interconnect. This eases control of indices throughout the development of computer code. In some experiments upper and lower strips are notched in order to track changes take place in an ordinary node on a curved surface.

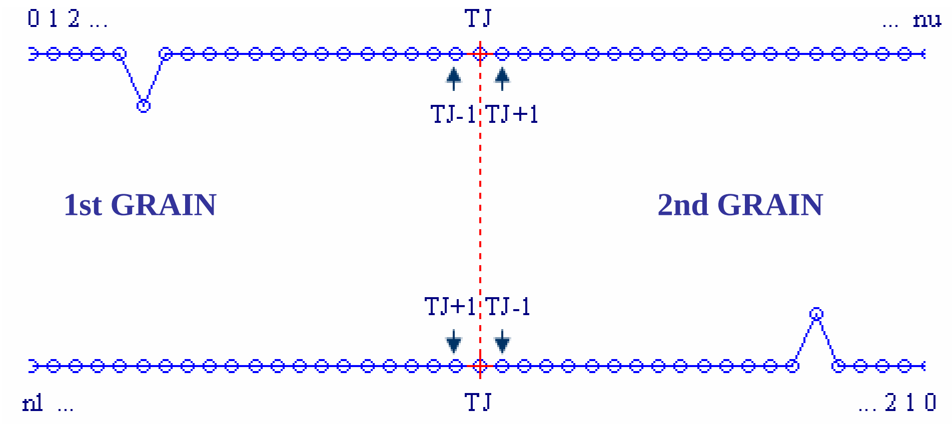

Figure 4.3.1: Schematic representation of the initial system showing ordinary points and triple junctions. ‘*nu*‘ and ‘*nl*‘ are respectively total number of nodes at the upper and lower strips of the interconnect.

In Appendix the C++ code developed is given, whose algorithms are discussed below.

The model is two dimensional; however, node positions are stored in 3x1 matrices in order to make use of vector algebra. Once node, node centroid positions and segment lengths are introduced, turning angles or angle between two successive segments and local boundary normal vectors are calculated by certain algorithms (Appendix). Similarly the node curvatures are calculated by using a discrete geometric relationship in connection with the fundamental definition of radius of curvature and the normal vector applying vector and dot products wherever needed.

The electrostatic potential $\nabla\vartheta(r)$ on system boundaries obey the Laplace equation given by

$$\nabla^2\vartheta(r) = 0 \tag{4.3.1}$$

and subjected to the Neumann boundary conditions,

$$\hat{n}\cdot\nabla\vartheta(r) = \hat{n}\cdot\frac{\partial\vartheta(r)}{\partial r}\hat{r} = 0 \tag{4.3.2}$$

which indicates that the electric field at the boundary along the boundary normal is zero.

Comparing with finite element method (FEM), IBEM requires less number of nodes, less computing time, and stroge but offers higher accuracy and efficiency in analysis, especialy in analysis of thin structures (Beer and Watson, 1992). So we seek a solution to Eq. (4.3.1) preferably by the use of Indirect Boundary Element Method (IBEM).

Numerical integrations required by IBEM is carried out by trapezoidal rule using '*mint'* (Appendix) sub segments, and an electrostatic connection matrix utilizing the element centroids, is obtained. Finally the normal component of the electric field at the centroid positions on the boundary due to uniformly distributed charge is calculated by solving the system of linear equations formed by IBEM.

For the solution of the linear system, Gaussian elimination with back substitution method is performed.

Explicit Euler's method (Mathews, 1992) is used to perform the time integration of Eqs. (4.2.2.2) & (4.2.3.5). The time step is determined from the maximum surface velocity such that the displacement increment is kept constant for all time step increments. This so-called adapted time step auto-control mechanism combined with the self-recovery effect associated with the capillary term guarantees the long time numerical stability and the accuracy of the explicit algorithm even after performing several hundred to several millions steps.

Accuracy and efficiency of the numerical methods require a strict control of number and position of system nodes. For an accurate and efficient study a remeshing technique that guarantees keeping the distance between two successive nodes, i.e. the segment lengths below a critical value in order to keep the accuracy in an acceptable level, and inhibits formation of useless nodes causing loss of efficiency should be employed. This technique is explained by Fig. 4.3.3.

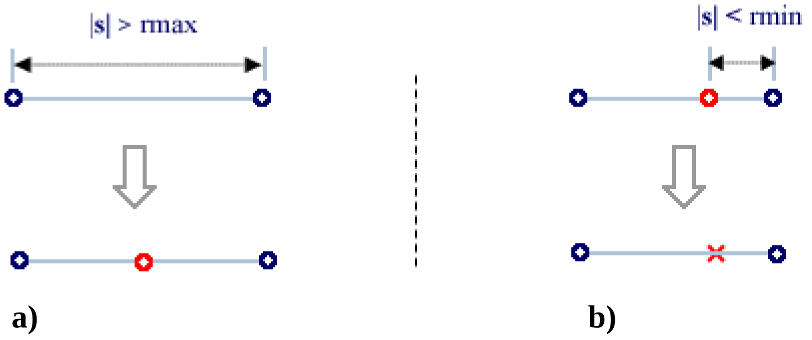

Figure 4.3.3: Remeshing, **a)** the segment length is bigger than the maximum allowable segment length: midpoint is converted to a new node, **b)** the segment length is smaller than the minimum allowable segment length: the node-in-share is discarded and remaining two nodes are combined (after this combination the new

segment is checked whether it is bigger than the maximum allowable segment length or not).

The following figure summarizes the iterative process.

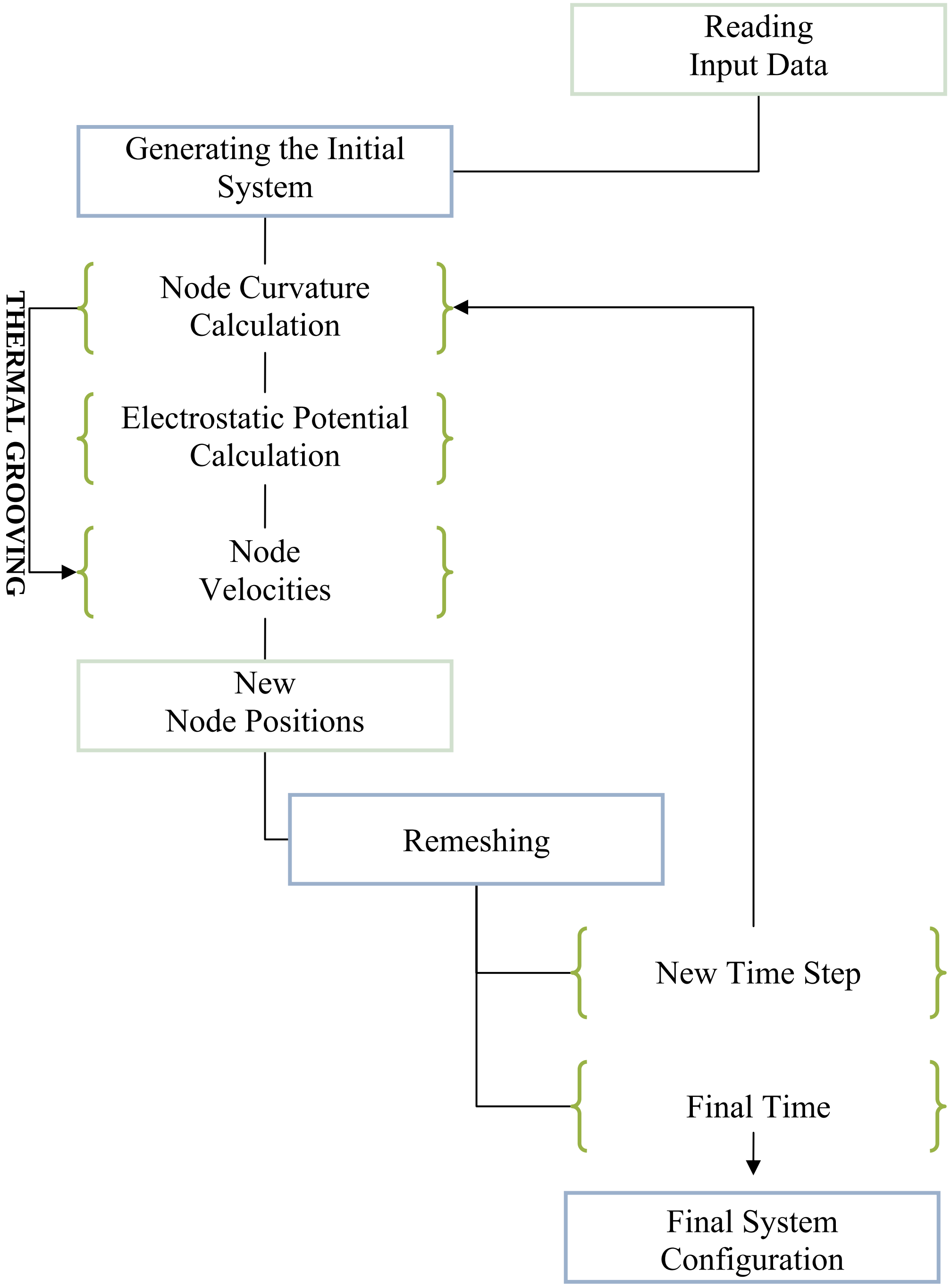

Figure 4.3.4: Program flow chart.

CHAPTER 5

RESULTS & DISCUSSION

5.1. Experimental Setup

Experimental setup considers the metallic (Al-Cu) interconnects in the presence of insulators, vias, and shunts. It is assumed that the sample sandwiched as sketched in Fig. 5.1.1. with a top and bottom high resistance ($TiAl_3$, TiN etc) coatings, which together with the substrate constitute diffusion barrier layers. We also assumed here that only the sidewalls and the edges of the interconnect lines are subjected to the surface drift-diffusion, and they are exposed to environment (air) whose conductivity is neglected in this study.

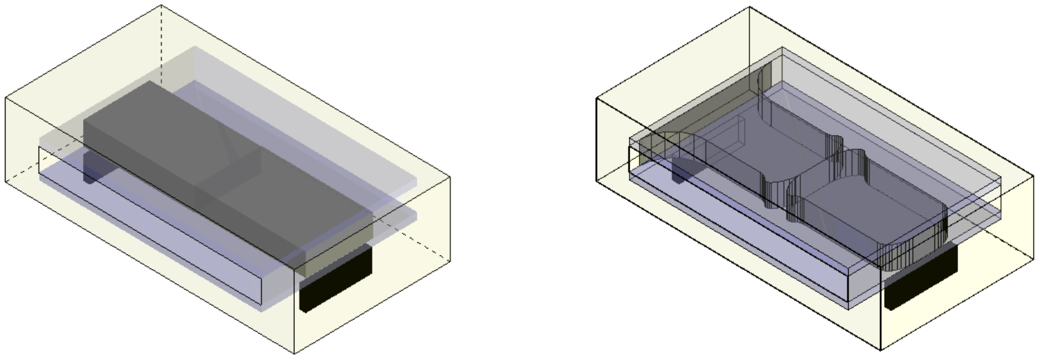

(a) (b)

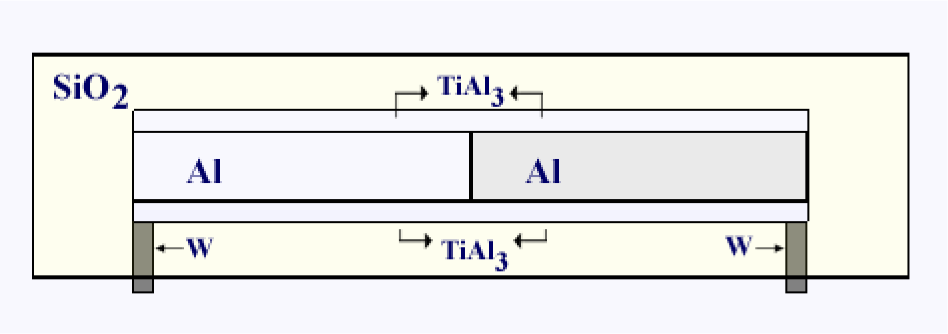

(c)

Figure 5.1.1: Schematic representation of experimental setup:
a) Initial configuration. b) A representative configurational change.
c) Side view.

On a silicon chip interconnects are made of several levels of Al or Cu lines. Silicon dioxide fills the space in between to provide insulation. The whole structure is a metal network embedded in an oxide matrix. The tungsten studs serves as vias to link interconnect lines between different levels. The titanium aluminide (or TiN) shunt the electic current where voids deplete the metallic Al or Cu. Fig. 5.1.2. (Z. Suo, 1998)

a)

b)

Figure 5.1.2: Two and three dimensional interconnect networks in silicon chip.
a) Interconnect with the insulator removed showing more clearly the multi-metal construction. b) A TEM cross-section of a multilevel interconnect structure (Z. Suo *et.al*, 2000).

For the above configuration we consider first the classical Mullins problem with a normal and tilted boundary between the grains, examining positive and negative tilts, without applied electrostatic field.

The effect of the electromigration on the GB grooving kinetics is simulated by applying first a constant voltage difference (CVD) between electrodes (applied electric field intensity, χ is invariant), and assuming that surface drift-diffusion as well as the surface specific Gibbs free energy are isotropic.

The second topic, which is studied thoroughly in this thesis, deals with the cathode drift or voiding under electromigration while hillocks grew at the anode end. In both case studies, the surface drift-diffusion and the specific surface Gibbs free energy are all assumed to be isotropic.

In order to obtain the cathode drift regime, we have further continued our experiments by terminating the CVD condition after 95% reduction in the cathode contact area (or equivalent increase in specimen resistance), and switched on the constant current test (CCT) program by allowing the whole cathode area (the complete width, $2w_0$) is exposed to the original applied electrostatic field intensity denoted by $\vec{E}_o$ (or χ invariant), and then connecting two terminal nodes, which define the remaining part of the cathode contact area (5%), to form a fully-connected cathode contour.

This is the first experimental setup used in this thesis, namely CVD-CCT experiments (mixed electrostatic boundary conditions).

The second setup employs constant current type electrostatic boundary condition for the electromigration forces from beginning to the end.

In these investigations reflecting boundary conditions at the anode, and reflecting or free-moving boundary conditions at the cathode electrodes are utilized, which resulted void formation at the cathode edge and the mass accumulation (hillock) at the anode end of the interconnect material as can be seen from Fig. 5.1.3. As far as the specimen configuration is concerned; the sandwich structure is selected such as that only the lateral surfaces are exposed to the environment (air, etc.), and they also constitute free excess (path) for the electromigration enhanced drift-diffusion of matter (including vacancies).

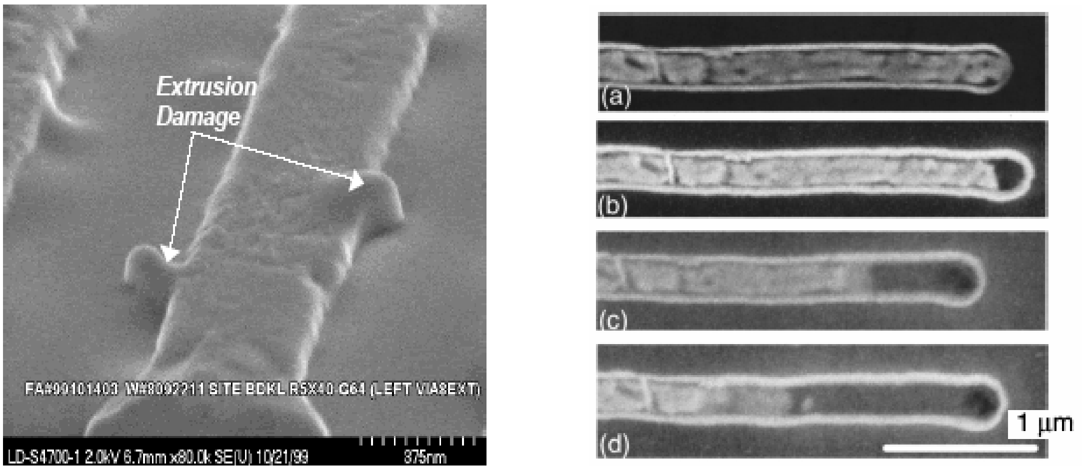

a) b)

Figure 5.1.3: SEM micro-graphs of Cu interconnect lines showing;
a) Mass accumulation at the anode (Ogawa *et.al,* 2000). b) Voiding at the cathode end of a 0.18 μm wide line at (a) 0 h, (b) 9 h, (c) 46 h, (d) 74 h (Liniger *et.al*, 2002).

5.2 Thermal Grooving

5.2.1. Thermal Grooving Without GB Tilt

In Fig. 5.2.1.1, the snapshots from the surface grain boundary interactions for various wetting parameters in the range of $\lambda = 0.1 - 0.8$ shows clearly the effect of the wetting parameter on the morphology as well as on the time dependence of the groove tip displacement.

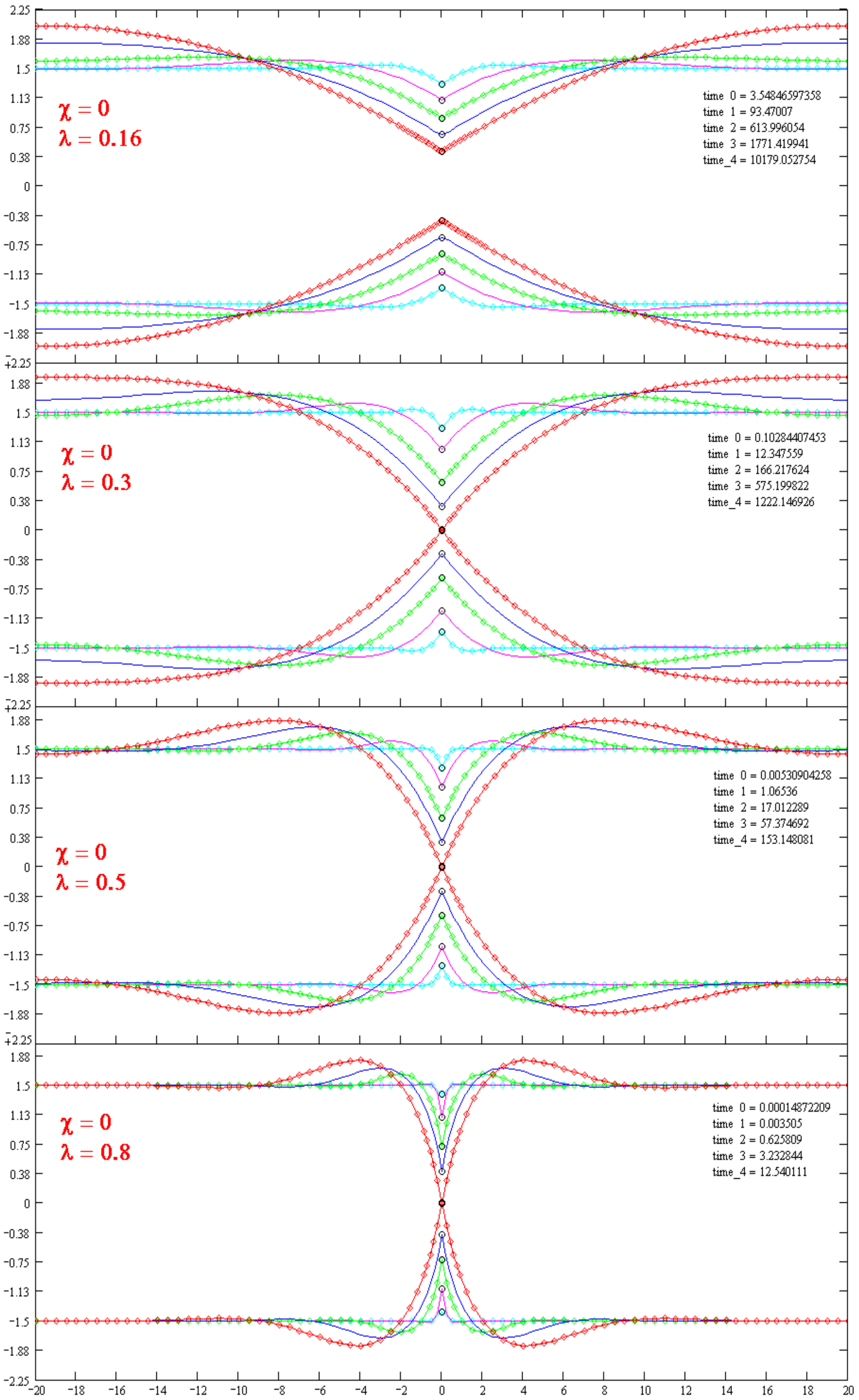

Figure 5.2.1.1: Corresponding profiles for each λ value, no GB tilt.

The evolution behavior of the dihedral angles, $\theta^{\pm}$ and the normalized groove tip depth $\bar{H}_{gb} \equiv H_{gb} / \ell_0$ are presented as a function of normalized time in a semi-logarithmic plots in Fig. 5.2.1.2 and Fig. 5.2.1.3, respectively. In the simulation studies, groove tip displacement is measured with respect to the original surface of the interconnect material, and the positive direction of the motion is chosen towards the bulk region. Fig. 5.2.1.2 shows that the surface - grain boundary system starts to evolve towards the equilibrium configuration having proper dihedral angles dictated by thermostatic theory, which are generally given by and $\theta_{eq}^{\pm} = \arccos(\lambda^{\pm})$ for the left and right sides respectively as soon as they have in close contact with each others.

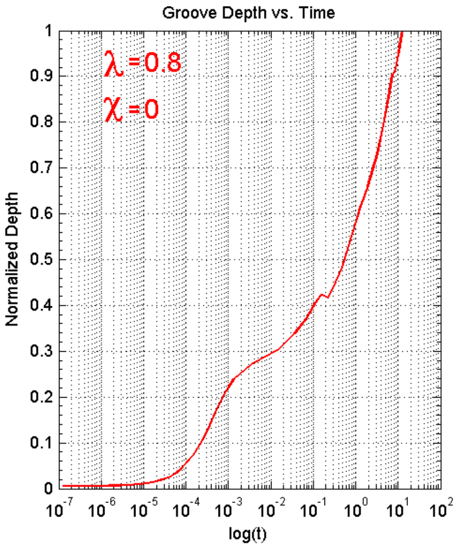

Figure 5.2.1.2: Normalized groove depth vs. logaritmic normalized time for $\lambda = 0.8$ *(nearly complete wetting).*

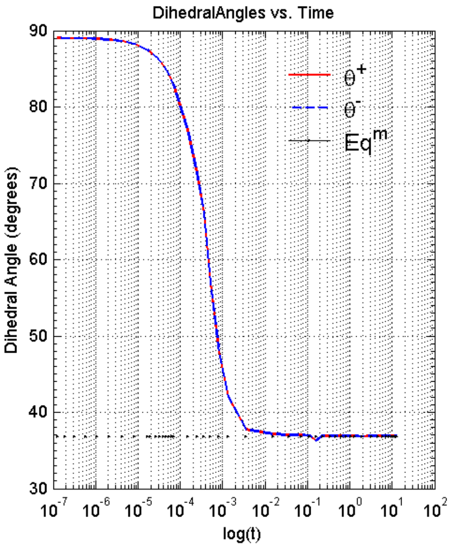

Figure 5.2.1.3: Dihedral angles, $\theta^{\pm}$, vs. logaritmic normalized time for $\lambda = 0.8$.

The rate of this shape evolution process in the transient regime seems to obey the first order reaction kinetics and it is controlled by three independent unit processes, namely the mobility of surface drift-diffusion, and the generalized mobilities associated with longitudinal movement of triple junction and the transverse flow of matter through the junction, respectively. In Fig. 5.2.1.4 the transient and steady state behavior of the normalized groove tip velocity is illustrated in the gross-grain window by filtering out the random fluctuations. The noise, which occurs in the triple junction velocity as well as in the dihedral angles, is due to the global nature of this highly nonlinear problem.

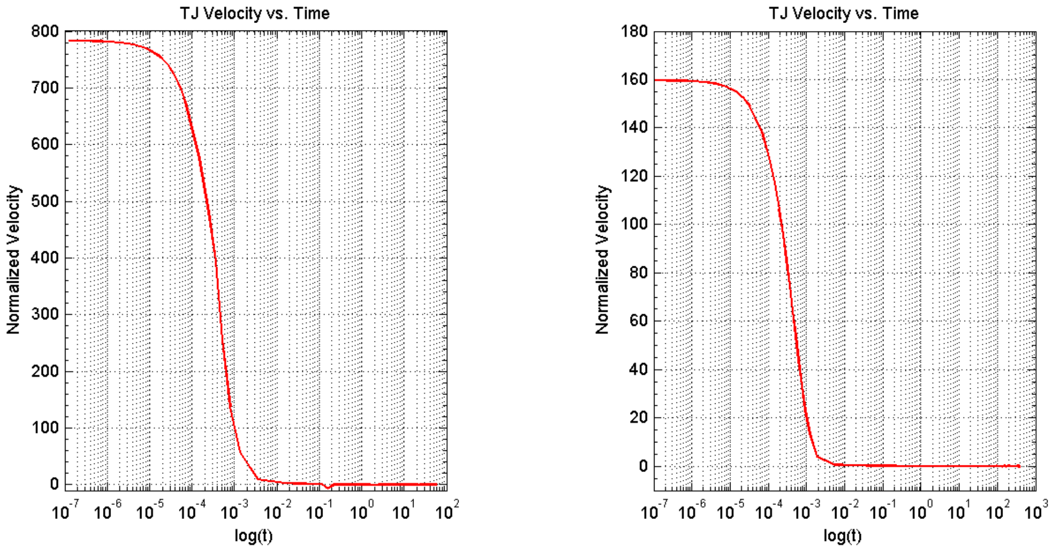

a) **b)**

Figure 5.2.1.4: Normalized triple junction velocity vs. logaritmic normalized time for a) $\lambda = 0.8$ and, b) $\lambda = 0.16$.

The following analytical expression is obtained for the steady state regime by the linear regression analysis, in the normalized and scaled time and space domain:

$$\overline{H}_{gb}(\overline{t},\lambda) = \left[\frac{4\lambda}{5}\left(\overline{t}^{1/4} - \overline{0.01}^{1/4}\right) + \overline{c}(\lambda)\right] \tag{5.2.1.1}$$

$$\overline{V}_{gb}(\overline{t},\lambda) = \frac{\lambda}{5}\overline{t}^{-3/4} \tag{5.2.1.2}$$

Where, $\overline{V}_{gb}(\overline{t},\lambda)$ is the triple junction (TJ) steady state displacement velocity, and $\overline{H}_{gb}(\overline{t},\lambda)$ is the normalized TJ height, and $\overline{c}(\lambda)$ is the modification term and it is closely related to the value of the TJ depth at onset of the steady state regime, which is found to be about $\overline{t}_{onset} \cong 0.01$. According to the data shown in

Fig. 5.2.1.4, the following analytical expression is obtained for this term by a linear regression analysis:

$$\bar{c}(\lambda) = 0.459\lambda^2 + 0.17\lambda + 0.028 \tag{5.2.1.3}$$

The substitution of above connection in Eq. (5.2.1.1) and rearranging the terms results, the following compact formula may be obtained for the groove tip depth in normalized and scaled space:

$$\bar{H}_{gb}^{ST}(\bar{t},\lambda) = \frac{4\lambda}{5}(\bar{t}^{1/4} - \overline{0.01}^{1/4}) + \left[0.459\lambda^2 + 0.17\lambda + 0.028\right] \tag{5.2.1.4}$$

Similarly, the transient plus the steady state regimes may be represented by the following formula, which involves the first order reaction kinetics:

$$\bar{H}_{gb}^{T}(\bar{t},\lambda) = \left[1 - 0.97\exp(-ka\left(\bar{t} - \bar{t}_o\right)\right]\left[\frac{4\lambda}{5}(\bar{t}^{1/4} - \overline{0.01}^{1/4}) + \left[0.459\lambda^2 + 0.17\lambda + 0.028\right]\right] \tag{5.2.1.5}$$

Where ka and $\bar{t}_o$ are system parameters, and found to be 2.5×10^3 and 10^{-7}, respectively.

The validity of these formulas is checked for each experiment carried out for different wetting parameters, Fig. 5.2.1.5 summarizes our results.

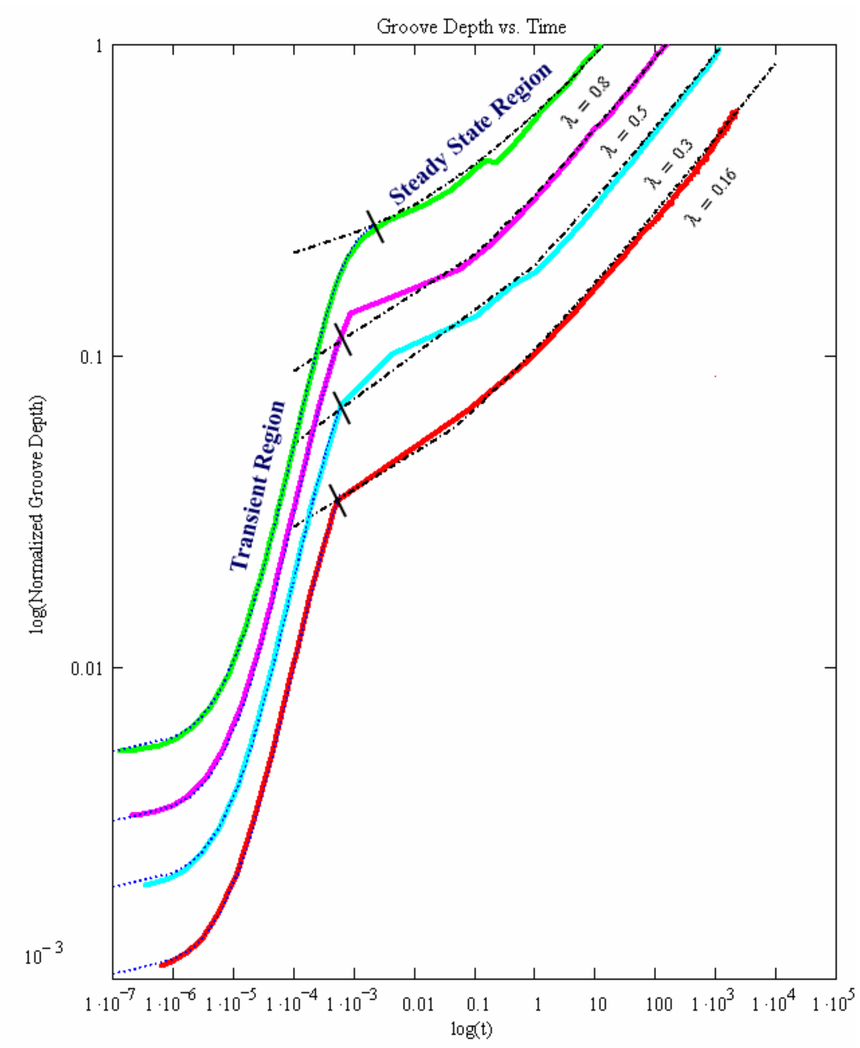

Figure 5.2.1.5: Logarithmic normalized groove depth versus normalized time plot $(\lambda = 0.16 - 0.8)$.

By applying the inverse scaling procedures to our analytical findings denoted by Eq. (5.2.1.4) by utilizing the expressions for the normalized parameters that are given Chapter 4.2.1, one finds the following equation for the grain boundary TJ displacement in terms of the surface diffusivity D_σ, the interfacial layer thickness h_σ, the wetting parameter λ, and the specific surface Gibbs free energy g_σ:

$$H_{gb} = \frac{4\lambda}{5}\left[\frac{D_\sigma h_\sigma \Omega_\sigma g_\sigma}{kT}\right]^{1/4}\cdot\left(t^{1/4} - 0.01^{1/4}\right) + \left[0.459\lambda^2 + 0.17\lambda + 0.028\right] \qquad (5.2.1.6)$$

The first term on the right side of this expression is almost identical to the one obtained by Mullins (1957, Eq.36) for a surface layer of infinite extent, using the small slope approximation in addition to the assumption that the dihedral angles are in equilibrium configuration. The B parameter, which is introduced by Mullins (1957) in his paper for scaling purpose, is exactly equal to ℓ_o^4/τ_o in our representation, which operates on two dimensional finite domain (actually, the general cylindrical surfaces in 3-D). Mullins obtains as a prefactor $a_o = -0.7803$ compared to our value of 4/5 appears in Eq. (5.2.1.6). The sign difference is due to our adapted convention differences as mentioned above. Similarly, renormalization of Eq. (5.2.1.2) results the following expression for the steady state TJ displacement velocity, which may be also obtained from Eq. (5.2.1.6) in a trivial fashion:

$$\bar{V}_{gb}(\bar{t},\lambda) = \frac{\lambda}{5}\left[\frac{\ell_0}{\tau_0}\right]^{-3/4} \equiv \frac{\lambda}{5}\left[\frac{D_\sigma h_\sigma \Omega_\sigma g_\sigma}{kT}\right]^{1/4} t^{-3/4} \qquad (5.2.1.6)$$

Needless to say, this expression is almost identical to the one, which can be deduced from Mullins' formula (1957, Eq.36).

In Chapters 5.2.2 and 5.2.3 results of the experiments carried out for positive and negative grain boundary tilts are given without any further discussion.

5.2.2. 30° of GB Tilt In The Clockwise Direction

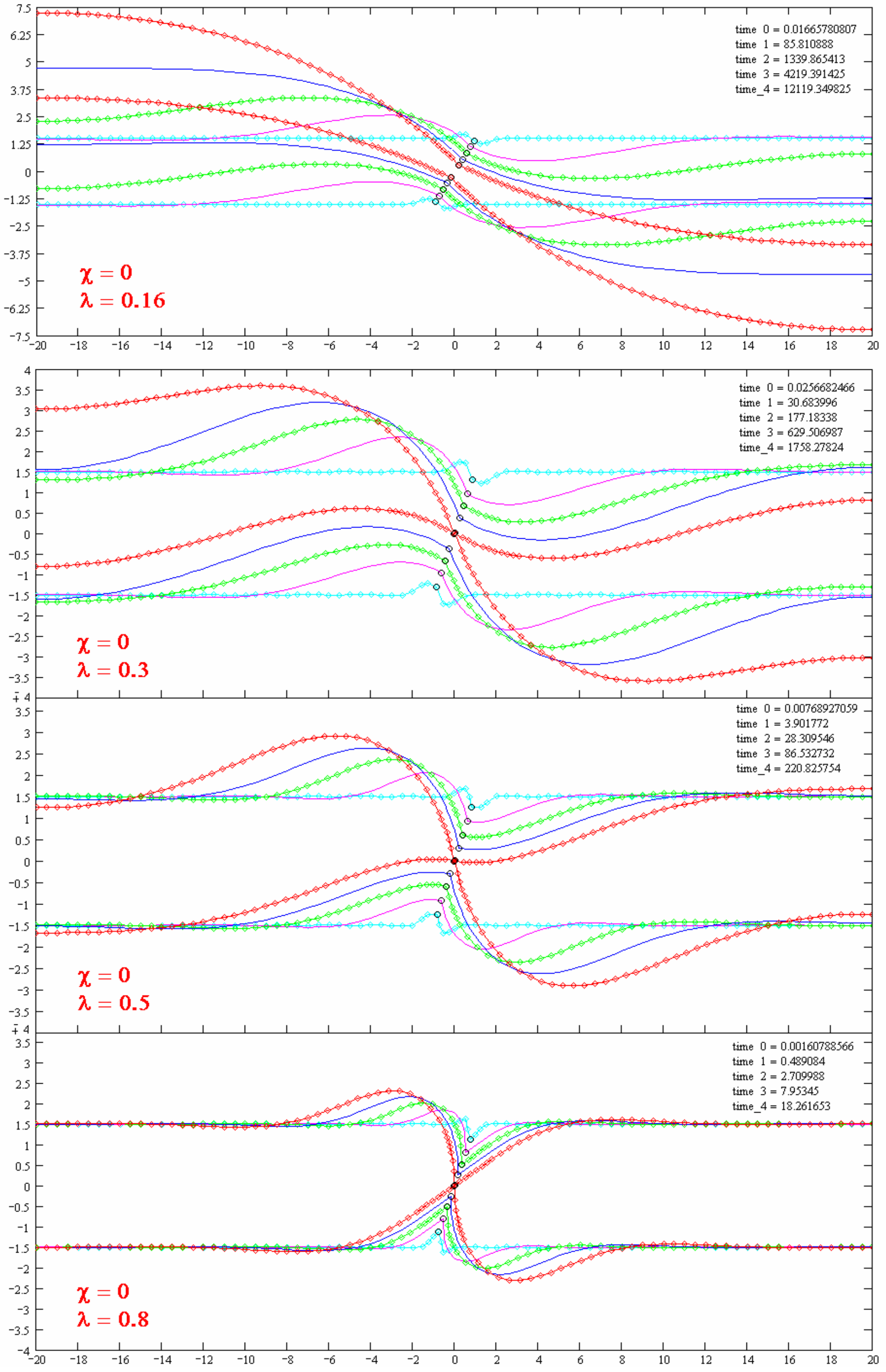

Figure 5.2.2.1: Corresponding profiles for each λ value, 30° of GB tilt in the clockwise direction.

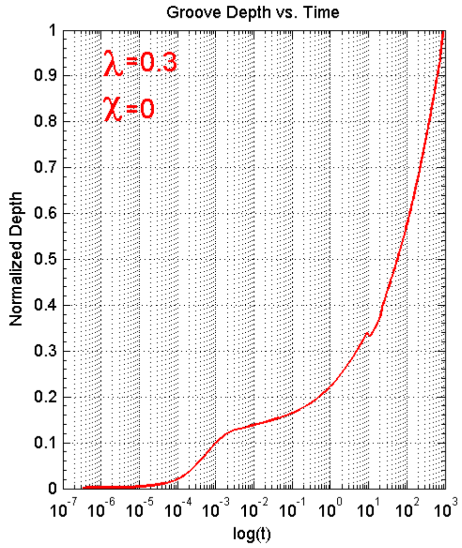

Figure 5.2.1.2: Normalized groove depth vs. logaritmic normalized time for $\lambda = 0.3$.

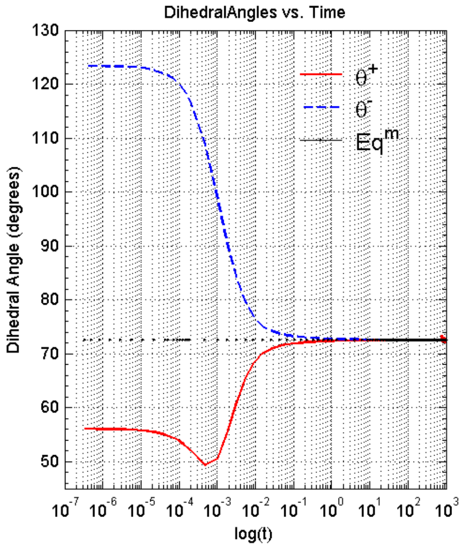

Figure 5.2.1.3: Upper dihedral angles, $\theta^{\pm}$, vs. logaritmic normalized time for $\lambda = 0.3$.

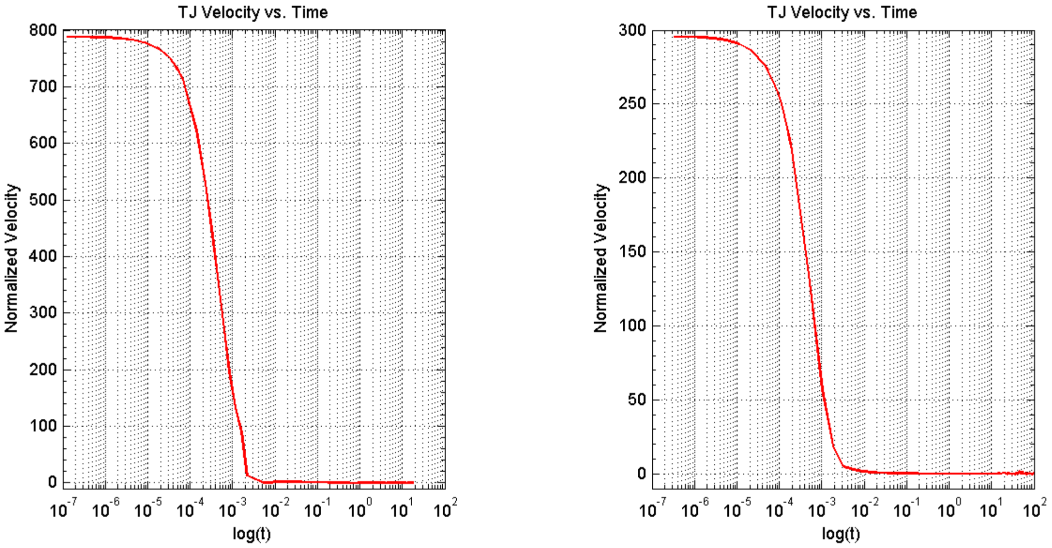

a) **b)**

Figure 5.2.2.4: Normalized triple junction velocity vs. logaritmic normalized time for a) $\lambda = 0.8$ and, b) $\lambda = 0.3$.

5.2.3. 30° of GB Tilt In The Counter Clockwise Direction

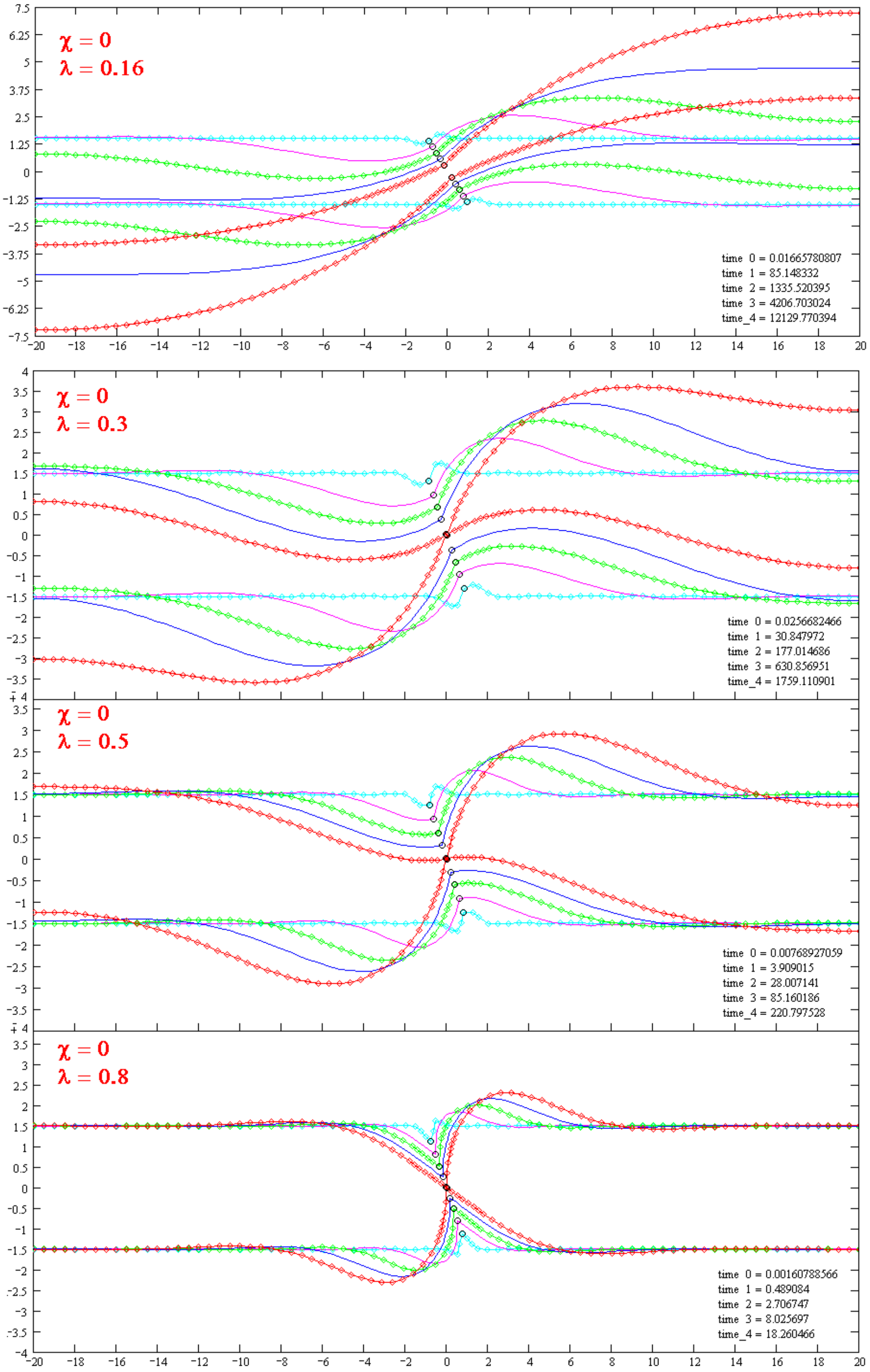

Figure 5.2.3.1: Corresponding profiles for each λ value, 30° of GB tilt in the counter clockwise direction

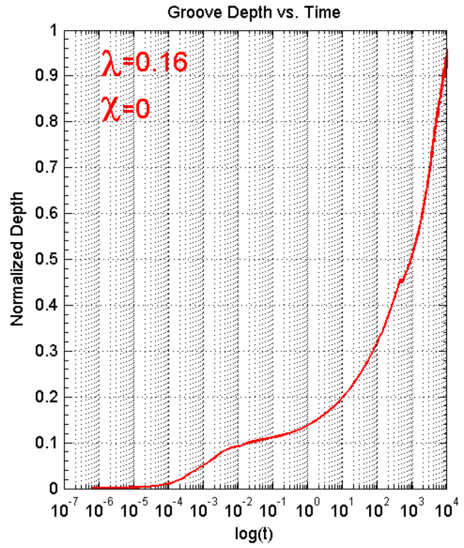

Figure 5.2.3.2: Normalized groove depth vs. logaritmic normalized time for $\lambda = 0.16$.

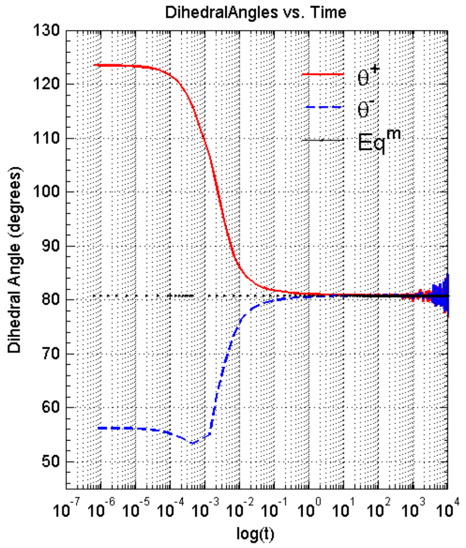

Figure 5.2.3.3: Dihedral angles, $\theta^{\pm}$, vs. logaritmic normalized time for $\lambda = 0.16$.

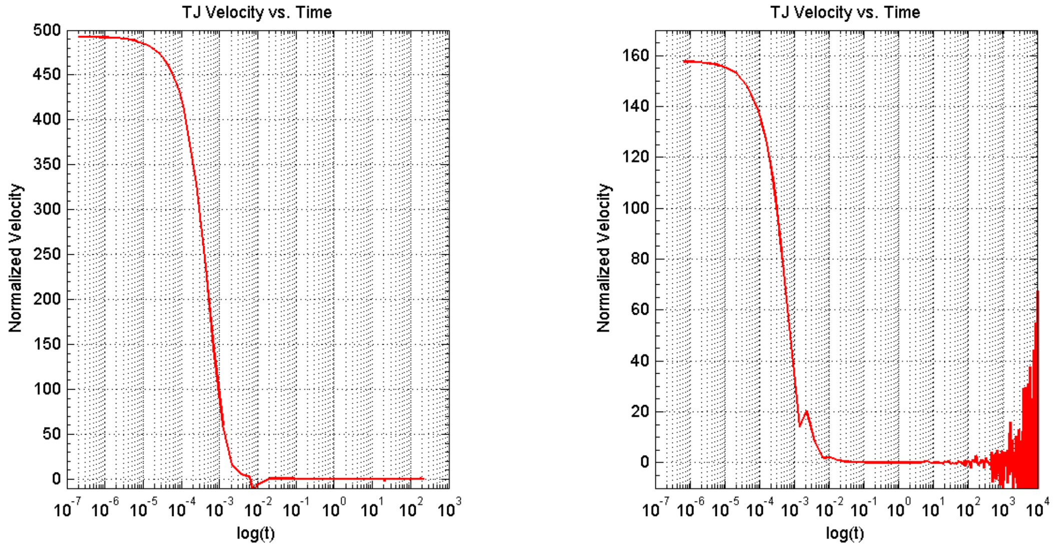

a) **b)**

Figure 5.2.3.4: Normalized triple junction velocity vs. logaritmic normalized time for a) $\lambda = 0.5$ and, b) $\lambda = 0.16$.

5.3. Effect of Electromigration

5.3.1. CVD-CCT Experiments

i. Electromigration Grooving & Cathode Shrinkage

In Fig.5.3.1.1, a typical behavior of the electromigration grooving for a normal GB, and the surface topographical evolution under the action of the capillary and electromigration forces is presented. As far as the surface topology is concerned, there is a pronounce asymmetry in the profile. The windward side of the GB shows an extra mass accumulation compared to the leeward side, which shows almost flat appearance. This asymmetry shows further enhancement upon any increase in the electron wind intensity parameter.

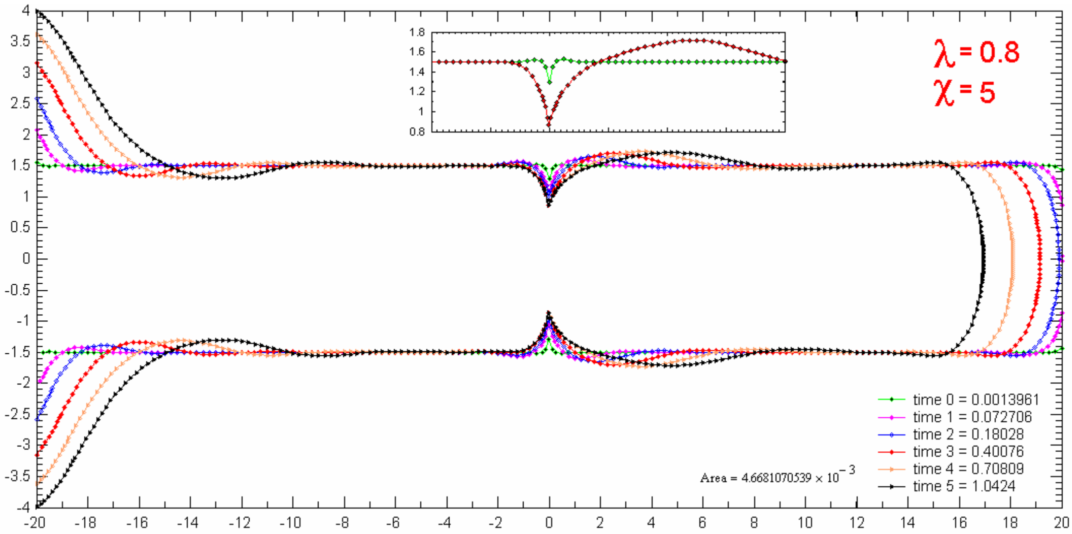

Figure 5.3.1.1: Evolution profile of the test specimen for selected time steps for $\lambda = 0.8$ and $\chi = 5$. Upper window shows the initial and final states of the groove.

Since, we are using the reflecting boundary conditions at edges of the sidewalls, and assuming further that the bulk drift-diffusion is absent, the whole interconnect line, during the electromigration testing will be a conservative close system in terms of the number of particles, as long as one doesn't consider the growth (evaporation or condensation) term in Eq. (4.2.2.2). That means the total volume (area) of the test specimen stays constant regardless its shape. This point is always checked in order to insure that there is no numerical or programming error present during the simulation studies.

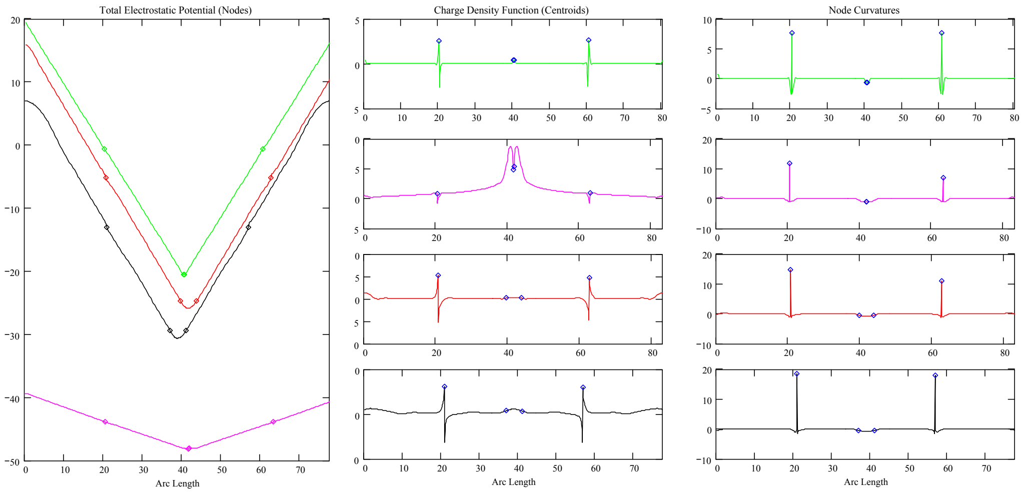

a) b) c)

Figure 5.3.1.2: a) total electrostatic potential, b) charge density function, c) curvature vs. arc length graphs, each following the color series of Figure 5.3.1.1.

As mentioned above, since this first set of simulations is done under *the constant voltage condition* up to 95% reduction in the cathode contact area; there is a steady decrease in the net current flow through the cathode contact area, showing almost inverse exponential type shrinkage with the normalized time. This application manifests itself in the electrostatic potential vs. arclength graphs with a drastic decrease on the onset of cathode detachment in Fig. 5.3.1.2.

In Fig. 5.3.1.3, the normalized groove depth as a function of the scaled time is presented on a semi-logarithmic plot for, $\lambda = 0.8$ and $\chi = 5 - 50$.

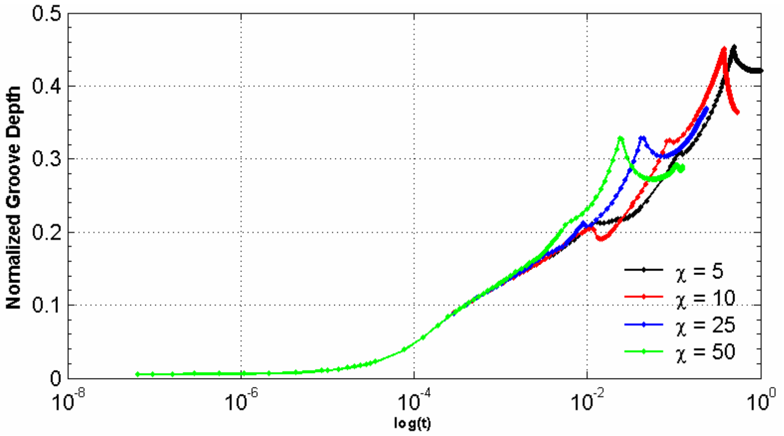

Figure 5.3.1.3: Normalized groove depth vs. normalized time graph for $\lambda = 0.8$ and $\chi = 5 - 50$ interval.

Following figures show the effect of increasing electronwind intensity on the profile evolution for nearly complete wetting case. In these figures first two series (distinguished by the colors of green and magenta) are belong to the case of constant voltage difference testing, and the rest belongs to the profiles after switching to the constant current regime.

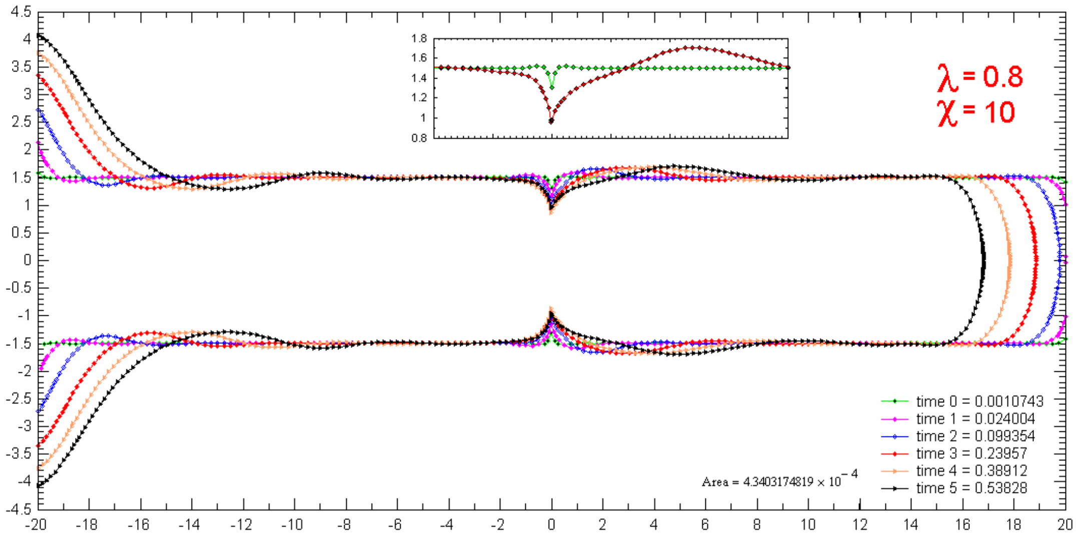

Figure 5.3.1.4: Evolution profile of the test specimen for selected time steps for $\lambda = 0.8$ and $\chi = 10$. Upper window shows the initial and final states of the groove.

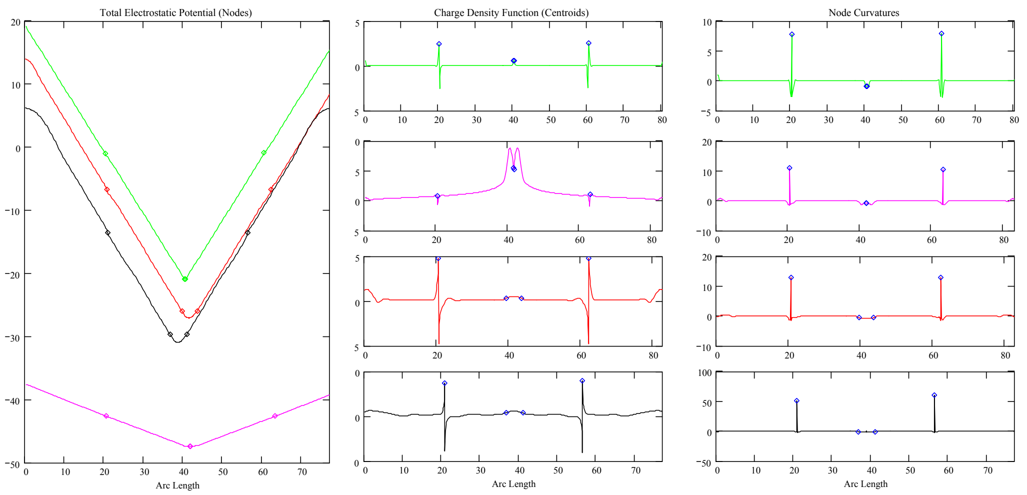

a) b) c)

Figure 5.3.1.5: a) total electrostatic potential, b) charge density function, c) curvature vs. arc length graphs, each following the color series of Fig. 5.3.1.4.

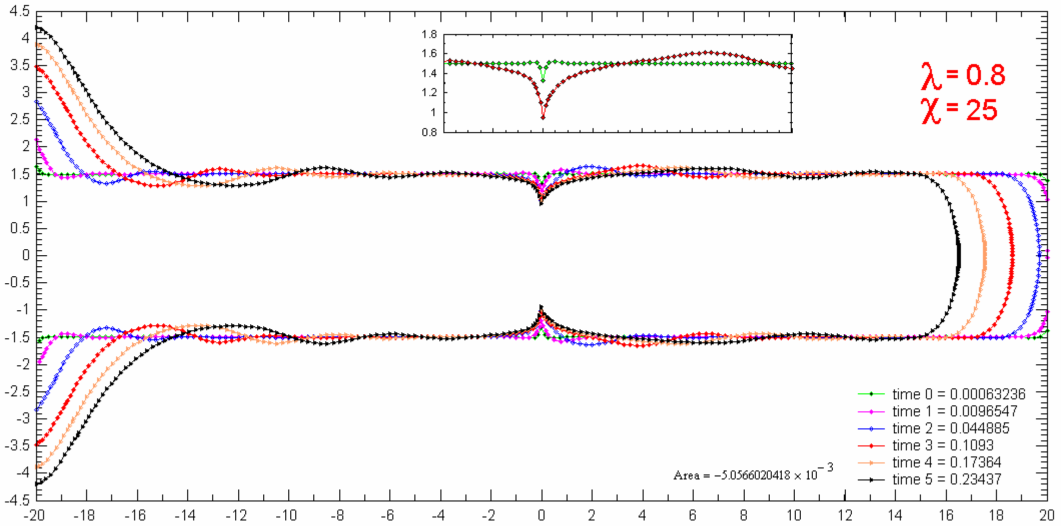

Figure 5.3.1.6: Evolution profile of the test specimen for selected time steps for $\lambda = 0.8$ and $\chi = 25$. Upper window shows the initial and final states of the groove.

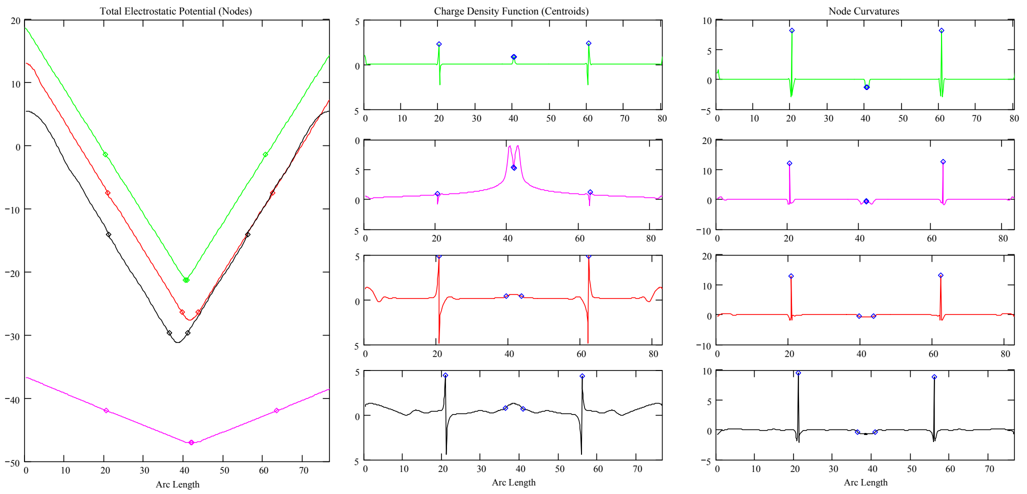

a)　　b)　　c)

Figure 5.3.1.7: a) total electrostatic potential, b) charge density function, c) curvature vs. arc length graphs, each following the color series of Fig. 5.3.1.6.

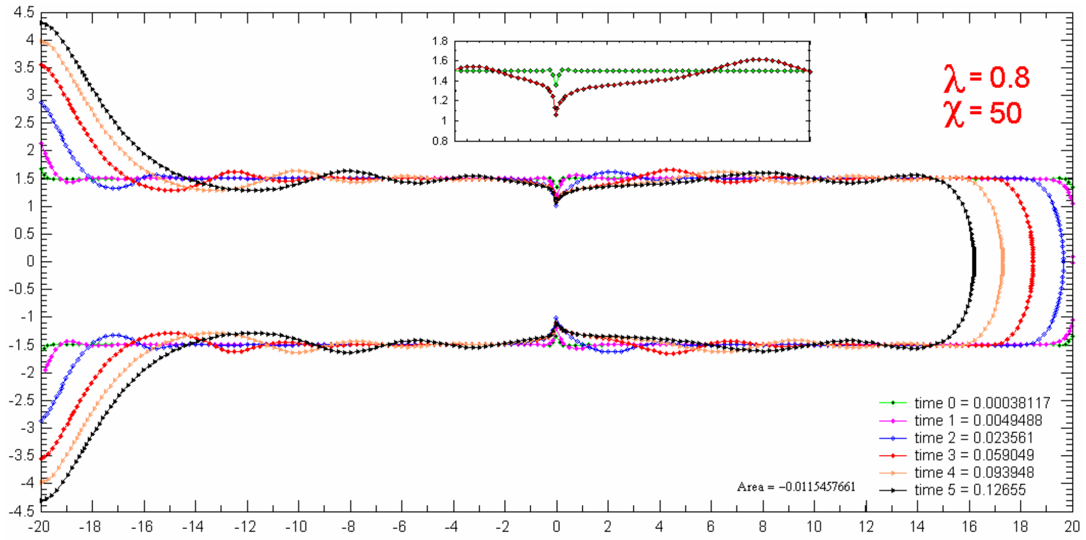

Figure 5.3.1.8: Evolution profile of the test specimen for selected time steps for $\lambda = 0.8$ and $\chi = 50$. Upper window shows the initial and final states of the groove.

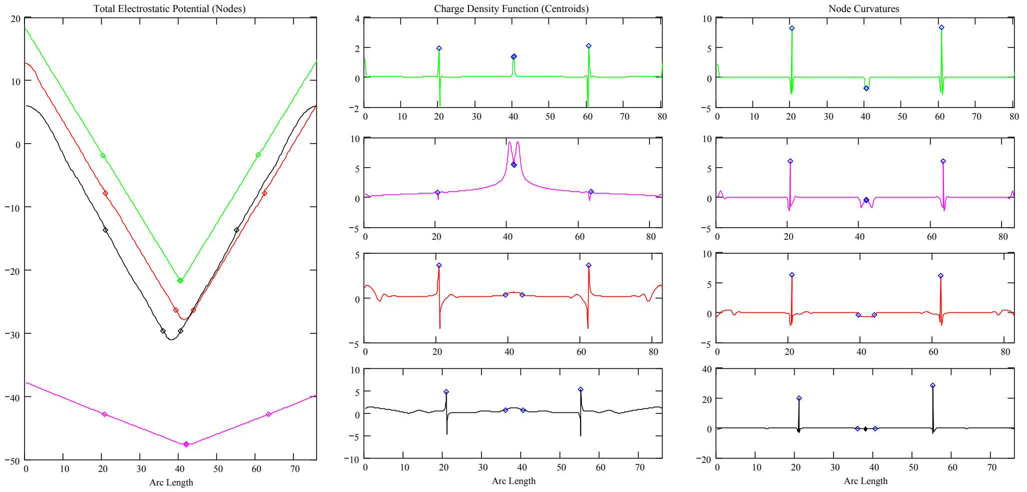

a) b) c)

Figure 5.3.1.9: a) total electrostatic potential, b) charge density function, c) curvature vs. arc length graphs, each following the color series of Fig. 5.3.1.8.

The shrinkage in the cathode area means that the net resistance of the interconnect during the constant voltage differential testing is also increases exponentially with time, as demonstrated by a semi-logarithmic plot in Fig. 5.3.1.10. One may obtain the following analytical connection for the cathode contact area shrinkage versus normalized time using the nonlinear regression procedure at two different regimes:

$$\bar{A}^{CVD}(\bar{t},\chi) \cong \left\{ \begin{array}{ll} 3\left(1-4.5\chi\bar{t}\right) & \text{if } \chi \geq 1 \\ & \\ 3\left(1-8\chi\bar{t}\right) & \text{if } \chi \leq 0.1 \end{array} \right\} \qquad (5.3.1.1)$$

If we assume that the solder joint has failed when the degradation reaches some critical value (e.g. it is 5% drop in electrical resistance of solder joint in the US microelectronic industry) of the fractional cathode area reduction, the time required to reach the failure can be easily obtained from Eq. (5.3.1.1). One may easily write the following expression for the fractional resistance variation using the well known inverse relationship between the resistance and the cathode cross section:

$$f \equiv \frac{\delta R}{R} \equiv -\frac{\delta A}{A} = \frac{\alpha\chi\bar{t}}{1-\alpha\chi\bar{t}}$$

Where $f = 0.05$, $(\%5)$ is the fractional change in the resistance due to the cathode shrinkage because of voiding. $\alpha \cong 4$ for $\chi \geq 1$ and $\alpha \cong 8$ *for* $\chi \leq 0.1$ as stated above.

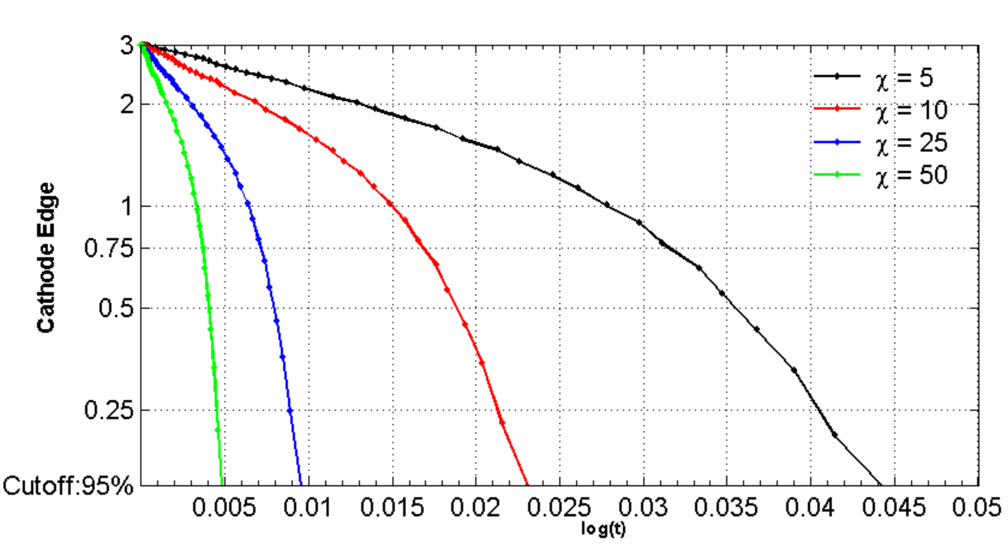

Figure 5.3.1.10: Semilogaritmic cathode contact area shrinkage versus normalized time.

The time dependent normalized and renormalized resistance $R(t)/R_o$ of the sample may be obtained by the following expressions by referring to its original value denoted by R_o:

$$\frac{R(t,j,w)}{R_0} = \left[1 - \alpha\chi\bar{t}\right]^{-1} = \left[1 - \alpha\frac{9D_\sigma h_\sigma e\hat{Z}\rho j}{w^2 kT}t\right]^{-1} \qquad (5.3.1.2)$$

One may write following expression for cathode failure time (CFT) using the fact that j denotes the current density (invariant quantity for this test) at the cathode edge, which is given by $j = \rho^{-1}E_o \equiv \rho^{-1}(\Delta\vartheta / L)$. $\Delta\vartheta$ is applied voltage difference and L is the electrode to electrode specimen length, which is constant.

$$t_{CFT}(j,w,f)=\frac{f}{1+f}\frac{w^2}{9}\left[\alpha\frac{D_\sigma h_\sigma}{kT}e\hat{Z}\frac{\Delta\vartheta}{L}\right]^{-1} \qquad (5.3.1.3)$$

This expression shows that the cathode failure time depends upon the width of the interconnect quadraticaly if the cathode voiding occurs by sidewall surface diffusion. On the other hand if the cathode voiding takes place rather by the grain thinning, which implies that the diffusion path is upper and/or lower surfaces, the width in above equation should be replace by h, the thickness of the interconnect line.

In order to obtain the cathode drift regime, we have further continued our experiments by terminating the CVD condition after 95% reduction $\left(\bar{t}_{trs}\cong 0.005 \text{ for } \chi=50\right)$ in the cathode contact area (or equivalent increase in specimen resistance), and switched on the constant current test (CCT) program by allowing the whole cathode area (the complete width, $2w_0$) is exposed to the original applied electrostatic field intensity denoted by $\vec{E}_o$ (or χ invariant), and then connecting two terminal nodes, which define the remaining part of the cathode contact area (5 %), to form a fully-connected cathode contour.

ii. Cathode Drift Due to Electromigration Induced Voiding

Two different experimental procedures are applied to reveal this peculiar phenomenon. The first procedure as described in the previous section starts with application of the constant voltage differential to the electrodes up to the point of almost complete cathode failure (95% by voiding). Above figures showing profile evolutions under different electronwind intersities, belong to constant current testing (except the colors of green and magenta) which is followed after constant voltage difference testing, as described above.

According to Eq. (5.3.1.1) the complete cathode detachment actually never takes place$\left(\bar{t}_{CFT} \rightarrow \infty\right)$, under the constant voltage differential testing, because of the exponential character of the phenomenon. Therefore, the constant current source program should be activated by an external agent as soon as the distance between two leading nodes of the cathode edge becomes equal to the minimum segment length generated during the simulation experiments. This roughly corresponds to 5% of the total width in our discretization scheme.

In Fig. 5.3.1.11 cathode drift-displacements for different electronwind intensities are plotted as a function of normalized time for an interconnect subjected to the mixed-electrostatic boundary conditions as described above.

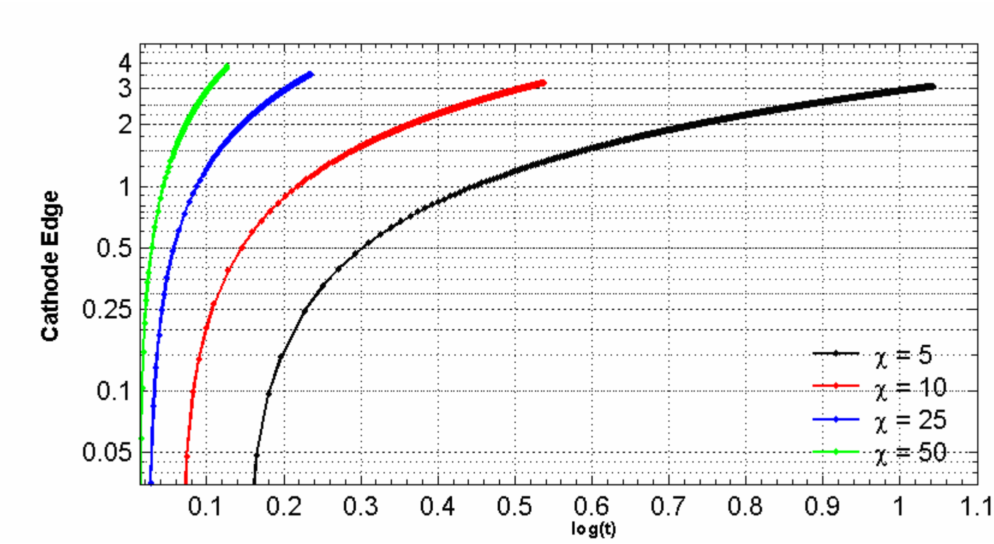

Figure 5.3.1.11: Semilogaritmic cathode-drift displacement (displacement from initial specimen length due to electromigration) versus normalized time.

This figure clearly shows the linear behavior of the cathode-drift during the constant current test procedure. The slopes (drift velocity) of these drift-displacement time plots show very systematic connection with the applied electric field intensity, which is also invariant for the constant current set-up. The results are analyzed by linear regression procedure, which deduced following analytical and very useful expression in practice.

$$\bar{d}^{CVD}_{drift}\left(\chi,\bar{t}\right)=0.661\chi\bar{t}+0.0126\bar{t} \qquad (5.3.1.4)$$

Where, the normalized elapsed time for the cathode drift is referred to the onset of the cathode edge displacement stabilization. Due to the sudden change over from the constant voltage regime to the constant current condition, the some fluctuations in the cathode edge position always take place. The extrapolation of this relationship to zero electron wind intensity parameter $\left(\chi\to 0\right)$ implies that there should be a cathode-drift phenomenon, which corresponds to the cases where there is no applied electric field$\left(\chi=0\right)$. In reality, our extensive computer simulation studies showed that one can not have any cathode voiding and drifting in the absence of the applied electric field as long as one uses the R-BC. Similarly, no accumulation takes place at the anode end if one uses R-BC there. However, as will see in the next section; FM-BC at the cathode edge results in voiding and cathode drifting even in the absence of the applied electric field.

Now, above findings can be transformed into the real time and space domain by inverse normalization procedure, which results :

$$d^{CVD}_{drift}\left(\chi,t\right)=1.983\frac{D_\sigma h_\sigma eZ\rho j}{w_0 kT}t+3.4\frac{\Omega_\sigma D_\sigma h_\sigma g_\sigma}{w_0{}^3 kT}t \qquad (5.3.1.6)$$

$$j_{thr}=\left(\frac{E_{thr}}{\rho}\right)=1.7156\frac{\Omega_\sigma g_\sigma}{w_0{}^2 eZ\rho} \qquad \text{(threshold current density)} \qquad (5.3.1.7)$$

The importance of the threshold current density may be more appreciated when we examine the behavior of the cathode drift velocity with the applied electric field. The value of the threshold current density depends linearly upon the surface specific Gibbs free of the interface between the interconnect material and its surrounding coatings, and inversely on its bulk resistivity. The specimen width (or thickness) also plays very important role on this parameter. It is easy to realize that the wide (or thick) lines show much better performance then the narrow (thin) lines as far as the deactivation of the cathode drift phenomenon is concerned.

Similarly, the cathode drift velocity may be calculated from Eq. (5.3.1.6), by taken its differential and adjusting the terms, which reads:

$$v_{drift}^{CVD} = \frac{0.983}{w} \frac{D_\sigma h_\sigma e Z \rho}{kT} \left(j + j_{thr} \right) \qquad (5.3.1.8)$$

This formula clearly shows that below the current threshold level, there is long extended plateau region in the cathode drift velocity versus applied current density plot, which may be depended on the operating temperature due to the possible temperature dependence of intrinsic properties of the interconnect material $\{Z, g_\sigma \text{ and } \rho\}$. The close inspection of the first term in above equation shows that there is very close resemblance between the cathode drift velocity in EM influence regime and the steady state drift velocity of a circular void in an infinite and isotropic interconnect as calculated analytically by Ho (1970), namely:

$$v_{drift}^{Void} = \frac{2}{r_o} \frac{D_\sigma h_\sigma e Z \rho j}{kT} \qquad (5.3.1.9)$$

where, r_o is the radius of the internal void.

5.3.2. CCT Experiments

The second approach employs free-moving boundary condition (FM-BC) at the cathode edge and reflecting boundary condition (R-BC) for the anode end of the interconnect material having an aspect ratio of $\beta = 40/3$. The constant current source (CCS) may be put into the operation from the beginning of the simulation experiments rather then waiting for the end of the complete cathode failure by the shrinkage of the contact area. This can be easily accomplished by the usage of IBEM rather then the direct BEM, which is mostly used by investigators. For the application of IBEM, we are somehow taking different path from the traditional approach for the solution of the Laplace equation under the Neumann boundary condition. First, as an initial condition we apply a constant and uniform external electric field ($\vec{E}_o = \hat{i}E_o$) to the three dimensional space in which the sample is situated. Physically this can be realized if the underlayer of high resistance material (Ta, TiN and $TiAl_3$) is acting as a shunt, similar to Blech's experiments (1975). Secondly, during the calculation of the virtual charge distribution at the specimen boundaries (the sidewalls and the cathode and anode edges), we modified the Neumann boundary conditions (NBC) such as that the part of the cathode end bounded by the original sidewalls ($2w_o$-width) of the specimen, and the whole anode edge regardless their shapes should have zero virtual electric field intensity distribution, not along surface normal of the boundary but along the direction of the applied field. On contrary to this restriction, at the sidewalls the induced electric field intensity should counter act against to the normal component of the external field at the boundary (usual Neumann BC). Hence, the actual (net) electric field intensity at the cathode and anode boundaries becomes equal to the applied electric field intensity there. Therefore, according to the Gauss theorem: the path integral along the restricted cathode profile, $I = \int_0^{2w_0} \sigma \hat{n} \bullet \bar{E} d\ell = 2w_0 \sigma E$, gives the total current flowing through the specimen, and it stays invariant regardless the shape of the contour formed at the cathode edge of the specimen.

Hence, a perfect and very efficient constant current test program using IBEM method is utilized in this program, without referring to the tedious and time consuming finite difference shame as suggested and used by Khenner et. al. (2001) and later by Averbuch et. al (2003) in order to compute the time dependent $\vartheta(x, y, t)$ electrostatic potential everywhere in the bulk material including the shunt in order to obtain the electric field intensity at the cathode contour. This shows the power of IBEM method (the constant element) to handle the electrostatic problems concerning boundaries and surfaces, which are described by most authors as the 'bottleneck' of the numerical simulations. Even for the sharp corners and edges, where the electrostatic potential is discontinuous but not the tangential component of the electric field, one can develope very efficient forward and backward extrapolation procedures, while using IBEM.

i. Electromigration Grooving & Cathode Shrinkage

Same considerations made for the constant voltage difference case can be made for Fig. 5.3.2.1 and the rest of the profile snapshots in this chapter, asymmetry towards extra mass accumulation in the windward side become more pronounced with the increase in the electron wind intensity parameter.

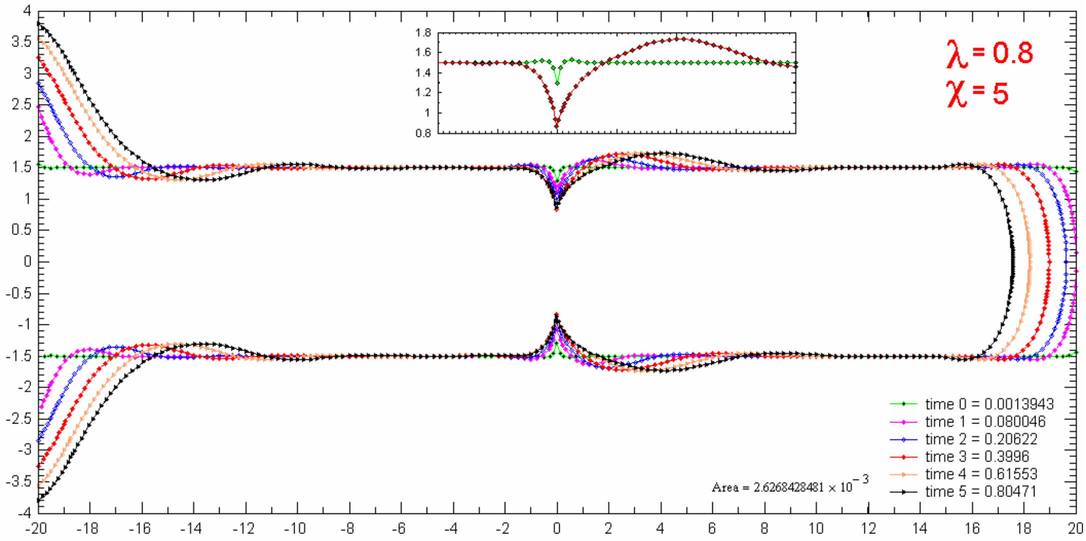

Figure 5.3.2.1: Evolution profile of the test specimen for selected time steps for $\lambda = 0.8$ and $\chi = 5$. Upper window shows the initial and final states of the groove.

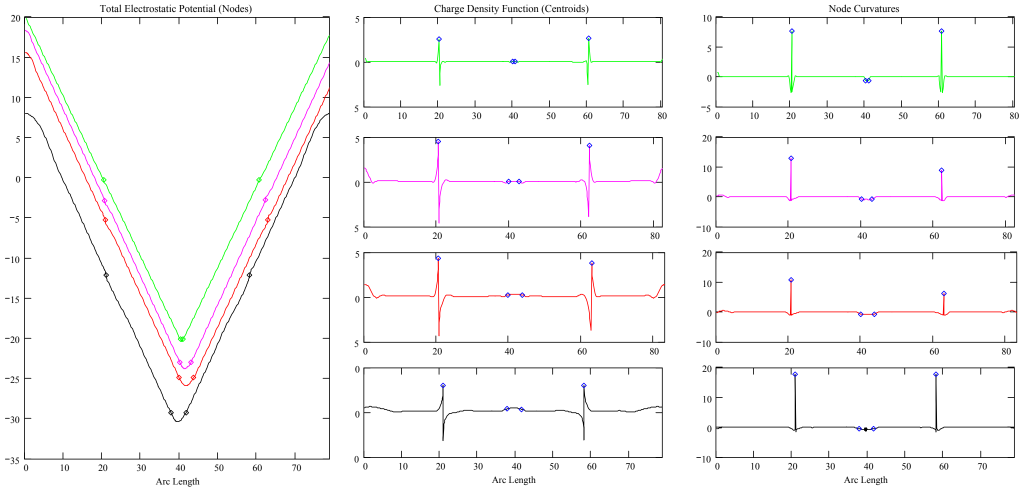

a) b) c)

Figure 5.3.2.2: a) total electrostatic potential, b) charge density function, c) curvature vs. arc length graphs, each following the color series of Fig. 5.3.2.1.

In Fig. 5.3.2.3, the triple junction depth obtained from the constant current test ($\chi = 5 - 50$ and λ=0.8) is plotted as a function of the normalized time, which also shows very similar characteristics behavior compared to the constant voltage test outcomes.

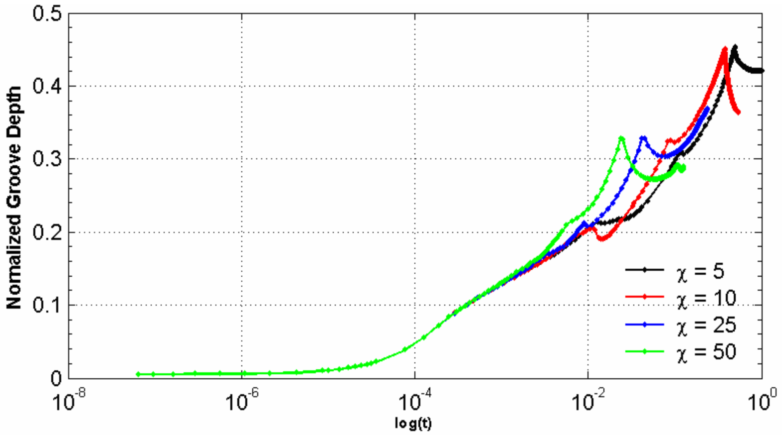

Figure 5.3.2.3: Normalized groove depth vs. normalized time graphs for $\lambda = 0.8$ and $\chi = 5 - 50$ interval.

Following figures show the effect of increasing electronwind intensity on the profile evolution for the case of constant current testing.

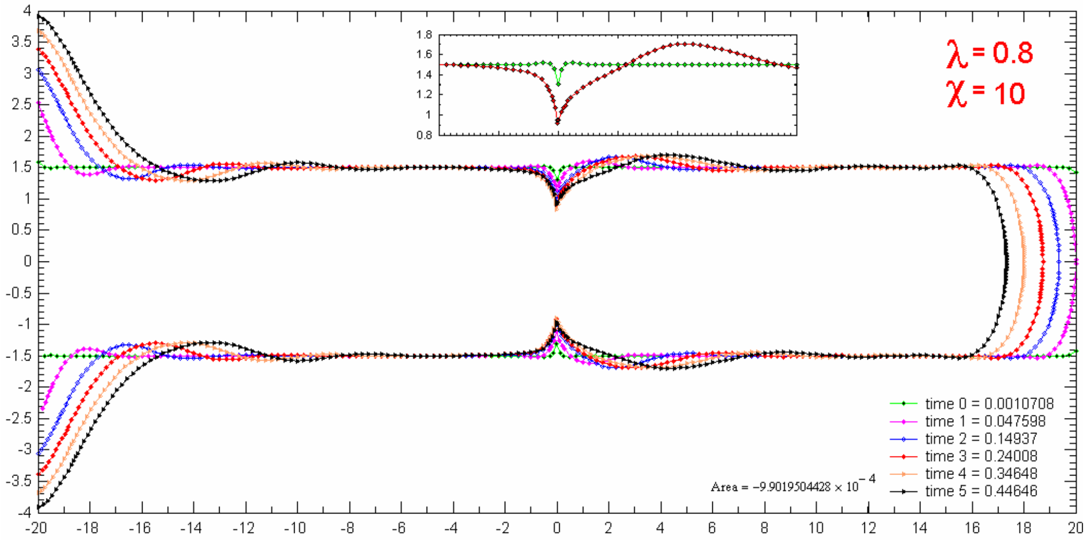

Figure 5.3.2.4: Evolution profile of the test specimen for selected time steps for $\lambda = 0.8$ and $\chi = 10$. Upper window shows the initial and final states of the groove.

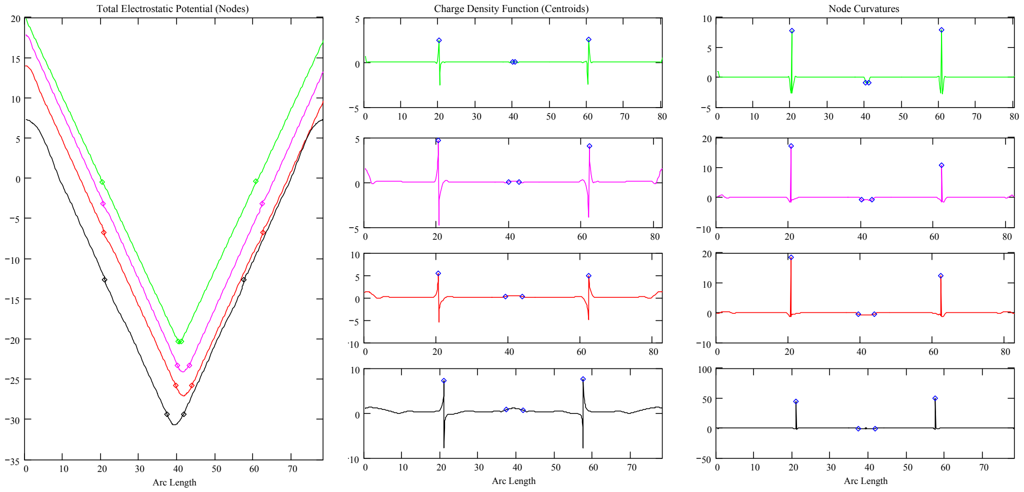

a)

b)

c)

Figure 5.3.2.5: a) total electrostatic potential, b) charge density function, c) curvature vs. arc length graphs, each following the color series of Fig. 5.3.2.4.

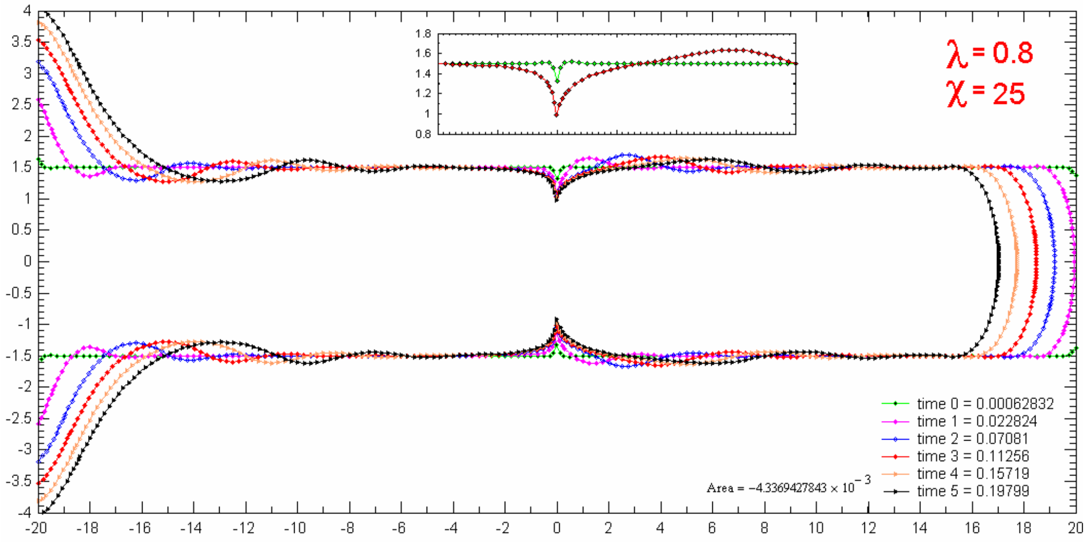

Figure 5.3.2.6: Evolution profile of the test specimen for selected time steps for $\lambda = 0.8$ and $\chi = 25$. Upper window shows the initial and final states of the groove.

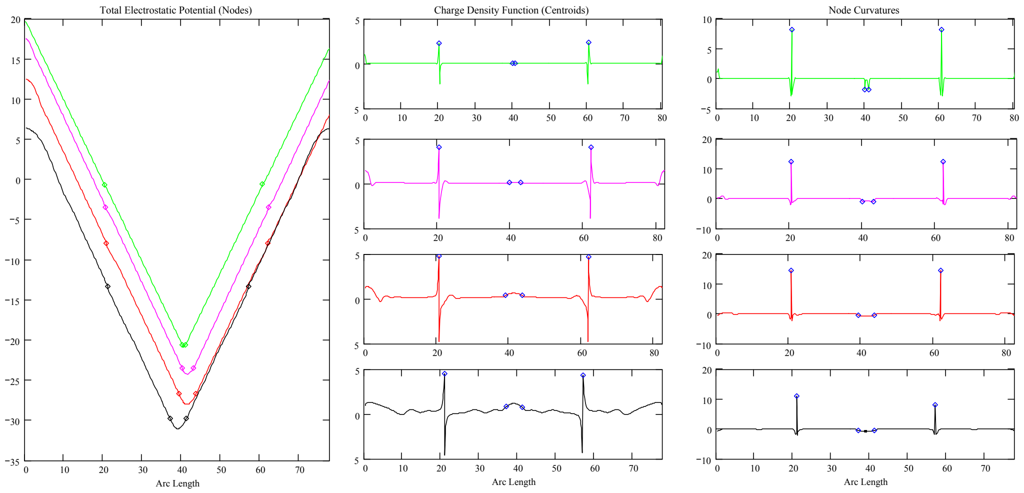

a) b) c)

Figure 5.3.2.7: a) total electrostatic potential, b) charge density function, c) curvature vs. arc length graphs, each following the color series of Fig. 5.3.2.6.

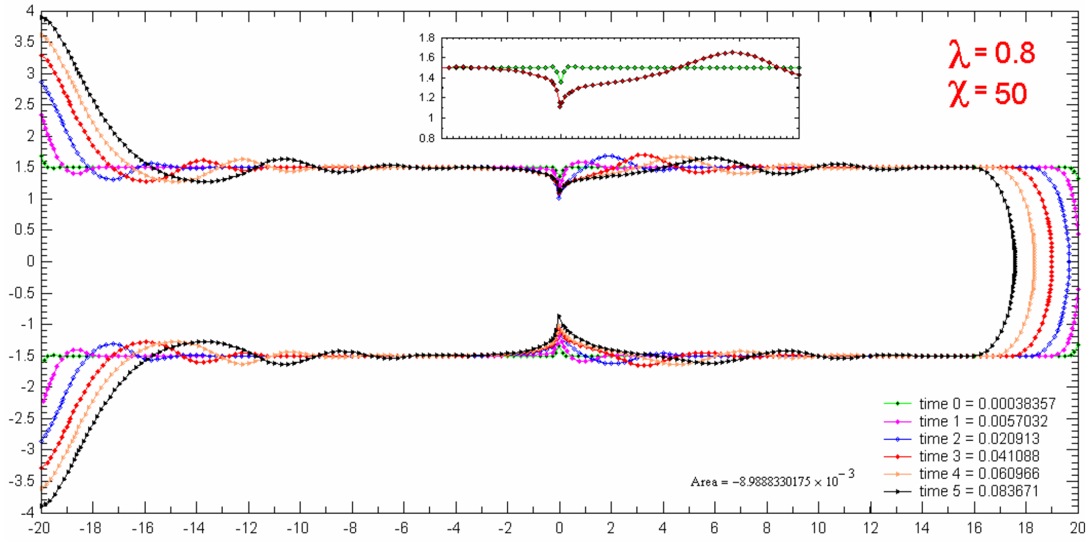

Figure 5.3.2.8: Evolution profile of the test specimen for selected time steps for $\lambda = 0.8$ and $\chi = 50$. Upper window shows the initial and final states of the groove.

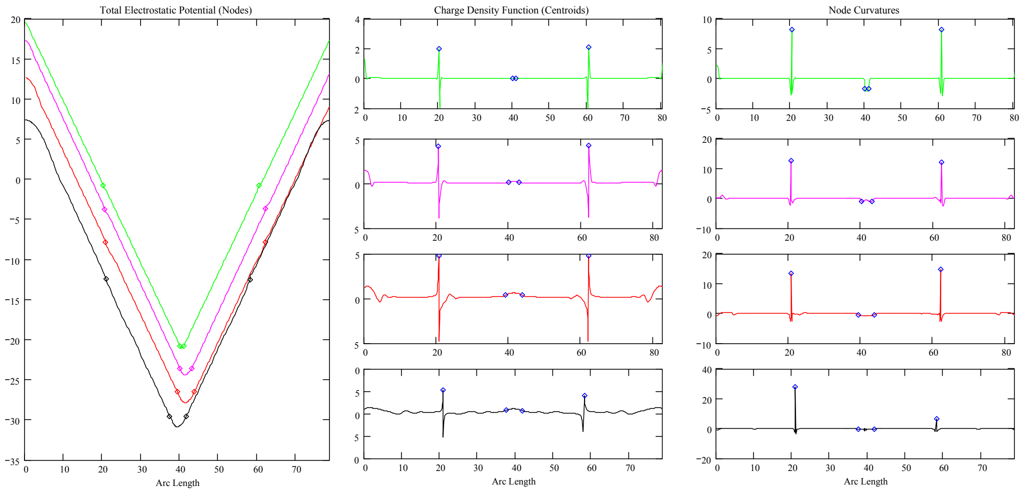

a) b) c)

Figure 5.3.2.9: a) total electrostatic potential, b) charge density function, c) curvature vs. arc length graphs, each following the color series of Fig. 5.3.2.8.

These figures clearly show the existence of the voiding (shrinkage) and edge drifting at the cathode end with FM-BC. There are no observable variations in the anode end of the surface profile, where we have employed R-BC. Linear regression analysis is applied also on the cathode voiding or shrinkage experiments, and the following analytical expressions obtained for the normalized cathode contact area or inverse electrical resistivity variations with respect the normalized time:

$$\overline{A}^{CCT}(\chi,\overline{t}) \equiv \overline{w}\left[\frac{R}{R_o}\right]^{-1} = 2\left[1-2\chi\overline{t}\right]\times\left[1+0.5\exp\left(-10\chi\overline{t}\right)\right] \ , \ \left(\chi \ge 1\right) \qquad (5.3.2.1)$$

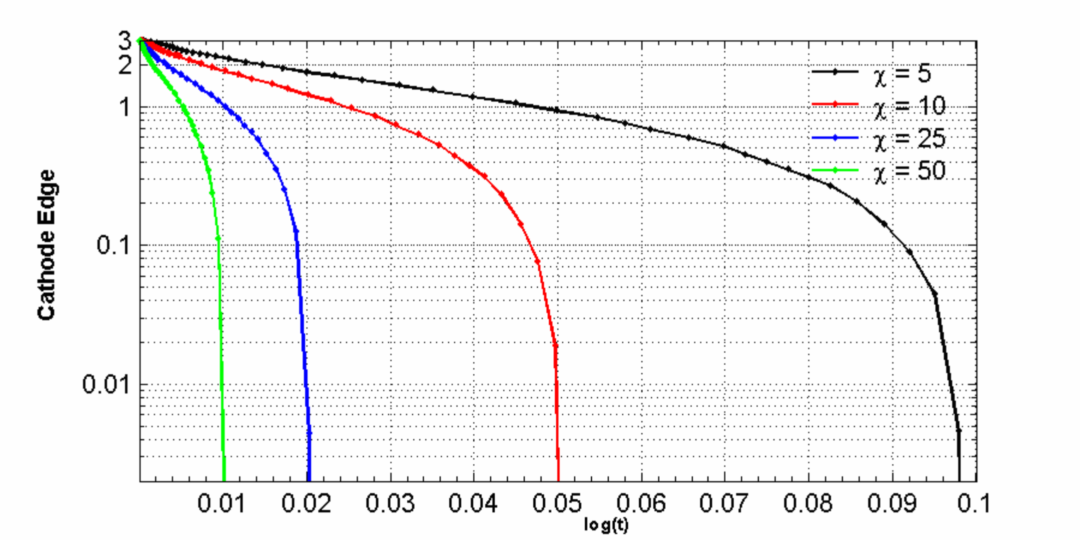

Figure 5.3.2.10: Semilogaritmic cathode contact area shrinkage versus normalized time under constant current.

Above expression clearly shows that there is a finite elapse time for the cathode failure by voiding, which is given by $\overline{t}_{CFT} = 1/(2\cdot\chi)$, in normalized time and space domain which can easily be checked from Fig. 5.3.2.10. Where $\overline{w} = 3$, is the normalized full width of the test specimen.

ii. Cathode Drift Due to Electromigration Induced Voiding

Similarly, the analytical expression for the cathode drift under the FM-BC utilizing the constant current source program is found. This is not surprisingly exactly the same analytical expression that we obtained from the constant voltage source setup as out line above, namely:

$$\overline{d}^{CCT}_{drift}\left(\chi,\overline{t}\right)=0.661\chi\overline{t}+0.0126\overline{t} \tag{5.3.2.2}$$

Where, the end of the cathode drift-incubation period, which includes the shrinkage stage, is used as a reference point for the measurements of the normalized time scale for the development of cathode edge displacement. Hence, one can easily see from above equation that as we observed independently, even under the zero applied electric field, $\chi=0$, the cathode edge drift is possible without introducing any external interference agent, as in the case of the constant voltage experiments. However, both simulations experiments, CVE and CCE give the same results, because the cathode drift stage are all driven under the same constant current source. In the first situation; it is artificially created by the switching operation, and in the second case; it is developed naturally after the termination of the cathode shrinkage stage.

Following figures compare the two experimental setup in terms of electromigration induced cathode shrinkage and drift.

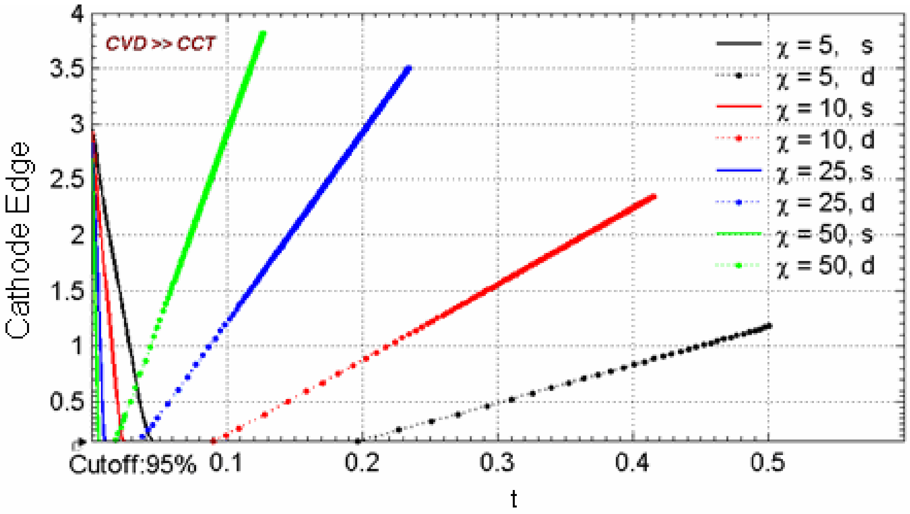

Figure 5.3.2.11: Linear cathode contact area shrinkage (s) followed by cathode drift (d) versus normalized time for set-up one.

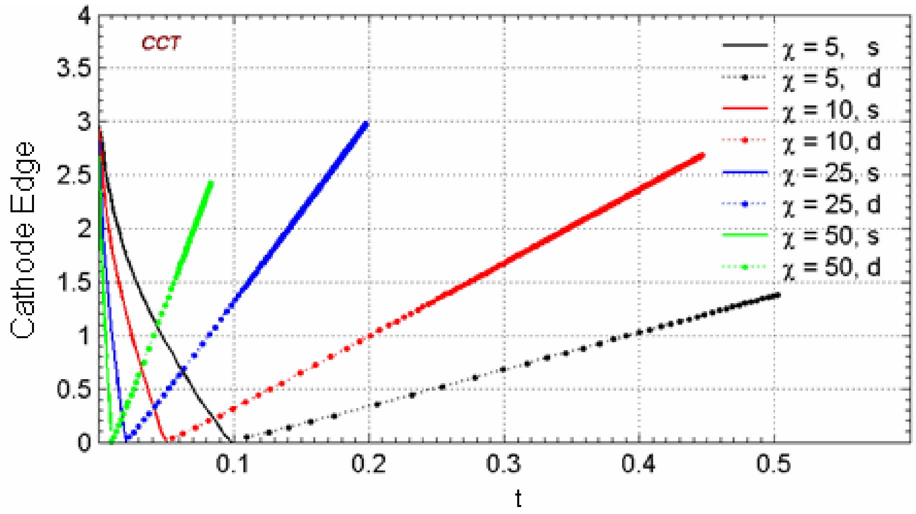

Figure 5.3.2.12: Linear cathode contact area shrinkage (s) followed by cathode drift (d) versus normalized time for set-up two.

It became obvious that the differences between the results of the constant voltage and the constant current experiments are negligibly small as far as the cathode drift phenomenon is concerned. The main difference comes from the types of the analytical functions Eq. (5.3.1.1) and Eq. (5.3.2.1) describing the time dependence of the cathode shrinkage processes at the cathode regions, respectively.

The incubation time of the cathode drift phenomenon, which is also coinciding with the time of complete cathode failure (CFT) by voiding due to surface drift-diffusion of atomic species is also analyzed. In Fig. 5.3.2.13 the incubation time versus electron wind intensity parameters $(\chi = 0.001 - 50)$ are plotted on a double logarithmic scale, where the wetting parameter and aspect ratio are chosen such as $\lambda = 0.8$ and $\beta = 40/3$, respectively. The linear regression analysis is applied to the inverse time versus electron wind intensity parameter, which resulted the following analytical expression:

$$\bar{t}_{Incu}^{CCT}(\chi) \cong \bar{t}_{CFT}(\chi) = \frac{0.5757}{0.3219 + \chi} \quad \text{(complete cathode failure time)} \qquad (5.3.2.3)$$

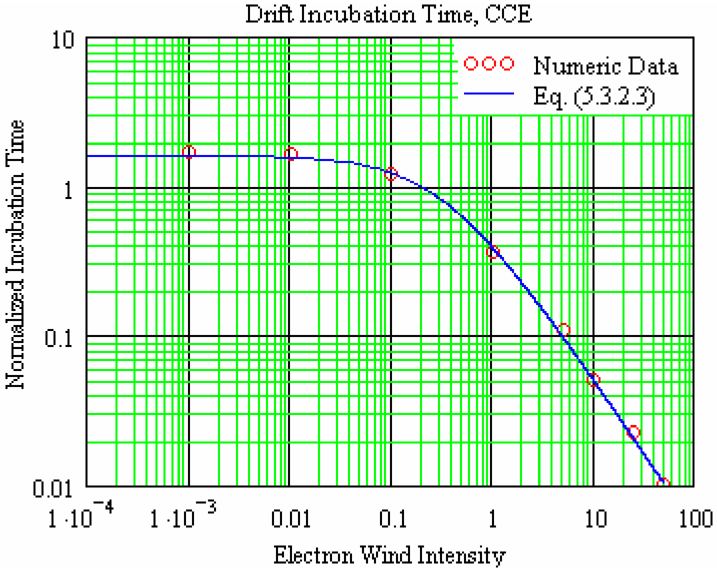

Figure 5.3.2.13: Normalized incubation time of the cathode drift phenomenon vs. electronwind intensity $\left(\chi = 0.001 - 50\right)$, and the analytical expression describing it.

Above expression is also plotted on Fig. 5.3.2.13, which shows an excellent match with the data points obtained from our computer simulation experiments under constant current condition. This modified hyperbolic function in log-log plot shows two distinct domains; the first region corresponds to the capillary dominating $\chi \leq 0.01$ plateau region, where the current exponent is equal to zero, and the second linear region $\chi \geq 1$ dominated by the applied electric field, which shows a current exponent is equal to unity. Between these two regimes lies the transition state with varying current exponent. Now we may transform above equation into the real time and space domain, which results:

$$t_{CFT}^{CCT}\left(\chi, w\right) = 0.576\left[3^2 \frac{D_\sigma h_\sigma eZ\rho j}{w^2 kT} + 0.322 \times 3^4 \frac{\Omega_\sigma D_\sigma h_\sigma g_\sigma}{w^4 kT}\right]^{-1} \text{ (sec.)} \qquad (5.3.2.4)$$

This general expression, which covers the whole domain of capillary and electromigration dominating regions can give following two formulas, which are perfectly represents both domain very accurately:

$$t_{CFT}^{CCT}\left(\chi, w\right) = 6.4\times10^{-2}\left[\frac{D_\sigma h_\sigma eZ\rho j}{w^2 kT}\right]^{-1} \text{(sec., EM dominating region)} \qquad (5.3.2.5)$$

$$t_{CFT}^{CCT}\left(\chi, w\right) = 2.2\times10^{-2}\left[\frac{\Omega_\sigma D_\sigma h_\sigma g_\sigma}{w^4 kT}\right]^{-1} \text{(sec., capillary dominating region)} \quad (5.3.2.6)$$

As mentioned before, this test configuration of the interconnect line (FM-BC) resembles the famous experimental set-up by Blech (1975), in the measurement of the drift velocity at the cathode edge. The main difference is the drift-diffusion paths between these experiments and the present chosen simulation studies. Blech is worried about the bulk drift -diffusion with or without grain boundary contributions in polygrain metal stripe under the electromigration forces. On the hand present study puts main emphasis on the evolution behavior of the single crystals and the bamboo type interconnect lines when the surface drift-diffusion becomes dominant mass transport mechanisms under the electromigration and capillary forces. As far as the validity of FM-BC is concerned the specific type of the surface paths is immaterial, which can be upper and lower surfaces or interfaces, even the lateral sides and edges of the interconnect line.

According to Hu *et al.* (1997), drift-velocity and resistance measurements in narrow (0.25 μM) bamboo-like grained structures suggests that the mass transport of Cu during electromigation measurements occur primarily along the sidewall surfaces of the line. These Cu lines, sandwiched with a top and bottom Ta layer, were connected to underlying W bars on each end of the Cu line. Above findings are also confirmed recently by Hu *et al.* (1999), who found that in narrow (0.15 μM) bamboo-like and near- bamboo structures (0.5 μM), the dominant mechanism is surface diffusion. They speculated that there is a linear relationship between failure lifetime and metal line width, despite the fact that these narrow lines were close to a perfect bamboo-like grain structure. However, according to our findings concerning the cathode voiding (Eq. (5.3.1.3)), cathode failure time should be quadratic function of the line width, which is also proved by the analysis of the data provided by Hu *et al.* (1999) presented in Fig. 5.3.2.14.

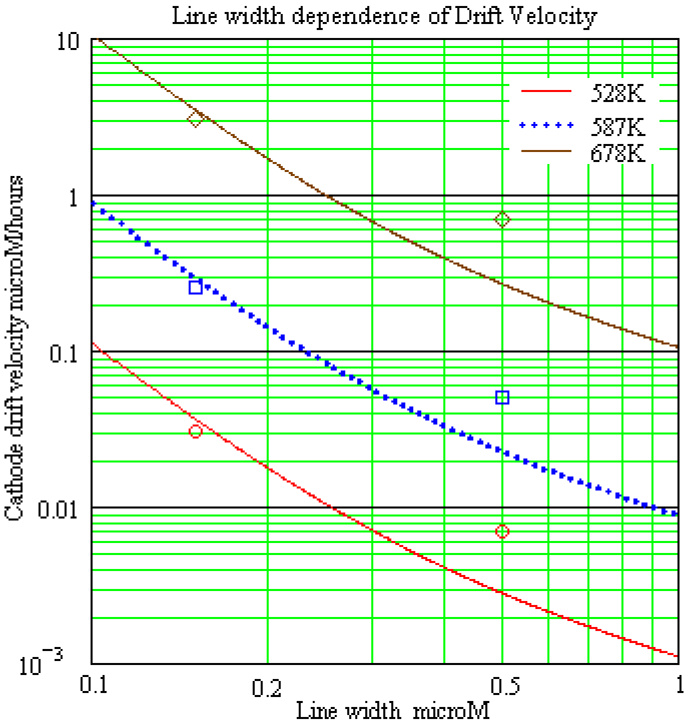

Figure 5.3.2.14: Drift velocity data by Hu *et al.* (1999) for bamboo (0.15μ) and near bamboo (0.5μ) structures.

All these experimental results suggest that the mass transport of Cu during electromigration primarily occurs along the side wall surfaces of the lines. In most recent study of Hu *et al.* (2001), experiments on $0.27\mu m$ wide Cu damascene interconnects shows that the electromigration time to failure is greatly influenced by the thickness of the metal liner at the contact between the via and underlying line. They obtained remarkably long lifetime when they used a $3nm$ thick liner (at the via/metal line interface), since the abrupt mass flux divergence at this interface normally seen is greatly diminished. This situation exactly corresponds to the perfect reflecting boundary conditions as adopted in our computer simulation studies while we were using constant voltage CVD test program. They concluded that the dominant diffusion path is along the top surface (Cu/SiN_x, interface) of a Cu damascene line. We should mention here that the results of our computer simulation studies can be easily applied to this case without to much trouble. All one has to do is to replace w line width in our equations by the line thickness denoted by h. Then, according to Eq. (5.3.1.8) the cathode drift velocity becomes inversely proportional with the line thickness (h^{-1}) as suggested by Hu *et al.* (2001) after interpreting their test results. We should mention here that the ad hoc relationship used by them for the cathode drift velocity is only valid for high current density regime, where the capillary effect doesn't play predominant role, as stated above. On the contrary to these accelerated test results, at low current densities where one operates on the plateau region, the negative effect of the specimen thickness on the cathode failure time becomes more detrimental due to the inverse cubic (h^{-3}) variation of the drift velocity with respect to the line thickness.

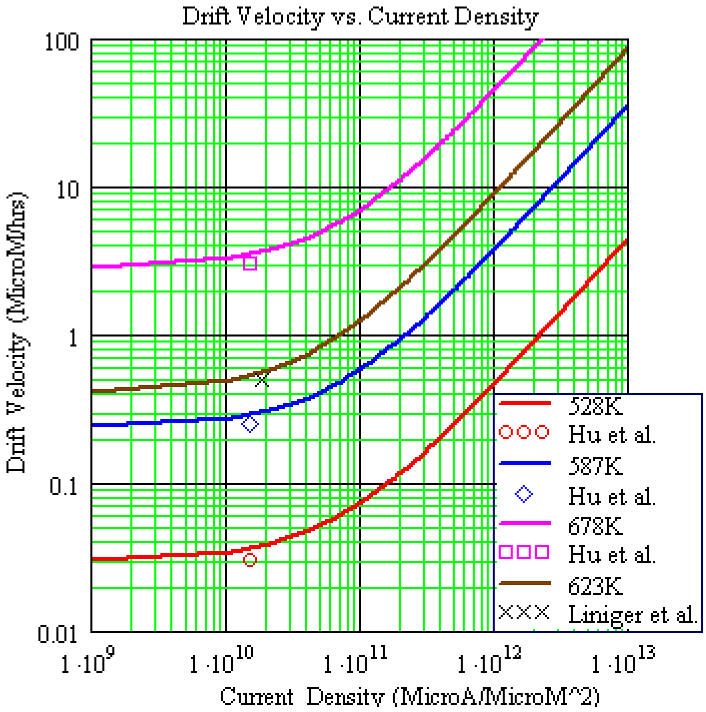

Figure 5.3.2.15: Drift velocity data by Hu *et al.* (1999), and Liniger *et al.* (2002), for different current densities.

In Fig. 5.3.2.15, the experimental data on the cathode drift velocity versus current density obtained by Hu *et al.* (1999) and Liniger *et al.* (2002) for copper interconnects exposed to different test temperatures are plotted on a double logarithmic scale. In the same plot, the cathode drift velocity relationship denoted by Eq. (5.3.1.8) is also plotted using the experimental information (the specimen width, the grain size, the current density and the test temperature) supplied by those authors in regards to their test samples. There are only three adjustable parameters in our theoretical curves such as the diffusion activation enthalpy Q_{Cu}, the effective electromigration valence $\hat{Z}_{Cu}$, and diffusivity constant denoted by D^{o}_{Cu}. The activation enthalpy can be directly and more accurately measurable from the cathode drift velocity versus temperature data.

While plotting of the theoretical curves, the diffusional parameters are used as follows: $Q_{Cu} = 0.99eV$, $D^{0}_{Cu} = 2.21\times 10^{-5} m^{2}/\sec$., and $Z_{Cu} = 12$. These figures are very close to the results obtained by Ogurtani and Oren (2004) for the surface diffusion of internal voids having no contaminations. Where, they have analyzed the available experimental data in the literature, utilizing the model developed by them for the cathode failure mean time MTTF, associated with the internal voids drifting and interacting with the grain boundaries under EM forces, in bamboo structures.

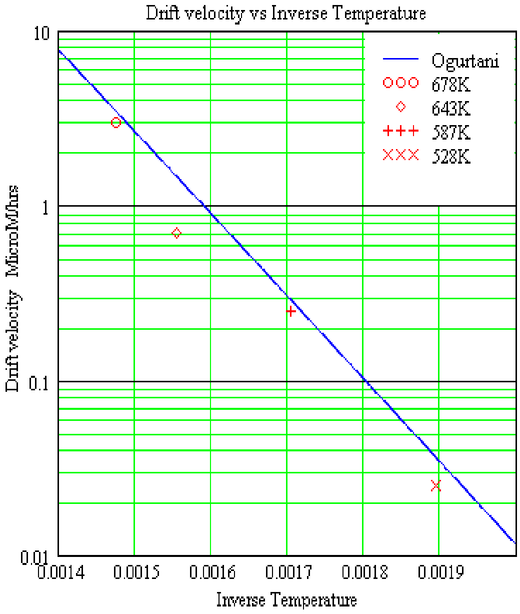

Figure 5.3.2.16: Drift velocity data by Hu *et al.* (1999), and Eq. (5.3.1.8).

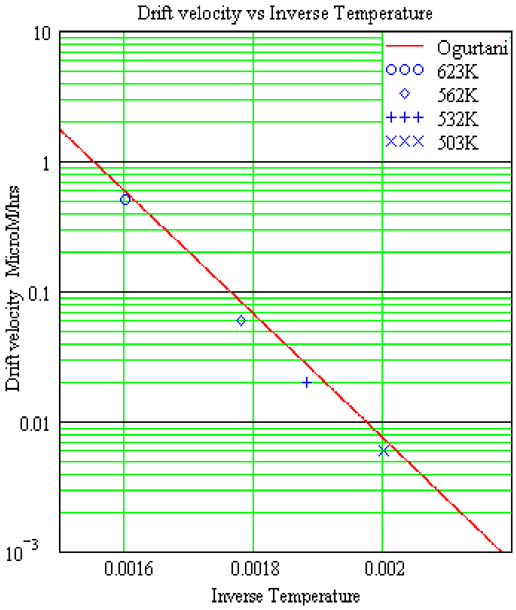

Figure 5.3.2.17: Drift velocity data by Liniger *et al.* (2002), and Eq. (5.3.1.8).

In Fig. 5.3.2.16 and Fig. 5.3.2.17, the data obtained by Hu *et al.* (1999) and Liniger *et al.* (2002) is plotted respectively in semi-logarithmic scale. The fitting of our analytical expression to those experimental data points obtained by these authors resulted in a consistent activation enthalpy of the surface diffusion such as $Q_{Cu} = 0.99eV$. On the other hand, the linear regression analysis of the data presented by Hu *et al.* (1997) and Liniger *et al.* (2002) gives same and again consistent results, namely, $Q_{Cu}^{App} = 0.93\ eV$. The main difference between these two activation enthalpy values comes from the fact that the slope obtained by linear regression analysis represents the apparent activation enthalpy, which overlooks the contribution of $1/kT$ in the mobility expression known as Einstein & Nerst relationship in the literature. Where the apparent activation enthalpy may be given by the following expression (Ogurtani and Oren 2003):

$$Q_{Cu}^{App} = -\frac{\partial V_{drift}}{\partial 1/T} = Q_{Cu} - kT \qquad (5.3.2.7)$$

Where, the temperature dependence of others parameters, which enter the theoretical expression, namely: the specific surface Gibbs free energy, the conductivity etc. are neglected. The contribution from kT amounts to $0.049\ eV$ at the temperature of about 560K, which corresponds to the mean value of the temperature range employed by those authors in their experiments. Hence, the true activation energy of the surface diffusion of copper in both experimental test conditions, which may heavily dependence upon the properties of the substrates and underlayers used, amount to $0.99\ eV$ as we obtained directly from the fitting of our theoretical expression to their data.

CHAPTER 6

CONCLUSIONS

These extensive simulation study results in certain analytical connections concerning thermal grooving, and electromigration induced cathode voiding and cathode drifting, whose proprieties are checked with the experimental data in the literature.

As far as the current density dependence of the mean cathode failure time (MTTF) is concerned, the relationship given in Eq. (5.3.2.4), which can be directly applicable to the those cases where the cathode voiding and edge thinning takes place predominantly by the mass diffusion along the paths such as sidewalls and /or upper and lower surfaces. There may be two different regimes which result completely different current exponents at high and low current densities, yielding $n=-1$ and $n=0$, respectively. The first regime is governed by the first term in Eq. (5.3.2.4), namely electromigration dominating stage, and the second regime is controlled by the second term, which is noting but capillary prevailing regime over the external applied electric field. The second regime is very important for the device operations. It seems that there is substantial decrease in actual life takes place compared to those results obtained by extrapolating the accelerated test data down to the device operating conditions; relatively low current densities and temperatures. This situation becomes more trouble some if one considers the effect of the miniaturization on MTTF. Since the second capillary dominating regime has very strong dependence on the size such as line width or thickness (h^{-3}) rather h^{-1} in the EM dominating regime.

The change over current density between these two regimes is given by Eq.(5.3.1.7) as:

$$j_{thr} = 1.7156 \frac{\Omega_\sigma g_\sigma}{w^2 e Z \rho}.$$

This threshold current density should be as small as possible for the benefit of MTTF. Hence, one should try to select those materials for the underlayers that they can be able to modify the properties of the interfacial layers to obtain low specific surface Gibbs energies, high specific resistivity and diffusion coefficients.

BIBLIOGRAPHY

YOUNG T., Philos. Trans. R. Soc. London, **95**, 65 (1805).

De DONDER Th. and Van RYSSELBERGHE P., *Affinity* (Stanford University Press, Menlo Park, California, USA) (1936).

VERSCHAFFELT J. E., Bull. Ac. Roy. Belgium (Cl. Sc.), **22**, 373 (1936).

GIBBS W., *The Collected Works of J. Willard Gibbs*, *Vol. I Thermodynamics* (Yale University Press, USA), p. 226 (1948).

BAILEY G. L. J., WATKINS H. C., Proc. Phys. Soc., **B 63**, 350 (1950).

HERRING C., *The Physics of Powder Metallurgy*, (Ed: W. E. Kinston, McGraw Hill, New York, USA), p. 143 (1951).

De GROOT S. R., *Thermodynamics of Irreversible Processes* (North-Holland Pub. Co., Amsterdam, Holland), p. 98 (1951).

BARDEEN J. and HERRING C., *Atom Movements* (American Society for Metals, Ed: J. H. Hollomon, Cleveland, Ohio, USA), p. 87 and 93 (1951).

Von-NEUMANN J., *Metal Interfaces* (American Society for Testing Materials, Cleveland, USA), p. 108 (1952).

MULLINS W.W., J. Appl. Phys., 28 (3), 333 (1957).

CHAN J. W. and HILLARD J. E., J. Chem. Phys., **28**, 258 (1958).

GUGGENHEIM E. A., *Thermodynamics*, 3rd Edition (North-Holland, Amsterdam, Holland), p. 46 and 375 (1959).

MULLINS W.W., SHEWMON P.G., Acta Metallurgica, **7**, 163 (1959).

HUNTINGTON, H.B., and GRONE, A.R., J. Phys. Chem. Solids, **20**, 76 (1961).

PRIGOGINE I., *Introduction to Thermodynamics of Irreversible Processes* (Interscience, New York, USA), p. 28, 29 and 34, (1961).

MYKURA, H., Acta Metall., **9**, 570 (1961).

DEFAY R., PRIGOGINE I., and BELLEMANS A., *Surface Tension and Adsorption* (John Wiley & Sons, New York, USA) (1966).

HAASE R., *Thermodynamics of Irreversible Processes* (Addison-Wesley, Massachusetts, USA), p. 245 (1969).

HO P.S., J. Appl. Phys., **41 (1),** 64 (1970).

ROBERTSON W.M., J Appl. Phys. **42 (1)**, 463 (1971).

OHRING M., J Appl Phys, **42,** 2653 (1971).

CHUANG T. and RICE J. R., Acta Metall., **21**, 1625 (1973).

BLECH I. A., J. Appl. Phys., **47**, 1203 (1976).

LANDAU L.D., LIFSHITZ E.M., *Statistical physics* (Pergamon Press, Oxford, Part II), p. 178 (1976).

YEREMIN E. N., *The Foundation of Chemical Kinetics* (MIR Publishers, Moscow, Russia), p. 215 (1979).

PHARR G. M. and NIX W. D., Acta Metall., **27**, 1615 (1979).

RICE J. and CHUANG T. J., J. Am. Ceram. Soc., **64 (1)**, 50 (1981).

SHARMA, SPITZ, Journal of Materials Science, **16** Letters, 535 (1981).

SRINIVASAN, Materials Science, 275 (1981).

ALLEN D.J., Scripta Metallurgica, **16**, 5 (1982).

OGURTANI T. O. and SEEGER A. K., J. Chem. Phys., **79 (10)**, 5041 (1983).

HUANG H. L., YANG J. S., J. Phys. D: Appl. Phys., **20**, 493 (1987).

TAKAHASHI Y., TAKAHASHI K. and NIGHIGUCHI K., Acta Metall. Mater., **39 (12)**, 3199 (1991).

ARZT E., and NIX W. D., J. Mater. Res. **6**, 731-736 (1991).

LIU, C.-L., COHEN, J.M., ADAMS, J.B., VOTER A.F., Surface science **253**, 334 (1991).

BEER G. and WATSON J. O., *Introduction to Finite and Boundary Element Methods for Engineers* (John Wiley & Sons, New York, USA), p. 141 (1992).

MATHEWS J. H., *Numerical Methods for Mathematics, Science and Engineering* (Prentice-Hall International Edition, New Jersey, USA), p. 148 (1992).

NIX W. D., and ARZT E., Metall. Trans., **23A**, 2007 (1992).

GENIN F.Y., MULLINS W. W., WYNBLATT P., Acta metal. Mater., **41**, 3541 (1993).

THOULESS M.D., Acta Metall. Mater. **21**, 1625 (1993) .

KLINGER L.M., GLICKMAN E.E., FRADKOV V.E., MULLINS W.W., BAUER C.L., J Appl Phys, **78**, 3833 (1995).

LIU C.-L., International Journal of Modern Physics **B9**, 1 (1995).

ZHANG W, SCHNEIBEL J.H. Computational Materials Sci, **3**, 347 (1995).

LEE K. L., HU C.-K., TU K. N., J. Appl. Phys. **78**, 4428 (1995).

CAHN J., ELLIOTT C., and NOVICK-COHEN A., Eur. J. Appl. Math., **7**, 287 (1996).

WANG W., SUO Z., and HAO T. H., J. Appl. Phys., **79**, 2394 (1996).

WONG H., MIKSIS M.J., VOORHEES P.W., DAVIS S.H., Acta Mater, **45,** 2477 (1997).

SUN B, SUO Z. Acta Mater, **45**, 4953 (1997).

BLECH I. A., Acta Mater., **4 (11)**, 3717 (1998).

KAGEYAMA M., ABE K., HARADA Y., ONODA H., Mater. Res. Soc. Symp. Proc., **514**, 91 (1998).

SUO Z., Acta Mater., **46 (11),** 3725 (1998).
KAZARYAN A., WANG Y. and PATTON B. R., Scripta Mater., **41** (5), 487 (1999).

MAHADEVAN M. and BRADLEY R. M., Physica D, **126**, 201 (1999).

GUNGOR M. R. and MAROUDAS D., J. Appl. Phys., **85 (4)**, 2233 (1999).

HU C.-K., ROSENBERG R., LEE K. Y., Appl. Phys. Lett., **74**, 2945 (1999).

HUANG P., LI Z. and SUN J., Model. Simul. Mater. Sci. Eng., **8**, 843 (2000).

OGURTANI T. O., *Irreversible Thermokinetics Theory of Surfaces and Interfaces with a Special Reference to Triple Junctions (unpublished)* (2000).

OREN E. E., M. Sc. Thesis, Middle East Technical University (2000).

KOETTER T. G., WENDROCK H., SCHUEHRER H., WENZEL C., WETZIG K., Microelectron. Reliab. **40**, 1295 (2000).

NATHAN M, GLICKMAN E, KHENNER M, Appl. Phys. Lett., **77 (21),** 3355 (2000).

PROOST J., HIRATO T., FURUHARA T., MAEX K., JCELIS.-P., J. Appl. Phys. **87**, 2792 (2000).

RABKIN E., KLINGER L., SEMENOV V., Acta Mater **48 (7)**, 1533 (2000).

OGAWA E. T., BIERWAG A. J, LEE K. –D., MATSUHASHI H., JUSTISON P. R., RAMAMURTHI A. N., and HO P. S., BLASCHKE V. A., GRIFFITHS D., NELSEN A., BREEN M., and HAVEMANN R., *Electromigration Study of Cu/Oxide Dual-Damascene Interconnects* (4th Annual Topical Research Conference (TRC) on Reliability Session 5, Stanford University, CA) (2000).

SUO Z., MA Q., MEYER W.K., *Unpublished* (2000).

HUANG P., LI Z., SUN J., Computational Materials Science **20**, 66 (2001).

OGURTANI T. O. and OREN E. E., J. Apply. Phys., **90 (3)**, 1564 (2001).

OREN E. E. and OGURTANI T. O., Mat. Res. Soc. Symp. Proc. (Ed: S. Lahiri), **714 E**, p. L9.2.1 (2001).

LIU C. Y., LEE S. and CHUANG T. J., Mat. Sci. Eng. B-Solid, **86**, 101 (2001).

KLINGER L, RABKIN E, Interface Sci., **9 (1-2)**, 55 (2001).

KHENNER M., AVERBUCH A., ISRAELI M. and NATHAN M., J. Comput. Phys., **170**, 764 (2001).

NOVICK -C. A., Physica D, **137**, 1 (2001).

AVERBUCH A, ISRAELI M, RAVVE I, J. Comput. Phys., **167 (2)**, 316 (2001).

LINIGER E., GIGNAC L., HU C.-K., KALDOR S., J. Appl. Phys., **92 (4)**, (2002).

GUNGOR M. R. and MAROUDAS D., International Journal of Fracture, **109**, 47, (2001).

GOTTSTEIN G. and SHVINDLERMAN L. S., Acta Mater., **50**, 703 (2002).

ZHANG W., SACHENKO P., SCHNEIBEL J. H., J. Mater. Res., **17 (6)**, (2002).

OREN E. E. and OGURTANI T. O., Mat. Res. Soc. Symp. Proc. (Eds: C. S. Ozkan, R. C. Cammarata, L. B. Freund, H. Gao), **695**, p. L.5.5.1 (2002).

XIN T., WONG H., Acta Materialia, **51,** 2305 (2003).

OGURTANI T. O. and OREN E. E., *Irreversible Thermokinetics Theory of Surfaces and Interfaces with a Special Reference to Void Intergranular Motion under the action Electromigration Forces (unpublished),* (2003).

OREN E. E., Ph. D. Thesis, Middle East Technical University (2003).

AVERBUCH A, ISRAELI M, NATHAN M, J. Comput. Phys., **188 (2)**, 640 (2003).

ZHANG W., SACHENKO P., GLADWELL I. I., Acta Materialia, **52**, 107 (2004).

APPENDIX

COMPUTER CODE

```
/*************************************************************************
                 Grain Boundary Grooving + Cathode Drift

                 Finite Interconnect with Grain Boundary:

Boundary element method used in the solution of the Laplace equation
related to the groove growth under the effect of electron wind in a finite
interconnect which is incorporated with the surface diffusion
due to curvature dependent chemical potential.

Utilizes RC-BC at anode, FM-BC at cathode.

Modified     : 10 December 2003, CSL, Ankara, Turkey
Copyright    : (C) 2003 by Oncu AKYILDIZ
Email  : oncu_a@yahoo.com
*************************************************************************/

#include <iostream.h>
#include <iomanip.h>
#include <math.h>
#include <time.h>
#include <fstream.h>
#define pi  3.14159265358979323846264338327950
#define sqr(x) ((x)*(x))
#define magnitude(a,b,c) sqrt(a * a + b * b + c * c)
#define dotpro(a0,a1,a2,b0,b1,b2) (a0*b0+a1*b1+a2*b2)
#define sign(a) ((a>0) ? (1):(-1))
using namespace std;
typedef double arr1[1001];
typedef double arr2[3][1001];
typedef double arr3[1001][1001];
typedef double arr4[3];
typedef double arr5[3][3];
int    mdiv,mc,nloop,nt,nu,nl,ms,t,gb1,gb2,gmdiv,newdata,mint,ca,cu,cd;
double sl,sw,timet,omega,vmax,mpow,e,emax,emin,rmax,rmin,ksi,dm,delta,mgl
       ,mgb,tmgb,dot,ddot,dotp,alfa,beta,lamda,lamda1,lamda2,deltat,epstime
       ,dihedral1l,dihedral2l,dihedral1r,dihedral2r,vgb1,vgb2,H,a,b,c,HL;
arr1   su,psi,ekap,tetau,kapkapu,v,cff,mu,fieldtn,fieldt;
arr2   delru,rt,rg,noo,llnu,noc,rcw;
arr3   tt;
arr4   tgu,tgd,rui,ruii,ruf,vect;
arr5   anti;
string sy;
```

```
/*      this function determines the record time steps */
int timer(int m, int e){
        int powa = 1;
        if (e != 0)  {
                for (int ki = 1; ki <= e; ki++)  powa *= m;
        }
        return powa;
}
/*      this function finds the vector product of two vectors */
inline void vectorpro(double a0,double a1,double a2,double b0, double
b1,double    b2){
        vect[0] = a1*b2-a2*b1;
        vect[1] = -a0*b2+a2*b0;
        vect[2] = a0*b1-a1*b0;
}
/*      production of a anticlockwise rotation matrix  */
void antirotma(double w){
        anti[0][0] = cos(w);
        anti[0][1] = -sin(w);
        anti[0][2] = 0.0;
        anti[1][0] = sin(w);
        anti[1][1] = cos(w);
        anti[1][2] = 0.0;
        anti[2][0] = 0.0;
        anti[2][1] = 0.0;
        anti[2][2] = 1.0;
}
/*      Gauss Jordan elimination method in the solution of simulataneous set
        equations au=b      */
void trian(long colon, double *tek, double (*cift)[1001]){
        arr1 ddd;
        arr3 trio;
        long ki, kj, kk, de;
        double tot, bol, max;
        for (ki = 0; ki <= colon; ki++)  cift[ki][colon + 1] = tek[ki];
        for (ki = 0; ki <= colon; ki++)  {
                max = fabs(cift[ki][ki]);
                de = ki;
                for (kk = ki; kk <= colon; kk++) {
                         if (max < fabs(cift[kk][ki]))   {
                                max = cift[kk][ki];
                                de = kk;
                        }
                }
                if (de != ki){
                        for (kk = 0; kk <= colon + 1; kk++)     {
                                ddd[kk] = cift[ki][kk];
                                cift[ki][kk] = cift[de][kk];
                                cift[de][kk] = ddd[kk];
                        }
                }
                bol = cift[ki][ki];
                for (kj = 0; kj <= colon + 1; kj++)     cift[ki][kj] /= bol;
                for (kk = ki; kk <= colon; kk++) {
                        if (kk != ki){
                                for (kj = 0; kj <= colon + 1; kj++)
        trio[ki][kj]                    = cift[ki][kj] * cift[kk][ki];
                                for (kj = 0; kj <= colon + 1; kj++)
        cift[kk][kj]                    -= trio[ki][kj];
                        }
                }
        }
        mu[colon] = cift[colon][colon + 1];
        for (ki = 1; ki <= colon; ki++)  {
                 tot = 0.0;
```

```
			for (kj = 1; kj <= ki; kj++) tot += mu[colon - kj + 1] *
				cift[colon - ki][colon - kj + 1];
			mu[colon - ki] = cift[colon - ki][colon + 1] - tot;
		}
}
double det(double a11,double a12,double a13,double a21,double a22,double
	a23,double a31,double a32,double a33)
{
	return (a11*a22*a33+a12*a23*a31+a13*a21*a32-a13*a22*a31-a12*a21*a33-
	a11*a23*a32);
}
void inter(double x0,double x1,double x2,double y0,double y1,double y2)
{
	arr5 a2,b2,c2,del;
	double ddel;
	a2[0][0] = y0;
	a2[0][1] = x0;
	a2[0][2] = 1;
	a2[1][0] = y1;
	a2[1][1] = x1;
	a2[1][2] = 1;
	a2[2][0] = y2;
	a2[2][1] = x2;
	a2[2][2] = 1;
	b2[0][0] = sqr(x0);
	b2[0][1] = y0;
	b2[0][2] = 1;
	b2[1][0] = sqr(x1);
	b2[1][1] = y1;
	b2[1][2] = 1;
	b2[2][0] = sqr(x2);
	b2[2][1] = y2;
	b2[2][2] = 1;
	c2[0][0] = sqr(x0);
	c2[0][1] = x0;
	c2[0][2] = y0;
	c2[1][0] = sqr(x1);
	c2[1][1] = x1;
	c2[1][2] = y1;
	c2[2][0] = sqr(x2);
	c2[2][1] = x2;
	c2[2][2] = y2;
	del[0][0] = sqr(x0);
	del[0][1] = x0;
	del[0][2] = 1;
	del[1][0] = sqr(x1);
	del[1][1] = x1;
	del[1][2] = 1;
	del[2][0] = sqr(x2);
	del[2][1] = x2;
	del[2][2] = 1;
	ddel =
	det(del[0][0],del[0][1],del[0][2],del[1][0],del[1][1],del[1][2],
	del[2][0],del[2][1],del[2][2]);
	a =
	det(a2[0][0],a2[0][1],a2[0][2],a2[1][0],a2[1][1],a2[1][2],a2[2][0],
	a2[2][1],a2[2][2])/ddel;
	b =
	det(b2[0][0],b2[0][1],b2[0][2],b2[1][0],b2[1][1],b2[1][2],b2[2][0],
	b2[2][1],b2[2][2])/ddel;
	c =
	det(c2[0][0],c2[0][1],c2[0][2],c2[1][0],c2[1][1],c2[1][2],c2[2][0],
	c2[2][1],c2[2][2])/ddel;
}
```

```
/*     this procedure generates the initial system    */
void generate(){
       nt = 4*mdiv+2*mc;
       for (int kl = 0; kl <= 4*mdiv+2*mc; kl++){
              if (kl <= 2*mdiv){
                     rt[0][kl] = (kl-mdiv)*sl/mdiv;
                     rt[1][kl] = sw;
              }
              if (kl > 2*mdiv){
                            if (kl <= 2*mdiv+2*mc-1){
                                   rt[0][kl] = sl;
                                   rt[1][kl] = -(kl-2*mdiv-mc)*sw/mc;
                            }
                            else{
                                   rt[0][kl] = -(kl-3*mdiv-2*mc)*sl/mdiv;
                                   rt[1][kl] = -sw;
                            }
              }
              rt[2][kl] = 0;
       }
}
void delr1(){
       for (int ki = 0; ki<=nt-1; ki++)
       {
              for (int kj = 0; kj<=2; kj++)
                     delru[kj][ki] = rt[kj][ki+1]-rt[kj][ki];
              su[ki] = magnitude(delru[0][ki],delru[1][ki],delru[2][ki]);
       }
}
void psir(){
       double dummy;
       for (int ki = 1; ki<=nt-1; ki++){
              vectorpro(delru[0][ki-1],delru[1][ki-1],delru[2][ki-
                     1],delru[0][ki],delru[1][ki],delru[2][ki] );
              dummy = (magnitude(delru[0][ki-1],delru[1][ki-1],delru[2]
              [ki-1]))*(magnitude(delru[0][ki],delru[1][ki],delru[2][ki]));
              tetau[ki] =asin(dotpro((vect[0]/dummy),vect[1]/dummy,
              vect[2]/dummy,0,0,1));
              dummy = dotpro( delru[0][ki-1],delru[1][ki-1],delru[2]
              [ki-1],delru[0][ki],delru[1][ki],delru[2][ki] );
              if ( dummy <= 0 ){
                     tetau[ki] = pi - tetau[ki];
              }
              if (tetau[ki] > pi){
                     tetau[ki] = tetau[ki] - 2*pi;
              }
              tetau[ki] = -tetau[ki];
       }
}
/*     This procedure calculates the local curvature and the local line
       normal vector at any given node knowing the successive segment
       vector set in this procedure:
        kapkap : local curvature
        lln    : local line normal */
void kappa()
{
       for (int ki = 1; ki<=nt-1; ki++)
       {
              alfa = atan(sin(tetau[ki])/((su[ki-1]/su[ki])
              +cos(tetau[ki])));
              kapkapu[ki] = 2*sin(alfa)/su[ki];
              beta = (pi-2*alfa)/2;
              antirotma(-beta);
              for (int kj = 0; kj<=2; kj++)
              {
                     noo[kj][ki] =       anti[kj][0]*delru[0][ki]
                     +anti[kj][1]*delru[1][ki]+anti[kj][2]*delru[2][ki];
```

```
        }
        for (int kj = 0; kj<=2; kj++)
        {
            llnu[kj][ki] = noo[kj][ki]
            /magnitude(noo[0][ki],noo[1][ki],noo[2][ki]);
        }
        kapkapu[ki] = -kapkapu[ki];
    }
    for (int kj = 0; kj<=2; kj++)
    {
        llnu[kj][nt] = llnu[kj][nt-1];
        llnu[kj][0] = llnu[kj][1];
    }
    kapkapu[0] = kapkapu[1];
    kapkapu[nt] = kapkapu[nt-1];
}
/*  This procedure calculates the normal unit vectors at the centroids
    for   the upper and lower cut interfaces. Directions towards the
    interconnect material for edges. */
void noc1()
{
    for (int i=0; i<=nt-1; i++)
    {
        vectorpro(0,0,-1,delru[0][i],delru[1][i],delru[2][i]);
        noc[0][i] = vect[0]/su[i];
        noc[1][i] = vect[1]/su[i];
        noc[2][i] = vect[2]/su[i];
    }
}
/*  This procedure calculates the centroid position vectors for the
    whole upper and lower edges      */
void rcw1()
{
    for (int ki=0; ki<=nt-1; ki++)
        for (int kj=0; kj<=2; kj++)
            rcw[kj][ki] = ( rt[kj][ki]+rt[kj][ki+1] )/2;
}
/*  Indirect Boundary Element Method
    This is an electrostatic connection matrix utilizing the element
    centroids, m is the numder of subsegment used in the integration
    procedure. */
void tin()
{
    arr1 rcij;
    arr2 rc;
    double tot, total, rcos, rcms;
    for (int i=0; i<=nt-1; i++)
    {
        for (int j=0; j<=nt-1; j++)
        {
            if (i == j)  tt[i][j] = 0.5;
            else
            {
                for (int k=0; k<=mint; k++)
                    for (int kj=0; kj<=1; kj++)
                rc[kj][k] = (rt[kj][j]-rcw[kj][i])
                +k*delru[kj][j]/mint;
                    rcij[0] = 0;
                    rcij[1] = 0;
                for (int kj=0; kj<=1; kj++)
                    for (int k=1; k<=mint-1; k++)rcij[kj] +=
                    rc[kj][k]/(sqr(rc[0][k])+sqr(rc[1][k]));
                    rcos = sqr(rc[0][0])+sqr(rc[1][0]);
                    rcms = sqr(rc[0][mint])+sqr(rc[1][mint]);
                for (int kj=0; kj<=1; kj++)      rcij[kj] +=
                    0.5*(rc[kj][0]/rcos+rc[kj][mint]/rcms);
        tt[i][j] =  - su[j]*
```

```
        dotpro(noc[0][i],noc[1][i],0,rcij[0],rcij[1],0)*0.5/(pi*mint);
                        }
                }
        }
}
/*      CF is the normal component of the electric fied on the both strip
        surfaces     as well as the anod and cathod edges. Due to the
        applied voltage along the x-axis. Where we assumed that the cathod
        edge exposed to the applied current sources and sinks, therefore not
        insulated like others surfaces. */
void cf()
{
        for (int ki=0; ki<=nt-1; ki++){
                if ((ki>=cu-2) && (ki<=cd+1))    cff[ki] = 0;
                else   cff[ki] = -noc[0][ki];
        }
}
/*      Calculation of the electrostatic potential due to the boundary
        charge distribution at any point in the interior region or at the
        boundary rq denotes the position vector.
        field1  :  electrostatic  applied  voltage  along  the  negative  x
        direction.(electric field in the positive direction)
        field2 : electrostatic potential due to boundary charge distribution
                which satisfies the neumann condition.
        fieldt : total electrostatic potential at the void surface. */



void field()
{
        double eta,tot;
        arr1   rrq,rrq1,rrkq,delu,fieldi,fieldii;

/*      Below line generates mu that is the charge to be inserted in order
        to satisfy the Neumann Boundary Condition along the free
        surfaces, by using procedure trian. "mu" is a charge density
        function at a given segment which is assumed to be uniformly
        distributed along each segment.  */
        trian(nt-1, cff, tt);
/*      delu calculation and field2      */
        for (int i=0; i<=nt-1; i++){
                fieldi[i] = -1*rcw[0][i]; // fieldi
                for (int j=0; j<=nt-1; j++){
                        for (int kj=0; kj<=1; kj++){
                                rrq[kj] = rt[kj][j]-rcw[kj][i];
                                rrq1[kj] = rt[kj][j+1]-rcw[kj][i];
                        }
                        eta =  0.5*(log(magnitude(rrq[0],rrq[1],0))
                        +log(magnitude(rrq1[0],rrq1[1],0)));
                        tot = 0;
                        for (int k=1; k<=mint-1; k++){
                                for (int kj=0; kj<=1; kj++)
                                        rrkq[kj] = rt[kj][j]+k*(rt[kj][j+1]-
                                rt[kj][j])/mint-rcw[kj][i];
                                tot = tot+log( magnitude(rrkq[0],rrkq[1],0) );
                        }
                        delu[j] = -0.5*fabs(su[j])*(tot+eta)/(pi*mint);
                }
                fieldii[i] = 0;
                for (int kl=0; kl<=nt-1; kl++)fieldii[i] += delu[kl]*mu[kl];
                fieldt[i] = fieldi[i]+fieldii[i];  // fieldt
        }
/*      Below lines transfer the centroid data to the node positions for the
        whole system. */
        fieldtn[0] = fieldt[0];
        for (int i=1; i<=nt-1; i++)      fieldtn[i] = ( fieldt[i-1]*su[i]
        +fieldt[i]*su[i-1] )/(su[i]+su[i-1]);
```

```
        fieldtn[nt] = fieldt[nt-1];
}
void tg(){
        arr1 dummy;
        for (int kj=0; kj<=2; kj++)
        {
                dummy[kj] = rt[kj][gb2]-rt[kj][gb1];
        }
        for (int kj=0; kj<=2; kj++)
        {
                tgu[kj] = dummy[kj]/magnitude(dummy[0],dummy[1],dummy[2]);
                tgd[kj] = -tgu[kj];
        }
}
/*      This procedure calculates the node velocities at the upper and lower
        strip edges and also at the grain boundary nodes as proposed by
        Ogurtani theory, and then calculates the new node positions */
void vcalc()
{
                arr1 dummy1,dummy2,dummy3,dummy4;
                double dummy1c,dummy2c,dummy3c,dummy4c,dummy1d,dummy2d,
                dummy3d,dummy4d,dummymt1,dummymt2,dummyx,dummyxx,xx;
                for (int aii=0; aii<=nt; aii++)
                {
                        psi[aii] = ksi*fieldtn[aii];
                        ekap[aii] = kapkapu[aii]+psi[aii];
                }
                for (int kj=0; kj<=2; kj++)
                {
                        dummy1[kj] = delru[kj][gb1]/su[gb1];
                        dummy2[kj] = delru[kj][gb1-1]/su[gb1-1];
                        dummy3[kj] = delru[kj][gb2]/su[gb2];
                        dummy4[kj] = delru[kj][gb2-1]/su[gb2-1];
                }
                        dummy1d = dotpro(dummy1[0],dummy1[1],dummy1[2]
                        ,tgu[0],tgu[1],tgu[2]);
                        dummy2d = dotpro(dummy2[0],dummy2[1],dummy2[2]
                        ,tgu[0],tgu[1],tgu[2]);
                        dummy3d = dotpro(dummy3[0],dummy3[1],dummy3[2]
                        ,tgd[0],tgd[1],tgd[2]);
                        dummy4d = dotpro(dummy4[0],dummy4[1],dummy4[2]
                        ,tgd[0],tgd[1],tgd[2]);
                        dihedral1l = acos(-dummy1d);
                        dihedral2l = acos(-dummy3d);
                        dihedral1r = acos( dummy2d);
                        dihedral2r = acos( dummy4d);
        vectorpro(dummy1[0],dummy1[1],dummy1[2],tgu[0],tgu[1],tgu[2]);
        dummymt1 = dotpro(0,0,1,vect[0],vect[1],vect[2]);
        vectorpro(dummy2[0],dummy2[1],dummy2[2],tgu[0],tgu[1],tgu[2]);
        dummymt1 = dotpro(0,0,1,vect[0],vect[1],vect[2])-dummymt1;
        vectorpro(dummy3[0],dummy3[1],dummy3[2],tgd[0],tgd[1],tgd[2]);
        dummymt2 = dotpro(0,0,1,vect[0],vect[1],vect[2]);
        vectorpro(dummy4[0],dummy4[1],dummy4[2],tgd[0],tgd[1],tgd[2]);
        dummymt2 = dotpro(0,0,1,vect[0],vect[1],vect[2])-dummymt2;
                //node velocities
/* 0 */         v[0] = 2*(ekap[1]-ekap[0])/sqr(su[0]);
                for (int ajj=1; ajj<=nt-1; ajj++)
                {
/*gb1-1 */ if (ajj==gb1-1)
                        {
                                dummyx = (su[gb1-3]+2*su[gb1-2]+su[gb1-1])*0.5;
                                dummyxx = (su[gb1-3]+su[gb1-2])*0.5;
                                xx = 0.5*su[gb1-3]+su[gb1-2]+su[gb1-1];
                                inter(0,dummyxx,dummyx,ksi*fieldt[gb1-3]
                                ,ksi*fieldt[gb1-2],ksi*fieldt[gb1-1]);
                                psi[gb1] = a*sqr(xx)+b*xx+c;
```

```
                    }
                           v[ajj] = -delta/omega*(mgl*0.5*(lamda-dummy2d)-
                           tmgb*dummymt1);
                           v[ajj] = v[ajj] -(ekap[gb1-1]-ekap[gb1-2])
                           /su[gb1-2]+(psi[gb1]-psi[gb1-1])/su[gb1-1];
                           v[ajj] = v[ajj]/(su[gb1-1]+0.5*su[gb1-2]);
                    }
/* gb1*/   else if (ajj==gb1)
                    {
                           v[ajj] = mgb*(lamda+0.5*(dummy1d-dummy2d))
                           /omega;
                           vgb1 = v[ajj];
                    }
/* gb1+1*/ else if (ajj==gb1+1)
                    {
                           dummyx = (su[gb1+2]+2*su[gb1+1]+su[gb1])*0.5;
                           dummyxx = (su[gb1+1]+su[gb1+2])*0.5;
                           xx = 0.5*su[gb1+2]+su[gb1+1]+su[gb1];
                           inter(0,dummyxx,dummyx,ksi*fieldt[gb1+2]
                           ,ksi*fieldt[gb1+1],ksi*fieldt[gb1]);
                           psi[gb1] = a*sqr(xx)+b*xx+c;
                           v[ajj] = -delta/omega*(mgl*0.5*(lamda+dummy1d)
                           +tmgb*dummymt1);
                           v[ajj] = v[ajj] +(ekap[gb1+2]-ekap[gb1+1])
                           /su[gb1+1]-(psi[gb1+1]-psi[gb1])/su[gb1];
                           v[ajj] = v[ajj]/(su[gb1]+0.5*su[gb1+1]);
                    }
/*gb2-1 */ else if (ajj==gb2-1)
                    {
                           dummyx = (su[gb2-3]+2*su[gb2-2]+su[gb2-1])*0.5;
                           dummyxx = (su[gb2-3]+su[gb2-2])*0.5;
                           xx = su[gb2-1]+su[gb2-2]+0.5*su[gb2-3];
                           inter(0,dummyxx,dummyx,ksi*fieldt[gb2-3]
                           ,ksi*fieldt[gb2-2],ksi*fieldt[gb2-1]);
                           psi[gb2] = a*sqr(xx)+b*xx+c;
                           v[ajj] = -delta/omega*(mgl*0.5*(lamda-dummy4d)
                           -tmgb*dummymt2);
                           v[ajj] = v[ajj] -(ekap[gb2-1]-ekap[gb2-2])
                           /su[gb2-2]+(psi[gb2]-psi[gb2-1])/su[gb2-1];
                           v[ajj] = v[ajj]/(su[gb2-1]+0.5*su[gb2-2]);
                    }
/* gb2*/   else if (ajj==gb2)
                    {
                           v[ajj] = mgb*(lamda+0.5*(dummy3d-ummy4d))/omega;
                           vgb2 = v[ajj];
                    }
/* gb2+1*/ else if (ajj==gb2+1)
                    {
                           dummyx = (su[gb2+2]+2*su[gb2+1]+su[gb2])*0.5;
                           dummyxx = (su[gb2+2]+su[gb2+1])*0.5;
                           xx = su[gb2]+su[gb2+1]+0.5*su[gb2+2];
                           inter(0,dummyxx,dummyx,ksi*fieldt[gb2+2]
                           ,ksi*fieldt[gb2+1],ksi*fieldt[gb2]);
                           psi[gb2] = a*sqr(xx)+b*xx+c;
                           v[ajj] = -delta/omega*(mgl*0.5*(lamda+dummy3d)
                           +tmgb*dummymt2);
                           v[ajj] = v[ajj] +(ekap[gb2+2]-ekap[gb2+1])
                           /su[gb2+1]-(psi[gb2+1]-psi[gb2])/su[gb2];
                           v[ajj] = v[ajj]/(su[gb2]+0.5*su[gb2+1]);
                    }
/*rest*/   else
                    {
                           v[ajj] = (ekap[ajj+1]-ekap[ajj])/su[ajj]-
                           (ekap[ajj]-ekap[ajj-1])/su[ajj-1];
                           v[ajj] = 2*v[ajj]/(su[ajj]+su[ajj-1]);
                    }
             }
/*nt*/       v[nt] = 2*(ekap[nt-1]-ekap[nt])/sqr(su[nt-1]);
```

```
              vmax = v[0];
              for (int ajj=0; ajj<=nt; ajj++)
              {
                     if (fabs(v[ajj])>=vmax)
                     {
                            vmax = fabs(v[ajj]);
                     }
              }
              for (int ajj=1; ajj<=nt-1; ajj++)
              {
                     for (int aii=0; aii<=1; aii++)
                     {
                            if (ajj==gb1)
                            {
                            rt[aii][ajj] = rt[aii][ajj]+deltat*v[ajj]
                            *tgu[aii];
                            }
                            else if (ajj==gb2)
                            {
                            rt[aii][ajj] = rt[aii][ajj]+deltat*v[ajj]
                            *tgd[aii];
                            }
                            else
                            {
                     rt[aii][ajj]= rt[aii][ajj]+deltat*v[ajj]
                     *llnu[aii][ajj];
                            }
                     }
              }
       rt[1][0] = rt[1][0]-deltat*v[0];
       rt[1][nt] = rt[1][nt]+deltat*v[nt];
}

/*     This procedure performs the remeshing by eliminating those segments
       smaller than rmin and dividing those which are greater than rmax
       into two parts and also keeps the grain boundary triple junction
       as a stable point.*/
void remeshing()
{
       int ka = 1;
       int gnew1,gnew2,nn;
       double magi;
       int flag = 0;
       rmax = emax*dm;
       rmin = emin*dm;
       arr2 rm,delrr;
       rm[0][0] = rt[0][0];
       rm[1][0] = rt[1][0];
       rm[2][0] = rt[2][0];
       int Z = 0;
       for (int ki=0; ki<=gb1-2; ki++)
       { // {zone 1}
              if (su[ki] >= rmax)
              {
                     if (Z==1)
                            {
                                   for(int kj=0; kj<=2; kj++)
                                   {
                                   rm[kj][ka] = (rt[kj][ki+1]+rt[kj][ki-1])
                                   /2;
                                   }
                                   Z = 0;
                            }
                     else
                            for(int kj=0; kj<=2; kj++)
                            {
                                   rm[kj][ka] = (rt[kj][ki+1]+rt[kj][ki])/2;
```

```
                    }
             for(int kj=0; kj<=2; kj++)
             {
                    rm[kj][ka+1] = rt[kj][ki+1];
             }
             ka = ka+2;
       }
       if ((su[ki] < rmax) && (su[ki] > rmin))
       {
             for (int kj=0; kj<=2; kj++)
             {
                    rm[kj][ka] = rt[kj][ki+1];
             }
             ka = ka+1;
       }
       if (su[ki] <= rmin)
       {
             for (int kj=0; kj<=2; kj++)
             {
                    delru[kj][ki+1] = delru[kj][ki+1]+delru[kj][ki];
             }
             Z=1;
       }
}
if ((su[gb1-1] >= rmax) || (su[gb1] >= rmax)
|| (su[gb2-1] >= rmax) || (su[gb2] >= rmax))
{
       flag = 1;
}
if ((su[gb1-1] < rmax) && (flag != 1))
{
       for (int kj=0; kj<=2; kj++)
       {
             rm[kj][ka] = rt[kj][gb1];
       }
       gnew1 = ka;
       ka = ka+1;
}
if (flag == 1)
{
       for (int kj=0; kj<=2; kj++)
       {
             rm[kj][ka] = (rt[kj][gb1]+rt[kj][gb1-1])/2;
             rm[kj][ka+1] = rt[kj][gb1];
       }
       gnew1 = ka+1;
       ka = gnew1+1;
}
Z = 0;
if ((su[gb1] < rmax) && (flag != 1))
{
       for (int kj=0; kj<=2; kj++)
       {
             rm[kj][ka] = rt[kj][gb1+1];
       }
       ka = ka+1;
}
if (flag == 1)
{
       for(int kj=0; kj<=2; kj++)
       {
             rm[kj][ka] = (rt[kj][gb1+1]+rt[kj][gb1])/2;
             rm[kj][ka+1] = rt[kj][gb1+1];
       }
       ka = ka+2;
}
for (int ki=gb1+1; ki<=gb2-2; ki++)
```

```
{ // {zone 2}
       if (su[ki] >= rmax)
       {
              if (Z==1)
                     {
                            for(int kj=0; kj<=2; kj++)
                            {
                            rm[kj][ka] = (rt[kj][ki+1]+rt[kj][ki-1])
                            /2;
                            }
                            Z = 0;
                     }
              else
                     {
                            for(int kj=0; kj<=2; kj++)
                            {
                            rm[kj][ka] = (rt[kj][ki+1]+rt[kj][ki])/2;
                            }
                     }
              for(int kj=0; kj<=2; kj++)
              {
                     rm[kj][ka+1] = rt[kj][ki+1];
              }
              ka = ka+2;
       }
       if ((su[ki] < rmax) && (su[ki] > rmin))
       {
              for (int kj=0; kj<=2; kj++)
              {
                     rm[kj][ka] = rt[kj][ki+1];
              }
              ka = ka+1;
       }
       if (su[ki] <= rmin)
       {
              for (int kj=0; kj<=2; kj++)
              {
                     delru[kj][ki+1] = delru[kj][ki+1]+delru[kj][ki];
              }
              Z=1;
       }
}
if ((su[gb2-1] < rmax) && (flag != 1))
{
       for (int kj=0; kj<=2; kj++)
       {
              rm[kj][ka] = rt[kj][gb2];
       }
       gnew2 = ka;
       ka = ka+1;
}
if (flag == 1)
{
       for (int kj=0; kj<=2; kj++)
       {
              rm[kj][ka] = (rt[kj][gb2]+rt[kj][gb2-1])/2;
              rm[kj][ka+1] = rt[kj][gb2];
       }
       gnew2 = ka+1;
       ka = gnew2+1;
}
Z = 0;
if ((su[gb2] < rmax) && (flag != 1))
{
       for (int kj=0; kj<=2; kj++)
       {
              rm[kj][ka] = rt[kj][gb2+1];
```

```
        }
        ka = ka+1;
}
if (flag == 1)
{
        for(int kj=0; kj<=2; kj++)
        {
                rm[kj][ka] = (rt[kj][gb2+1]+rt[kj][gb2])/2;
                rm[kj][ka+1] = rt[kj][gb2+1];
        }
        ka = ka+2;
}
for (int ki=gb2+1; ki<=nt-2; ki++)
{ // {zone 3}
        if (su[ki] >= rmax)
        {
                if (Z==1)
                {
                        for(int kj=0; kj<=2; kj++)
                        {
                                rm[kj][ka] = (rt[kj][ki+1]+rt[kj][ki-1])
                                /2;
                        }
                        Z = 0;
                }
                else
                        for(int kj=0; kj<=2; kj++)
                        {
                                rm[kj][ka] = (rt[kj][ki+1]+rt[kj][ki])/2;
                        }
                for(int kj=0; kj<=2; kj++)
                {
                        rm[kj][ka+1] = rt[kj][ki+1];
                }
                ka = ka+2;
        }
        if ((su[ki] < rmax) && (su[ki] > rmin))
        {
                for (int kj=0; kj<=2; kj++)
                {
                        rm[kj][ka] = rt[kj][ki+1];
                }
                ka = ka+1;
        }
        if (su[ki] <= rmin)
        {
                for (int kj=0; kj<=2; kj++)
                {
                        delru[kj][ki+1] = delru[kj][ki+1]+delru[kj][ki];
                }
                Z=1;
        }
}
for (int kj=0; kj<=2; kj++)
{
        rm[kj][ka] = rt[kj][nt];
        if (su[nt-1] >= rmax)
        {
        rm[kj][ka] = (rm[kj][ka-1]+rt[kj][nt])/2;
        rm[kj][ka+1] = rt[kj][nt];
        nn  = ka+1;
        }
        else nn  = ka;
}
delrr[0][0] = delru[0][nt-1]+delru[0][nt-2];
delrr[1][0] = delru[1][nt-1]+delru[1][nt-2];
delrr[2][0] = delru[2][nt-1]+delru[2][nt-2];
```

```
        magi = magnitude(delrr[0][0],delrr[1][0],delrr[2][0]);
        if (su[nt-1] <= rmin)
        {
                if (magi >= rmax)
                {
                        for (int kj=0; kj<=2; kj++)
                        {
                                rm[kj][ka-1] = (rt[kj][nt]-rm[kj][ka-2])/2;
                                rm[kj][ka] = rt[kj][nt];
                        }
                }
                else
                {
                        for (int kj=0; kj<=2; kj++)
                        {
                                rm[kj][ka-1] = rt[kj][nt];
                        }
                }
        }
        gb1 = gnew1;
        gb2 = gnew2;
        nt = nn;
        for (int ki=0; ki<=nt; ki++)
        {
                rt[0][ki] = rm[0][ki];
                rt[1][ki] = rm[1][ki];
                rt[2][ki] = rm[2][ki];
        }
}
void getparam()
{
        ifstream in;
        in.open("ms2.dat");
        in >> newdata ;     //{1:  if 0 new experiment if 1 continuous from
                                      cont.dat}
        in >> gmdiv;        //{2:  gb division}
        in >> mc;           //{3:  cathode division}
        in >> deltat ;      //{3:  initial time interval}
        in >> epstime ;     //{4:  time step correction}
        in >> emin;         //{5:  minimum segment length}
        in >> emax;         //{6:  maximum segment length}
        in >> t;            //{7:  initial loop number}
        in >> ms;           //{8:  data record number}
        in >> ksi;          //{9:  electron wind intensity}
        in >> nloop;        //{10: loop number}
        in >> timet;        //{11: real time}
        in >> mint;         //{12: integration segment number (odd)}
        in >> sl;           //{13: strip length coefficient}
        in >> sw;           //{14: strip coefficient}
        in >> mdiv;         //{15: division}
        in >> delta;        //{16: grain boundary thickness}
        in >> gb1;          //{17: location of the first grain boundary}
        in >> lamda1;       //{18: equilibrium dihedral angle between gb1
                                   and upper strip}
        in >> gb2;          //{19: location of the second grain boundary}
        in >> lamda2 ;      //{20: equilibrium dihedral angle between gb2
                                   and lower strip}
        in >> mgb;          //{21: grain boundary longitudinal mobility}
        in >> tmgb;         //{22: grain boundary transverse mobility}
        in >> mgl;          //{23: grain boundary longtidunal transverse
                                   mobility}
        in.close();
        lamda = lamda1;
        ruii[0] = -(gb2-mdiv)*sl/mdiv;
        ruii[1] = -sw;
        gb2 = gb2+2*mdiv+2*mc;
        omega = delta*delta*delta;   // atomic volume}
```

```
       dm = sl/mdiv;                // mean segment lenght}
       rui[0] = (gb1-mdiv)*sl/mdiv;
       rui[1] = sw;
}
/*     This procedure gets parameters from " cont.txt"       */
void getcontparam()
{
       double sil;
       ifstream in("cont.txt");
       in >>rt[0][0]>>rt[1][0]>>sil>>sil>>sil>>sil>>sil>>nu>>t>>ms>>timet>>
       gb1>>gb2>>nl;
       nt = nu+nl+1;
       gb2 = gb2+nu+1;
       for(int i=1; i<=nt; i++)
       {
                     in >>rt[0][i]>>rt[1][i]>>sil>>sil>>sil>>sil>>sil  ;
       }
       t = t+1;
}
/*     OGURTANI Model:
       Grain boundary grooving under the effect of electron wind and
       thermal streses using IBEM calculations. Finite strip with "grain
       boundary". */
void gbgroove()
{
       int kk=100;
       int kt;
       //for determining cathode escape rate
       double rtmax;
       time_t curtime;
       time(&curtime);
       getparam();
       if (newdata==0)     generate();
       else   getcontparam();
       tg();
       ofstream out1;      //open files for multiple write
       out1.open("angles.txt",ofstream::out | ofstream::app);
       out1 << setiosflags(ios::showpoint);
       out1 << setiosflags(ios::fixed);
       ofstream out2;
       out2.open("accessories.txt",ofstream::out | ofstream::app);
       out2 << setiosflags(ios::showpoint);
       out2 << setiosflags(ios::fixed);
       kt = t+32;
       while(t <= nloop)
       {
              delr1();
              psir();
              kappa();
              if (ksi != 0)
              {
              if ( (t/kk)*kk==t || t<=kt ){
                     noc1();
                     rcw1();
                     tin();
                     cf();
                     field();
                     }
              }
              vcalc();
              deltat = epstime*dm/vmax;
              if (((t+1)/kk)*kk==t+1 || t<=kt || ksi==0){
                     delr1();
                     // perform remeshing
                     remeshing();
              }
              //runaway cathode
```

```
              rtmax = rt[0][gb1];
              for (int ajj=gb1+1; ajj<=gb2; ajj++)
              {
                     if ((rt[0][ajj]>rtmax) && (rt[1][ajj]>=0))
                     ca = ajj;
                     if (fabs(rt[1][ajj+1])<fabs(rt[1][ajj]))
                     ca = ajj+1;
                     if (rt[1][ajj]<0)   break;
              }
//indexes for determining the electric field normals at cathode
              for (int ajj=ca-1; ajj>=gb1; ajj--)
              {
              if ((rt[1][ajj]>=rt[1][ajj+1]) && (rt[1][ajj]<sw))
              cu = ajj;
              if (rt[1][ajj]<=rt[1][ajj+1])    break;
              }
              for (int ajj=ca+1; ajj<=gb2; ajj++)
              {
              if ((rt[1][ajj]<=rt[1][ajj-1]) && (rt[1][ajj]>-sw))
              cd = ajj;
              if (rt[1][ajj]>=rt[1][ajj-1])    break;
              }
              //calculate the groove depth
              for (int j=0; j<=1; j++)
              {
                     ruf[j] = rt[j][gb1]-rui[j];
              }
              H = sign(-ruf[1])*magnitude(ruf[0],ruf[1],0);
                            for (int j=0; j<=1; j++)
              {
                     ruf[j] = rt[j][gb2]-ruii[j];
              }
              HL = sign(-ruf[1])*magnitude(ruf[0],ruf[1],0);
              if (t < 257){ mpow = timer(2,ms);}
              else if (t < 1001){ mpow = 300+100*(ms-9);}
              else if (t < 20001){ mpow = 10000+1000*(ms-25);}
              else if (t < 100001){ mpow = 20000+2500*(ms-35);}
              else  { mpow = 100000+5000*(ms-67);}
              timet = timet+deltat;
              if (t == mpow)
              {
                     ofstream out;
                     ifstream in;
                     out.open("name.txt");
                     out << ms << "csl.txt" ;
                     out.close();
                     in.open("name.txt");
                     in >> sy ;
                     in.close();
                     out << setiosflags(ios::showpoint);
                     out << setiosflags(ios::fixed);
                     out.open(sy.c_str(),ios::app );
       out<<setprecision(17)<<rt[0][0]<<""<<rt[1][0]<<""<<kapkapu[0]<<""
       <<mu[0]<<" "<<fieldtn[0]<<" "<<llnu[0][0]<<" "<<llnu[1][0]<<" "
       <<nt<<" "<<t
       <<" "<<ms<<" "<<timet<<" "<<gb1<<" "<<gb2<<" "<<endl;
                     for(int i=1; i<=nt; i++){
       out<<setprecision(17)<<rt[0][i]<<""<<rt[1][i]<<""<<kapkapu[i]<<" "
       <<mu[i]<<" "<<fieldtn[i]<<" "<<llnu[0][i]<<" "<< llnu[1][i]<<endl;}
                     out.close();
       out1<<setprecision(17)<<dihedral1l<<" "<<dihedral1r<<" "<<dihedral2l
       <<" "<<dihedral2r<<endl;
       out2<<setprecision(17)<<timet<<""<<vgb1<<""<<vgb2<<""<<H<<" "
       <<rt[0][ca]<<""<<rt[1][ca]<<""<<v[ca]<<""<<rt[0][cu]<<""<<rt[1][cu]
       <<" "<<rt[0][cd]<<" "<<rt[1][cd]<<" "<<HL<<endl;
       ms++ ;}
              if ( rt[1][gb1] < 0 || rt[1][gb2] > 0 ||
```

```
                rt[1][gb1] == rt[1][gb2])
                {
                        ofstream out;
                        ifstream in;
                        out.open("name.txt");
                        out << "ms2final.txt" ;
                        out.close();
                        in.open("name.txt");
                        in >> sy ;
                        in.close();
                        out << setiosflags(ios::showpoint);
                        out << setiosflags(ios::fixed);
                        out.open(sy.c_str(),ios::app );
        out<<setprecision(17)<<rt[0][0]<<""<<rt[1][0]<<""<<kapkapu[0]<<" "
        <<mu[0]<<" "<<fieldtn[0]<<" "<<llnu[0][0]<<" "<<llnu[1][0]<<" "
        <<nt<<" "<<t<<" "<<ms<<" "<<timet<<" "<<gb1<<" "<<gb2<<" "<<endl;
                        for(int i=1; i<=nt; i++){
        out<<setprecision(17)<<rt[0][i]<<""<<rt[1][i]<<""<<kapkapu[i]<<"
        <<mu[i]<<" "<<fieldtn[i]<<" "<<llnu[0][i]<<" "<< llnu[1][i]<<endl;}
                        out.close();
                        break;
                }
                t++ ;
        }
}
int main()
{
        gbgroove();
}
```